Multifunctional Materials: Bottom-up and Top-down

Thesis by

Raymond Andrew Weitekamp

In Partial Fulfillment of the Requirements

for the Degree of

Doctor of Philosophy

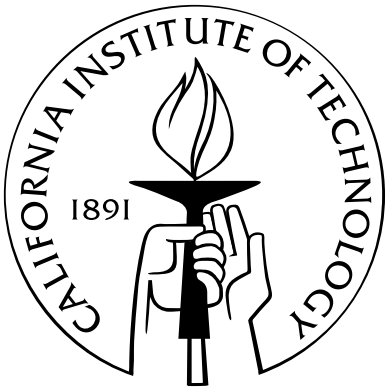

California Institute of Technology

Pasadena, California

2015

(Defended May 29, 2015)

Acknowledgments

It takes a village to write a thesis.

First and foremost, I would like to thank my advisors, Bob and Harry, for giving me the freedom and support to explore my own scientific interests. I had the rare opportunity to be able to work on anything and everything during my graduate career, and I am very grateful for that experience. Every year, we discovered more and more overlap between these two seemingly disparate fields of synthetic chemistry and applied physics. I have learned a great deal from both of them along the way.

I am especially grateful to my first scientific advisor, my father, for all of his love, guidance, and editorial skills; equally grateful to my mother for her love, wisdom, and presentation coaching. My parents have made tremendous sacrifices for me and my brothers, I could not have asked for more a supportive and inspiring family. While I might be the oldest sibling, I am certainly not always right - I've learned a lot from my brothers.

I would like to thank my committee members Dave Tirrell, Tom Miller, and Harry Gray for their support and perspectives. The last five years have been an exciting ride —I have really appreciated the feedback from my committee along the way.

All of the work in this thesis was highly collaborative. Between the Grubbs and Atwater groups, I have had approximately 150 labmates during my graduate career. Many of them have been collaborators on the work described here. For the published work, I have attempted to find a balance between including complete descriptions of the work, while attempting to be concise where others have already addressed the detailed procedures. In the unpublished work, I hope I have provided a snapshot of the many directions my collaborators and I are currently exploring. I cannot possibly

list all of the people who have helped along the way, so I will instead highlight major contributors to the research of each chapter:

Chapter 2 - Garret Miyake, Ben Sveinbjörnsson, Alice Chang, Victoria Piunova, Chris Daeffler, Rob MacFarlane, Yan Xia, Chris Bates, Jeremiah Johnson

Chapter 3 - Dennis Callahan, Jonathan Grandidier, Mike Deceglie, Colton Bukowsky, Corsin Battaglia

Chapter 5 - Vanessa Marx

Chapter 6 - Jim Fakonas, Shane Mangold, Colton Bukowsky, Tracy Clevenger, Oana Luca, Ricky Barz

Chapter 7 - Nikolaj Mandsberg

Science aside, Caltech has been a great place to be. I've really enjoyed spending time with my labmates, everything from group camping trips to softball championships, pub crawls to rock climbing, business plan competitions to jam sessions. I'm also really grateful to my housemates over the years: Ari, Ross, Andy, Shawn, Nick. Aside from my parent's house, my 3.5 years on Adam's Hill has been my longest stretch in one place, and it definitely flew by. I would be remiss not thank my sole source of energy, Professor Doctor Ernesto al Fresco —his mobile culinary laboratory has sustained my good health, even through rough times.

Finally, I would like to thank my girlfriend, Gabby, who has helped me put it all in perspective.

Abstract

This thesis is thematically separated into two complimentary approaches to advanced materials synthesis: bottom-up and top-down. Part I will discuss the self-assembly of photonic crystals, a unique class of periodic nanostructured materials featuring resonant optical response. Chapter 1 will introduce the concepts of self-assembly, specifically in the context of colloidal crystals and block copolymer nanostructures. Chapter 2 summarizes many years of work towards the goal of utilizing brush block copolymers as paintable photonic crystals. We employed 2D colloidal crystals as resonant light-trapping elements to improve the performance of thin-film solar cells; this work is described in Chapter 3. Part II of the thesis is centered around the concept of functional lithography: the ability to directly pattern materials with tailored physical properties and chemically active interfaces. We will briefly provide a history of photolithography in Chapter 4, and outline some of the limitations of the incumbent lithographic methods. The discovery of latent reactivity in ruthenium vinyl ether complexes, and the subsequent development of PhotoLithographic Olefin Metathesis Polymerization (PLOMP), are discussed in Chapter 5. This discovery has since blossomed into a true platform technology. We will discuss improvments to the functional group tolerance of PLOMP, as well as a few of our efforts to use PLOMP towards specific applications in Chapter 6. In Chapter 7 we document our attempts to activate PLOMP resists via multiphoton absorption, towards 3D printing of chemically functional microstructures.

Contents

List of Figures

Part I

Photonic Crystals via Self-assembly

Chapter 1

Bottom-up Fabrication

Portions adapted with permission from Miyake, Garret M., Raymond A. Weitekamp, and Robert H. Grubbs. "Synthesis of Materials with Nanostructured Periodicity." Handbook of Metathesis-Polymer Synthesis (2015).

Chapter Abstract

"Bottom-up" fabrication generally refers to directed- and self-assembly of materials, typically with periodic composition. In this introductory chapter, we highlight some of the advantages of bottom-up approaches to materials synthesis. We outline the basic principles of self-assembly for two important classes of hybrid materials: colloidal crystals and block copolymers. Colloidal crystals are useful materials for a number of optoelectronic device applications, particularly as elements of resonant dielectric structures. Block copolymers represent a versatile platform for multifunctional materials fabrication; we specifically highlight periodic nanostructured materials synthesized via ring-opening metathesis polymerization.

1.1 Bottom-up Fabrication via Self-Assembly

Self-assembly is a broadly-used term which has been applied to diverse processes such as colloidal packing, protein folding, and liquid crystal formation. In the context of this thesis, we specifically focus our discussion of self-assembly on the organization of distinct macromolecular or crystalline components into ordered aggregates. In principle, the assembly processes we discuss are reversible, in that covalent bond formation does not play a significant role in the process of aggregation. Self-assembly can be used to fabricate nanostructured materials where precision "top-down" approaches such as photolithography would be impossible or impractical. Instead of a defining a lithographic pattern directly, the information about the materials properties and assembled geometry are instead encoded into the individual components as shape, surface charge, polarizability, functionality, and mass.[1] By tuning these chemical driving forces, complex morphologies can be achieved "for free", which is an attractive approach for many applications, such as membranes [2], photonics [3], lithographic etch masks [4], and architected nanomaterials for drug delivery [5].

1.2 Colloidal Assembly

Ordered arrays of colloid particles, or colloidal crystals, are useful materials and templates for nanofabrication because they can be synthesized from inexpensive materials by self-assembly. The assembly processes are dictated by a number of interactions, including van der Waals forces, steric repulsions, and Coulombic repulsions. Perhaps the most familiar example of a colloidal crystal is the opal gemstone, consisting of polycrystalline domains of close-packed silica colloid. The color of these gemstones is due to diffractive photonic effects. The concept of "structural color" will be further elucidated in Chapter 2, as part of an introduction to photonic crystals. In the lab, colloidal crystals are typically fabricated from granular suspensions through a variety of controlled evaporation techniques. The diversity and flexibility of nanostructured arrays fabricated by colloidal lithography endow a variety of applications in many

fields, such as optics, photonics, bioscience, microelectronic engineering.

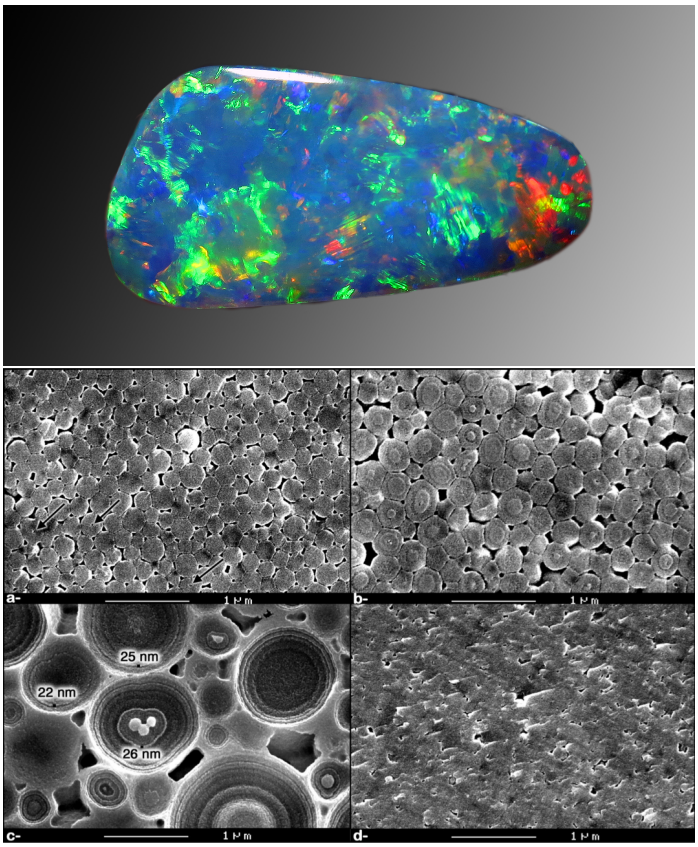

Figure 1.1: Photograph and SEM micrographs of naturally occuring opal. Top: "Coober Pedy Opal Doublet" by Dpulitzer via Wikimedia Commons. Bottom: Reference [6].

1.3 2D Colloidal Crystals

Two-dimensional colloidal crystals have a vast number of applications. Examples include lithographic templates, photonic crystals, anti-reflective coatings, and metamaterials.[7] Specifically, we will discuss their use as resonant dielectric structures for absorption enhancement in photovoltaic devices in Chapter 3. While three dimensional, hexagonally close-packed structures readily assemble from suspensions of spherical colloids with nanometer to micron diameters, the assembly of two dimensional monolayer arrays remains a challenging task. The 2D colloidal crystal quality is sensitive to variations in sphere size, density, surface functionality, and zeta po-

tential.[7] 2D colloidal crystals have been generated using a number of techniques, including Langmuir-Blodgett [4, 8], electric-field-induced assembly [9], convective assembly [10], and controlled evaporation.[11]

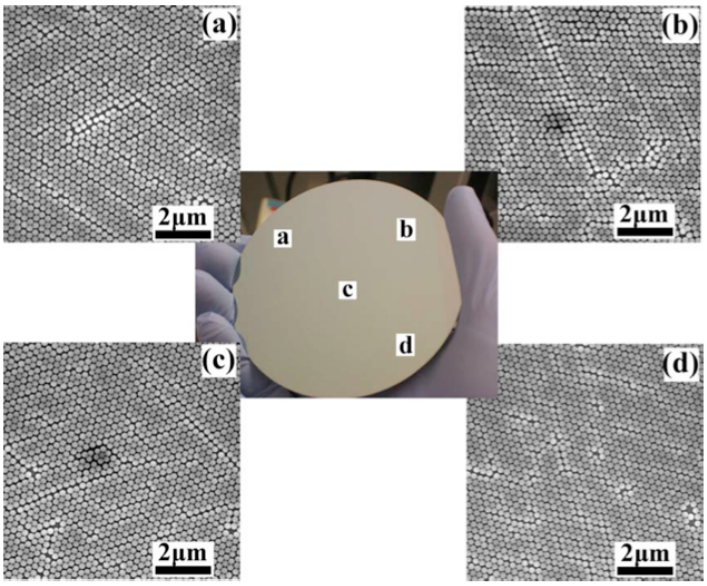

Figure 1.2: A highly uniform 2D colloidal crystal of silica nanospheres on a 4-inch diameter silicon wafer. Image from Reference [4].

Additionally, the substrate can be lithographically patterned to generate a template for colloidal self-assembly. For example, an array of topological "wells" can be patterned to facilitate colloidal self-assembly. There are number of reported examples that combine colloidal assembly and lithography to yield novel nanostructures.[12, 13] First, colloidal assembly has been performed on a lithographically defined polymer substrate, to trap the colloids inside the patterned wells.[13] PDMS stamps have also been employed to pick and place colloidal monolayers from a multilayer substrate.[12] In this case, the transfer substrate contains a thin polymer layer, which is heated above its glass transition temperature and then cooled to lock in the patterned colloidal crystal.

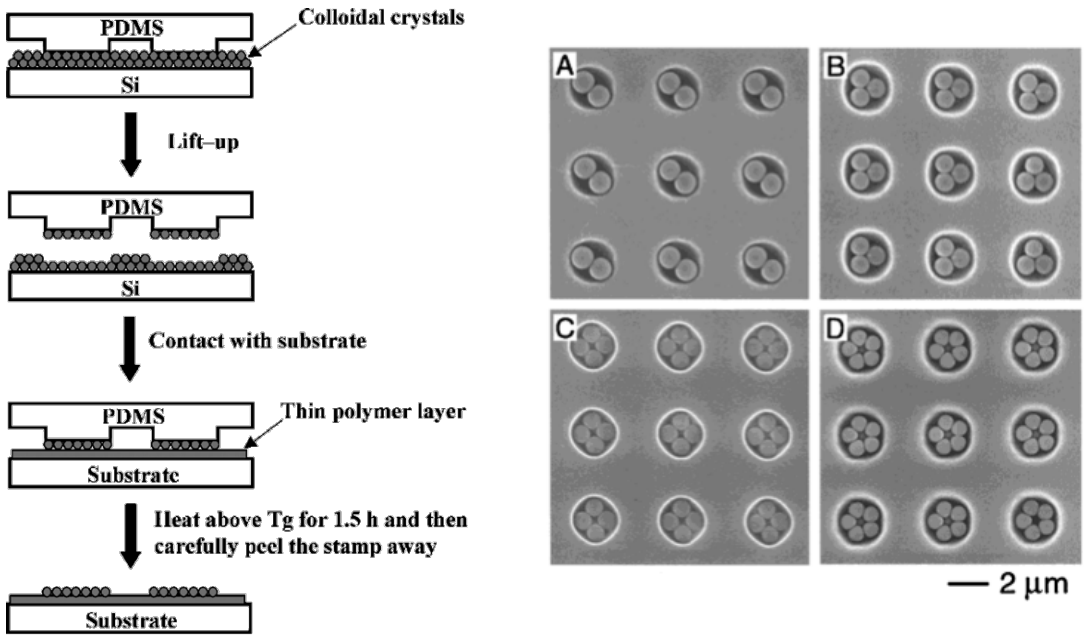

Figure 1.3: (Left) Microcontact printing of colloidal crystals enables spatially defined monolayers. From Reference [12]. (Right) Lithographically defined microstructures can be used to template colloidal assembly. From Reference [13].

One of the major challenges in colloidal assembly is precision. For certain applications, these templated approaches can render precise structuring through a combination of top-down and bottom-up techniques. In photonic devices, where fidelity is crucial, extensive optimization is sometimes required to achieve highly-ordered colloidal crystals. Despite these drawbacks, there are many cases in which colloidal assembly provides a robust approach to fabricating periodic micro- and nanostructures.

1.4 Block Copolymer Assembly

The highly ordered morphologies afforded by block copolymer (BC) self-assembly provide an attractive bottom-up approach to materials with nanostructured periodicity [14, 15]. In BC self-assembly, reorganization is driven by phase segregation of the chemically distinct blocks, while macroscopic separation is inhibited by covalent linkage between the blocks [16]. The morphological landscape is dictated by several parameters, including the degree of polymerization of the polymer, the volume fractions of the components (ϕ_A & ϕ_B), and the interaction parameters of the system χ. χ is a dimensionless representation of the energetic cost of exchanging equal volumes of polymer A & B:

$$\chi = z\Delta w/kT$$

In the equation above, z is the number of nearest neighbors, Δw is the difference between the A/B interaction energy and the average of the self-interaction energies, and kT is the thermal energy. The Flory-Huggins free energy of mixing is:

$$\Delta G_m = -T\Delta S_m + \chi kT\phi_A\phi_B \ ,$$

where ΔS_m is the entropy of ideal combinatorial mixing. Chemically dissimilar polymers will tend to have a large interaction parameter, which favors microphase separation. Mixing is favored at higher temperatures; this enables one to thermally anneal block copolymers into morphologies of higher symmetry.

BC self-assembly presents a highly tunable platform, because the polymer components can be altered to encompass an endless array of materials with targeted chemical or physical properties through the incorporation of choice building blocks. These bulk periodic nanostructured materials have diverse applications, such as separation membranes, lithographic templates, solid electrolytes, and photonic crystals (PCs). BCs are most notorious for their ability to self-assemble to domain sizes on the order of tens of nanometers; however, through polymer architectural design and advanced synthetic capabilities, BCs with the ability to assemble to domain sizes exceeding 100 nm are emerging, opening new avenues of research and potential applications.

1.5 Periodic Nanostructured Materials via ROMP

Ruthenium-mediated ring-opening metathesis polymerization (ROMP) of strained cyclic monomers has matured into a powerful polymerization methodology [17–19]. The living polymerization characteristics and broad functional and steric tolerance of ruthenium catalysts have enabled scientists to synthesize diverse polymeric materials with controlled molecular weights (MWs) and narrow molecular weight distributions (MWDs) [20]. Furthermore, the ability to precisely define polymer chain-end groups through initiator modification [21] or termination with functionalized chain-transfer agents (CTAs) [22] allows the modular preparation of copolymers through the sequencing of multiple polymerization methodologies. These attributes of ruthenium-mediated ROMP give rise to the ability to make on-demand, creatively designed BCs.

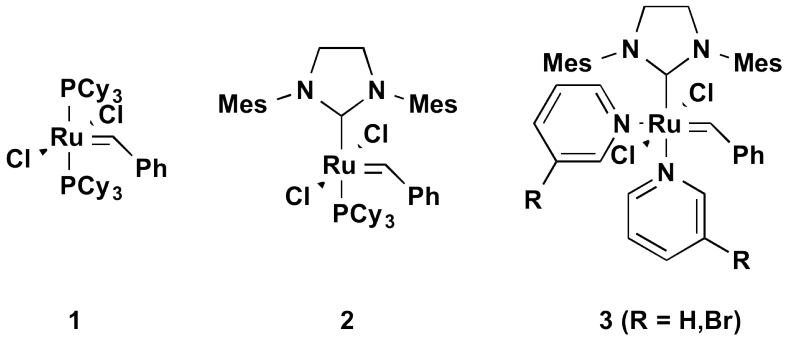

Figure 1.4: Structures of common ruthenium-based ROMP catalysts.

While the versatility of ROMP has made it a heavily utilized polymerization methodology, there are surprisingly few reports on the self-assembly of BCs constructed entirely by metathesis. Trimmel and coworkers synthesized a series of symmetric and asymmetric precursors to amphiphilic BCs through the sequential ROMP of methyl ester- and tert-butyl ester-functionalized norbornene (NBE) monomers initiated by catalyst **1** (Figure 1.5) [23]. Deprotection of the tert-butyl ester side groups with trifluoro acetic acid afforded the carboxylic acid functionality, rendering the final BCs amphiphilic. Because of the thermal instability of the polymers, films were drop-cast from a toluene solution, and the solid-state assembly of the BCs was investigated using a variety of analytical techniques. The BC morphology was visualized

with transmission electron microscopy (TEM) and confirmed by small-angle X-ray scattering (SAXS). Well-defined lamellae, cylinders, and spheres could be accessed by varying the relative volume fraction of the two blocks. Consistent with theory, increasing the BC MW at a constant volume fraction resulted in the assembly to the same morphology but with larger domain sizes. For lamellar nanostructures, the domain sizes of the periodic unit could be scaled from 18 to 33 nm by increasing the MW (M_{n} from 15.8 to 44.4 kDa). These polymers were later utilized to template the aggregation of a cationic platinum(II) complex by mixing during self-assembly [24]. The platinum complex preferentially assembled with the carboxylic acid-functionalized block, although the incorporation of platinum decreased the fidelity of lamellar ordering. TEM and SAXS were utilized to measure an average lamellar spacing of 39 nm. This supramolecular assembly of discrete nonluminescent platinum complexes produced red phosphorescent films, as a result of the formation of luminescent aggregates driven by BC assembly.

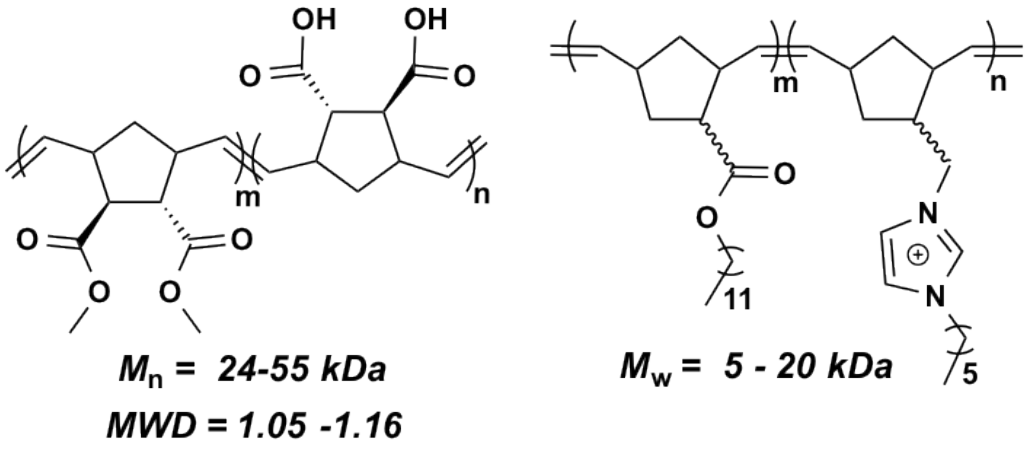

Figure 1.5: Structures of block copolymers synthesized through sequential ROMP. The self-assembly of these two block copolymers was studied by SAXS. From References [23, 24].

Gin and coworkers [25] highlighted the functional group tolerance of ruthenium-mediated ROMP by using **1** to synthesize imidazolium-functionalized BCs (Figure 1.5). As determined by SAXS, all the BCs assembled to a lamellar morphology. Interestingly, it was observed that the domain size ($\sim$ 30 nm) of these materials was

larger than would be expected for BCs of this MW. For comparison, an equal MW poly(styrene-block-vinylpyridine) would assemble to domain sizes of only 20 nm [26]. This observation was attributed to a rigid main-chain conformation that would favor the assembly to larger domains for the imidazolium-based polynorbornene (PNBE) BCs. A library of BCs constructed from these monomers was synthesized by varying the molar incorporation of the imidazolium monomer from 4 to 58% [27]. Extensive SAXS analysis of the BC-derived morphologies was utilized to establish the phase diagrams of the various morphologies. Lamellar, cylindrical, and spherical morphologies could be produced; however, the gyroid morphology was not observed. This was believed to be a result of the strong segregation parameters exhibited by these BCs. Polyionic liquids can be employed as gas separation membranes, because of their high CO_2 gas permeability and mechanical durability. Nanostructured membranes of these imidazolium-based BCs demonstrated CO_2 permeability two orders of magnitude higher than their amorphous analogs [28].

1.6 Hybrid Organic/Inorganic Composites

As BCs readily generate patterns with domain sizes on the order of tens of nanometers, there is growing interest in using them to template other materials, such as ordered organic-inorganic composites [29]. This can be accomplished through the selective removal of one of the components and infilling of the resulting void space [30] or through the direct coordination of metals to one of the blocks [31]. In particular, the incorporation of magnetic metals into the BC template can afford high-density magnetic arrays with a plethora of applications.

Malenfant et al. [34] utilized catalyst 3 to prepare poly(NBE)-block-(NBE decaborane) as precursors to nanostructured ceramics (Figure 1.6). The assembly of a BC with equal volume fractions of the two components was investigated through the controlled evaporation from chloroform and THF. As expected, the BC assembled to highly ordered stacked lamellae when cast from chloroform. Unexpectedly, hexagonally packed cylinders were observed in the films cast from THF, with the decaborane-

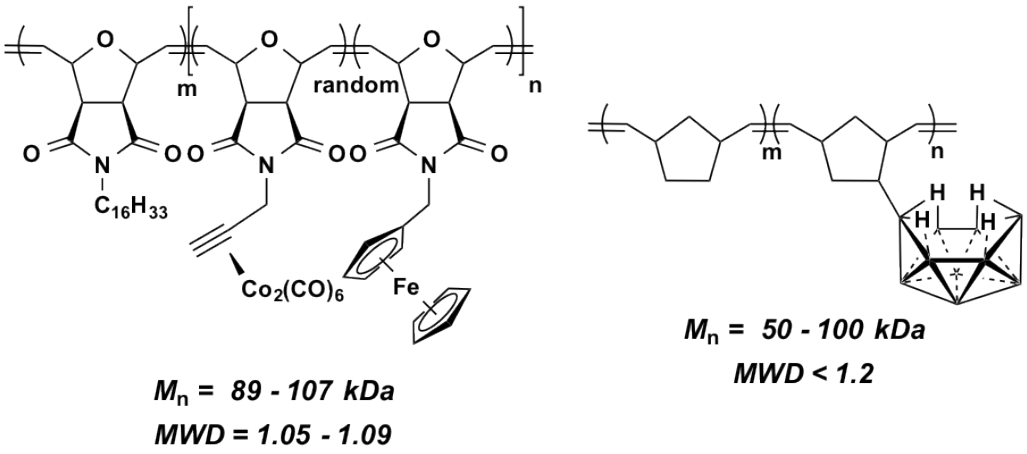

Figure 1.6: These two block copolymers were employed to generate organic/inorganic composite nanostructures. For visual clarity, the boron atoms in the decaborane group on the right are not drawn. From References [32, 33].

functionalized block comprising the matrix (Figure 1.7). It was stated that THF was a preferential solvent for the decaborane block, leading to the formation of cylinders. Pyrolysis was performed on the stacked lamellar nanostructure under a nitrogen atmosphere to produce a boron carbonitride/carbon ceramic composite with a maintained morphology. Additionally, pyrolysis on the cylindrical nanostructure was performed in an ammonia atmosphere to yield a boron nitride matrix constructed of mesoporous cylindrical voids (20 nm) and nanopores (2 nm) within the matrix. Nitrogen absorption was employed to demonstrate the high porosity of these materials. The surface area could reach 950 m^2g^1, which at that time was the highest reported surface area for such materials.

1.7 Challenges

The primary antagonist to self-assembly is chain entanglement —a defining characteristic of polymers which significantly impedes high molecular weight polymers from achieving large, ordered domains. Reaching domain spacings beyond 100 nm is a significant challenge for BCPs [35–37] because the entanglement of high MW polymers presents a large kinetic barrier, despite the large thermodynamic driving force to microphase segregation. As a result, high MW BCPs often end up in a kinetically

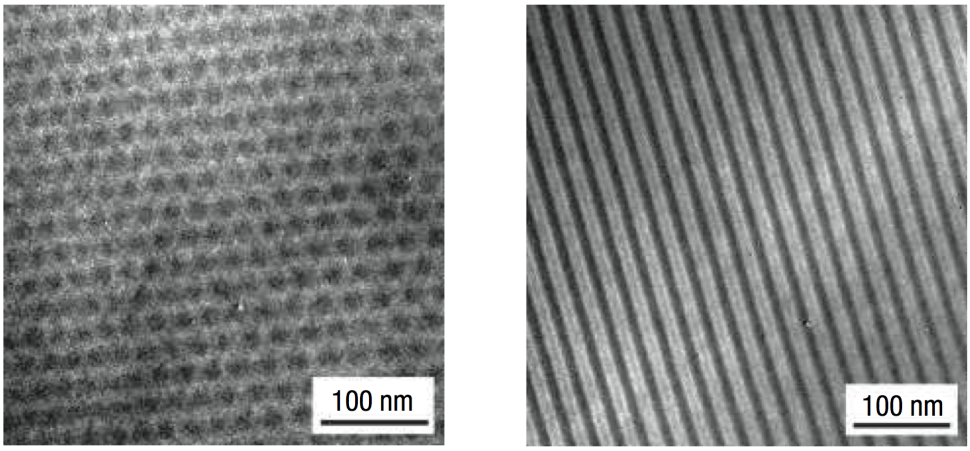

Figure 1.7: TEM bright-field images of the self-assembled microstructures of poly(norbornene)-block-poly(norbornene decaborane) after solvent evaporation. (Left) TEM showing the end view of a hexagonally packed cylindrical structure obtained using THF as the solvent. The poly(norbornene) phase forms the cylinders, and poly(norbornene decaborane) forms the matrix. (Right) TEM bright-field image of a self-assembled microstructure after chloroform evaporation, showing a lamellar morphology. The poly(norbornene) phase forms the darker layers. Image from Reference [33].

trapped state; equilibration is prohibited at a practical time scale. To overcome the practical limitations to the domain sizes and refractive indices of typical BCPs, assembled nanostructures are often swollen with additives, including small molecules [38–40], inorganic nanoparticles [41], or other polymers [36] to achieve photonic bandgaps in the visible and NIR. Additionally, extreme annealing conditions have been used successfully to prepare PC films from BCPs [42]. The complex annealing procedures and additives demanded by much of the work to date on polymer PCs represent a huge barrier to the practical implementation of BCPs as commercially viable optical elements. As chain entanglement presents a fundamental energetic barrier to the reorganization of high MW BCPs into large, ordered nanostructures, methods to surmount these limitations are needed.

References

(1) Whitesides, G. M.; Grzybowski, B. *Science* **2002**, *295*, 2418–2421.

(2) Li, F.; Josephson, D. P.; Stein, A. *Angewandte Chemie International Edition* **2011**, *50*, 360–388.

(3) Ozin, G. A.; Yang, S. M. *Advanced Functional Materials* **2001**, *11*, 95–104.

(4) Hsu, C.-M.; Connor, S. T.; Tang, M. X.; Cui, Y. *Applied Physics Letters* **2008**, *93*, 133109.

(5) Rösler, A.; Vandermeulen, G. W. M.; Klok, H.-A. *Advanced Drug Delivery Reviews* **2012**, *64, Supplement*, 270–279.

(6) Gaillou, E.; Fritsch, E.; Aguilar-Reyes, B.; Rondeau, B.; Post, J.; Barreau, A.; Ostroumov, M. *American Mineralogist* **2008**, *93*, 1865–1873.

(7) Zhang, J.; Li, Y.; Zhang, X.; Yang, B. *Advanced Materials* **2010**, *22*, 4249–4269.

(8) Marquez, M.; Grady, B. P. *Langmuir* **2004**, *20*, 10998–11004.

(9) Hayward, R. C.; Saville, D. A.; Aksay, I. A. *Nature* **2000**, *404*, 56–59.

(10) Prevo, B. G.; Hwang, Y.; Velev, O. D. *Chemistry of materials* **2005**, *17*, 3642–3651.

(11) Mihi, A.; Zhang, C.; Braun, P. V. *Angewandte Chemie* **2011**, *123*, 5830–5833.

(12) Yan, X.; Yao, J.; Lu, G.; Chen, X.; Zhang, K.; Yang, B. *Journal of the American Chemical Society* **2004**, *126*, 10510–10511.

(13) Yin, Y.; Lu, Y.; Gates, B.; Xia, Y. *Journal of the American Chemical Society* **2001**, *123*, 8718–8729.

(14) Bates, F. S.; Hillmyer, M. A.; Lodge, T. P.; Bates, C. M.; Delaney, K. T.; Fredrickson, G. H. *Science* **2012**, *336*, 434–440.

(15) Park, C.; Yoon, J.; Thomas, E. L. *Polymer* **2003**, *44*, 6725–6760.

(16) Bates, F. S.; Fredrickson, G. H. *Physics today* **1999**, *52*, 32–38.

(17) Vougioukalakis, G. C.; Grubbs, R. H. *Chemical reviews* **2009**, *110*, 1746–1787.

(18) Bielawski, C. W.; Grubbs, R. H. *Progress in Polymer Science* **2007**, *32*, 1–29.

(19) *Controlled and living polymerizations: methods and materials*; Müller, A. H. E., Matyjaszewski, K., Eds.; Wiley-VCH: Weinheim, 2009, 612 pp.

(20) Leitgeb, A.; Wappel, J.; Slugovc, C. *Polymer* **2010**, *51*, 2927–2946.

(21) Bielawski, C. W.; Louie, J.; Grubbs, R. H. *Journal of the American Chemical Society* **2000**, *122*, 12872–12873.

(22) Morita, T.; Maughon, B. R.; Bielawski, C. W.; Grubbs, R. H. *Macromolecules* **2000**, *33*, 6621–6623.

(23) Stubenrauch, K.; Fritz-Popovski, G.; Ingolić, E.; Grogger, W.; Glatter, O.; Stelzer, F.; Trimmel, G. *Macromolecules* **2007**, *40*, 4592–4600.

(24) Niedermair, F.; Stubenrauch, K.; Pein, A.; Saf, R.; Ingolić, E.; Grogger, W.; Fritz-Popovski, G.; Trimmel, G.; Slugovc, C. *J. Mater. Chem.* **2011**, *21*, 15183–15185.

(25) Wiesenauer, E. F.; Edwards, J. P.; Scalfani, V. F.; Bailey, T. S.; Gin, D. L. *Macromolecules* **2011**, *44*, 5075–5078.

(26) Matsushita, Y.; Mori, K.; Saguchi, R.; Nakao, Y.; Noda, I.; Nagasawa, M. *Macromolecules* **1990**, *23*, 4313–4316.

(27) Scalfani, V. F.; Wiesenauer, E. F.; Ekblad, J. R.; Edwards, J. P.; Gin, D. L.; Bailey, T. S. *Macromolecules* **2012**, *45*, 4262–4276.

(28) Nguyen, P. T.; Wiesenauer, E. F.; Gin, D. L.; Noble, R. D. *Journal of Membrane Science* **2013**, *430*, 312–320.

(29) Hamley, I. W. *Nanotechnology* **2003**, *14*, R39.

(30) Thurn-Albrecht, T.; Schotter, J.; Kfffdfffdstle, G. A.; Emley, N.; Shibauchi, T.; Krusin-Elbaum, L.; Guarini, K.; Black, C. T.; Tuominen, M. T.; Russell, T. P. *Science* **2000**, *290*, 2126–2129.

(31) Alexandridis, P.; Tsianou, M. *European Polymer Journal* **2011**, *47*, 569–583.

(32) AL-Badri, Z. M.; Maddikeri, R. R.; Zha, Y.; Thaker, H. D.; Dobriyal, P.; Shunmugam, R.; Russell, T. P.; Tew, G. N. *Nature Communications* **2011**, *2*, 482.

(33) Zha, Y.; Thaker, H. D.; Maddikeri, R. R.; Gido, S. P.; Tuominen, M. T.; Tew, G. N. *Journal of the American Chemical Society* **2012**, *134*, 14534–14541.

(34) Malenfant, P. R. L.; Wan, J.; Taylor, S. T.; Manoharan, M. *Nature Nanotechnology* **2007**, *2*, 43–46.

(35) Rzayev, J. *Macromolecules* **2009**, *42*, 2135–2141.

(36) Urbas, A.; Sharp, R.; Fink, Y.; Thomas, E. L.; Xenidou, M.; Fetters, L. J. *Advanced Materials* **2000**, *12*, 812–814.

(37) Edrington, A. C.; Urbas, A. M.; DeRege, P.; Chen, C. X.; Swager, T. M.; Hadjichristidis, N.; Xenidou, M.; Fetters, L. J.; Joannopoulos, J. D.; Fink, Y., et al. *Advanced Materials* **2001**, *13*, 421–425.

(38) Kang, Y.; Walish, J. J.; Gorishnyy, T.; Thomas, E. L. *Nature materials* **2007**, *6*, 957–960.

(39) Valkama, S.; Kosonen, H.; Ruokolainen, J.; Haatainen, T.; Torkkeli, M.; Serimaa, R.; Brinke, G. ten; Ikkala, O. *Nature Materials* **2004**, *3*, 872–876.

(40) Parnell, A. J.; Pryke, A.; Mykhaylyk, O. O.; Howse, J. R.; Adawi, A. M.; Terrill, N. J.; Fairclough, J. P. A. *Soft Matter* **2011**, *7*, 3721–3725.

(41) Lee, I.; Kim, D.; Kal, J.; Baek, H.; Kwak, D.; Go, D.; Kim, E.; Kang, C.; Chung, J.; Jang, Y.; Ji, S.; Joo, J.; Kang, Y. *Advanced Materials* **2010**, *22*, 4973–4977.

(42) Hustad, P. D.; Marchand, G. R.; Garcia-Meitin, E. I.; Roberts, P. L.; Weinhold, J. D. *Macromolecules* **2009**, *42*, 3788–3794.

Chapter 2

Brush Block Copolymers as Photonic Crystals

Portions adapted with permission from:

- Sveinbjörnsson, B. R.; Weitekamp, R. A.; Miyake, G. M.; Xia, Y.; Atwater, H. A.; Grubbs, R. H. "Rapid Self-Assembly of Brush Block Copolymers to Photonic Crystals". *Proceedings of the National Academy of Sciences* **2012**
- Miyake, G. M.; Weitekamp, R. A.; Piunova, V. A.; Grubbs, R. H. "Synthesis of Isocyanate-Based Brush Block Copolymers and Their Rapid Self-Assembly to Infrared-Reflecting Photonic Crystals". *J. Am. Chem. Soc.* **2012**
- Miyake, G. M.; Piunova, V. A.; Weitekamp, R. A.; Grubbs, R. H. "Precisely Tunable Photonic Crystals From Rapidly Self-Assembling Brush Block Copolymer Blends". *Angewandte Chemie International Edition* **2012**
- Piunova, V. A.; Miyake, G. M.; Daeffler, C. S.; Weitekamp, R. A.; Grubbs, R. H. "Highly Ordered Dielectric Mirrors via the Self-Assembly of Dendronized Block Copolymers". *J. Am. Chem. Soc.* **2013**
- Macfarlane, R. J.; Kim, B.; Lee, B.; Weitekamp, R. A.; Bates, C. M.; Lee, S. F.; Chang, A. B.; Delaney, K. T.; Fredrickson, G. H.; Atwater, H. A.; Grubbs, R. H. "Improving Brush Polymer Infrared One-Dimensional Photonic Crystals via Linear Polymer Additives". *J. Am. Chem. Soc.* **2014**
- Miyake, Garret M., Raymond A. Weitekamp, and Robert H. Grubbs. "Synthesis of Materials with Nanostructured Periodicity." Handbook of Metathesis-Polymer Synthesis **2015**. Copyright John Wiley & Sons.

Chapter Abstract

The reduced chain entanglement of brush polymers over their linear analogs drastically lowers the energetic barriers to reorganization. We have demonstrated the rapid self-assembly of brush block copolymers to multilayer nanostructures with tunable domain periodicities up to a few hundred nanometers. This periodic modulation of the material's dielectric function results in photonic bandgaps, which can be engineered to span the entire visible spectrum, from ultraviolet (UV) to near infrared (NIR). We have synthesized a number of different polymeric architectures capable of assembling to photonic crystals and have demonstrated the ability to precisely tune the optical properties through control of the polymer molecular weight and incorporation of blended additives. Sterically demanding side-groups are key to imparting this behavior, which can be accomplished with polymeric or dendritic moieties. We are working towards applying these discoveries towards applications in paintable photonic crystals, including infrared-reflective window films capable of improving the energy efficiency of buildings and vehicles.

2.1 Synthesis of Brush Polymers

The molecular brush polymer architecture is composed of polymeric side chains grafted to a common polymer main chain. The steric repulsions between the dense array of polymeric side-groups cause the main chain to adopt a highly elongated, rigid conformation that exhibits minimal chain entanglement [1]. The reduced entanglement of brush polymers over their linear analogs drastically lowers the energetic barriers to reorganization. As a result, molecular brush block copolymers (BBCPs) have been shown to self-assemble to morphologies with domain sizes well-exceeding 100 nm, a challenging size regime to achieve with linear block copolymers. In many cases, the assembly can be performed at room temperature, which could enable a number of applications in paintable hybrid materials.

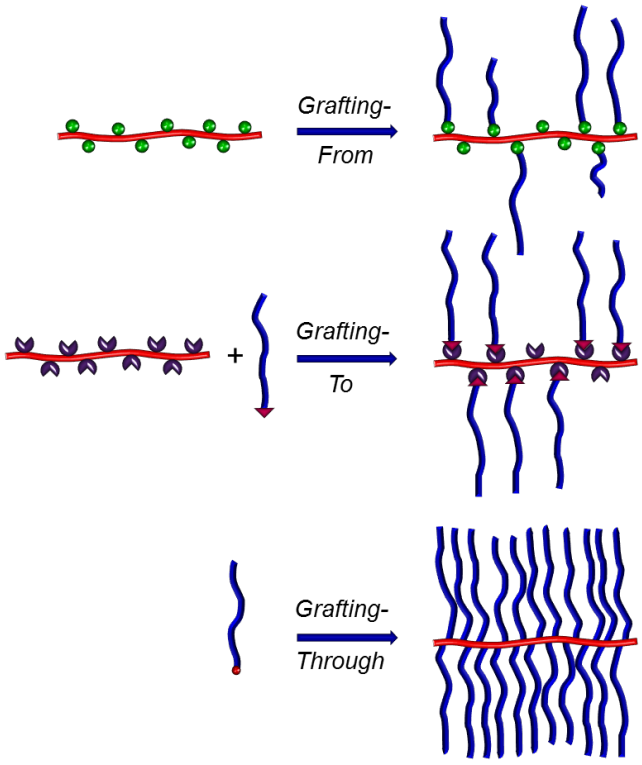

Figure 2.1: Three synthetic strategies for synthesizing brush polymers: grafting-from, grafting-to, and grafting-through.

Brush copolymers with high molecular weights (MW), narrow molecular weight distributions (MWDs), and complete side chain grafting are challenging targets for

synthetic polymer chemists. There are many approaches to these macromolecules, each with their own obstacles [2, 3]. Figure 2.1 depicts the three general strategies: grafting-from, grafting-to, and grafting-through. The grafting-from approach inherently produces nonuniform architectures because of the difficulty in achieving quantitative and uniform growth from a polymeric initiator. In the grafting-to strategy, it is difficult to achieve complete grafting, due to dramatic steric congestion at increased conversion. With these limitations in mind, our group has been interested in the synthesis of uniform and geometrically symmetric molecular brush-brush BCPs, to produce nanostructures with exceedingly large domain sizes. Xia et al. [4, 5] investigated the grafting-through (co)polymerization of polystyrene(PS), polyacrylate (PA), and PLA macromonomers, end-functionalized with *exo*-norbornene chain-end groups, mediated by the very fast-initiating catalyst **3**.

The graft-through ROMP of these macromonomers (MMs) exhibited living characteristics, enabling successful statistical or block copolymerization to high-MW copolymers with narrow molecular weight distributions. The solid-state assembly of these polymers was investigated after thermal annealing at 100 °C for 12 hours. Importantly, it was shown that, for statistical copolymers, the domain sizes of the materials was dictated by the MW of the grafts, whereas for BCPs the domain size was influenced by the degree of polymerization through the polymer main chain. It was noted that BCPs composed of asymmetric blocks did not assemble to well-ordered morphologies, which was attributed to the lack of conformational freedom due to the rigid-rod polymer architecture. Brush BCPs prepared by this route were observed to spontaneously assemble into large ordered nanostructures (>100 nm) [4], which piqued our interest in applying this approach to photonic crystals.

2.2 A Brief Introduction to Photonic Crystals

When the domain periodicities of typical copolymer structures reach hundreds of nanometers, the effective optical lengths of the domains approach visible wavelengths. The resulting periodic modulation of the dielectric function can yield a photonic

bandgap near the visible; within this gap, there are no allowed frequencies at which light can propagate through the material [6]. A one-dimensional photonic crystal (PC), consisting of a stack of alternating layers, is also termed a dielectric (or Bragg) mirror. This simple architecture forms the basis for a variety of modern optical elements, including filters, antireflection coatings, and resonant cavities.

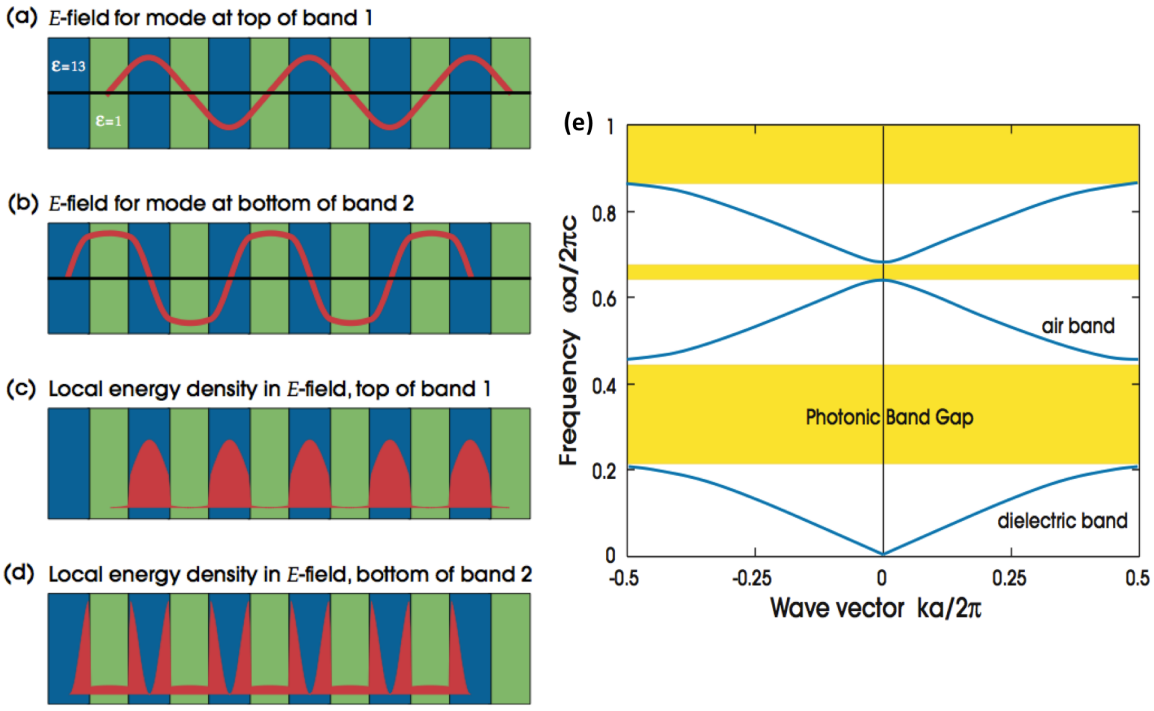

Figure 2.2: Field Profiles and Bandstructure of a 1D Photonic Crystal. An alternating multilayer structure results in a gap between the dielectric band and the air band, where there are no allowed propagation modes. Images from Reference [6]

Figure 2.2 depicts the optical field profiles and resulting photonic bandstructure of an alternating dielectric/air multilayer. At frequencies where the optical length of the repeat unit $(n_1x_1 + n_2x_2)$ approaches integer multiples of the half-wavelength $(\lambda/2)$, the coherently reflected waves interfere constructively, resulting in strong reflection within a specific optical band. The dielectric contrast between the layers is proportional to the reflected intensity at each interface $R = (n1 - n2/n1 + n2)^2$, as well as the width of the photonic bandgap. Typically, photonic crystals fabricated by "top-down" methods are engineered to employ high dielectric contrast, to minimize the total number of layers required to achieve near-unity reflection. In our work, we

demonstrate broadband reflection into the NIR with two low-index materials, with a refractive index contrast of approximately 0.1. Because self-assembly methods easily provide dozens to hundreds of layers, a reflection coefficient of unity can, in principle, be obtained.

2.3 Controlled Assembly of Brush Block Copolymer Photonic Crystals

Traditionally, PCs have been fabricated using top-down techniques such as layer-by-layer stacking [7], electrochemical etching [8], multibeam holography [9], and phase mask lithography [10]. These techniques offer the advantage of precision but require complex apparatuses and many processing steps. Colloidal assembly represents a bottom-up approach to PC fabrication [11, 12], although it is generally limited to face-centered cubic geometries. While colloidal templating is rapid and inexpensive, infilling with high refractive index inorganic materials is usually required to access a full photonic bandgap [11, 12]. BCP nanostructures offer an attractive solution because they can be prepared from commodity chemicals and synthetically tuned to yield a wide range of geometries and functionalities with unique chemical, mechanical, and optical properties.

The lactide (L) and styrene (S) based MMs employed in this study were synthesized from *exo*-norbornene functionalized initiators, suited for the ring opening polymerization of racemic L and the controlled radical polymerization of S. The MMs had similar MWs and narrow molecular weight distributions (MWDs), as characterized by the polydispersity index (PDI = Đ = M_w/M_n): (L-MM: $M_n = 6.1 \times 10^3$ g/mol, Đ = 1.20; S-MM: $M_n = 5.7 \times 10^3$ g/mol, Đ = 1.02). More importantly, the advantageous characteristics (i.e., livingness, stability, functional group, and steric tolerance) of Ru-mediated ROMP enable the sequential polymerization of the MMs to BBCPs in high yields with controlled MWs and narrow MWDs (Figure 2.3). The MW of the BBCPs were controlled by the MM to Ru ratio, and ranged from 1.08×10^6 to

6.64×10^6 g/mol, while maintaining relatively narrow MWDs (Đ = 1.07 –1.58) considering the ultra-high MWs, highlighting the robustness of ROMP. For this study, we targeted blocks with near equal weight ratios with the goal of achieving lamellar nanostructures. After preparing a series of well-defined BBCPs with a broad range of MWs, we investigated a number of simple self-assembly methods to yield thin, solid films. Our annealing methods included controlled evaporation from dichloromethane (DCM) and tetrahydrofuran (THF) solutions, before and after thermal annealing, as well as direct thermal annealing of the solid polymer powder under compression between two glass substrates. The drastic effect of the assembly method on the resulting nanostructures is most starkly visualized by a single BBCP ($M_{\mathrm{n}} = 2.94 \times 10^6$ g/mol), which appeared blue when cast from DCM, green when cast from THF, and red after thermally annealing the green film cast from THF (Figure 2.3(c)). Quantitative reflection measurements were performed on a spectrophotometer equipped with an integrating sphere diffuse reflectance accessory. The reflection spectra confirm the large differences between samples prepared by different annealing procedures (Figure 2.4(a)). For the sample shown in Figure 2.4, the first (longest wavelength) peak of reflection shifts by hundreds of nanometers, depending on the method of film preparation. The difference in color is not due to residual solvent; the films are completely dry, and we did not observe any color change upon placing a sample in high vacuum for more than 50 hours.

Scanning electron micrograph (SEM) cross-sections were used to directly image the film morphologies to further investigate causes of the observed reflection spectra. Although the thermally annealed samples must be composed of larger domains than the films prepared via controlled evaporation (as suggested by the greater λ_{max}), we were curious as to why the film cast from DCM provided the markedly altered reflection spectra. SEM images provided insight into the self-assembly of the films from different techniques, clearly visualizing the polymer morphologies and domain sizes (Figure 2.4(be)). For this polymer, all of the films, except those prepared from DCM, showed the expected stacked lamellar morphology for symmetric BCPs. In the case of the film cast from DCM, a disordered morphology is observed in the SEM image.

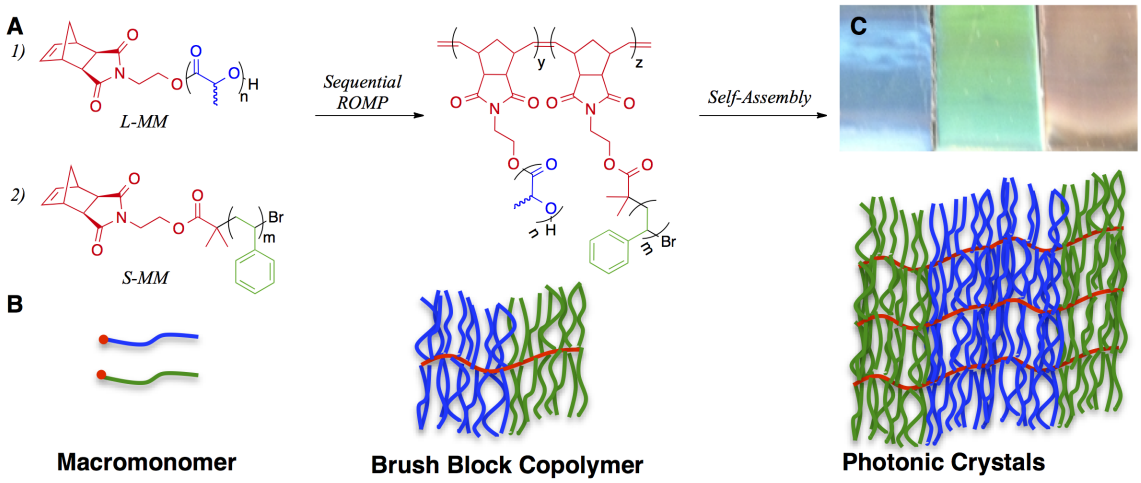

Figure 2.3: (a) S- and L-based MMs were sequentially polymerized by ROMP to BBCPs. (b) A schematic representation depicts the BBCPs and their assembly into ordered lamellar nanostructures. (c) Different annealing techniques render unique PCs for the same polymer, as shown in this photograph.

The evaporative self-assembly process is dictated by a number of factors, including the kinetics of evaporation, quality of solvent, and S/L interaction parameters, as well as the energetics of the glass/polymer interface. For many samples, the degree of lamellar order decreased as a function of distance from the glass interface. For BCPs with approximately equal volume fractions, the lamellar morphology is the most thermodynamically stable, as it minimizes the interfacial surface energy between the two constituent polymers. THF afforded larger domains of higher fidelity than DCM, which we attribute to the fact that it is a good solvent for this copolymer system [13]. In addition, its decreased volatility affords improved chain mobility: rearrangement occurs during evaporation, before the chains enter the glassy state once all solvent is removed. After thermal annealing, these samples become more ordered, with larger domain sizes, as observed in the SEMs and evidenced by the reflection spectra. Films that were directly thermally annealed from dry polymer powder also formed well-ordered lamellae with long wavelength reflection. The improved reflection coefficient is a consequence of film thickness. We observed the first order peak of reflection to be a linear function of MW for all of the self-assembly techniques employed. This is in contrast to a corresponding linear copolymer system, where the domain spacing is

proportional to $MW^{0.81}$ [14]. Because the peak wavelength and domain spacing are directly related by the equation $\lambda_{max} = 2(n_1x_1 + n_2x_2)$ [15], our results suggest that the BBCPs studied yield a larger increase in domain spacing per monomer incorporated than a corresponding linear system. Given the high persistence lengths of these brush polymers [1], we rationalize this observation in terms of the degree of backbone extension enforced by the steric congestion of the brushes. Thus, the brush polymer architecture enables both a large equilibrium scaling for self-assembled structures as well as a very fast equilibration rate, due to the significantly reduced chain entanglement (even at ultra-high MW). Russell and coworkers revealed that these polymers self-assemble with the grafts aligned parallel to the lamellae, and thus the domain size was directly controlled by the degree of polymerization through the polymer main chain, while the MW of the grafts had a less significant impact on the domain size [16].

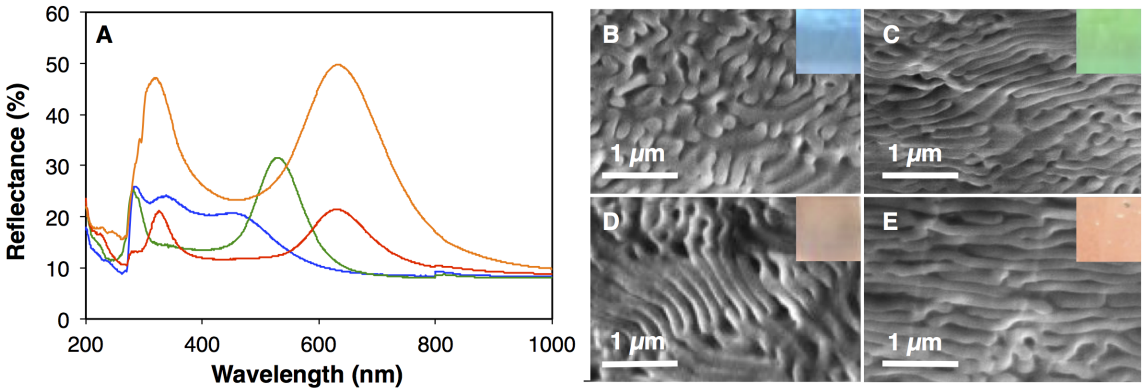

Figure 2.4: (a) Reflection spectra are plotted for the BBCP ($M_n = 2.94 \times 10^6$ g/mol) films prepared from the controlled evaporation from DCM (blue), or THF, before (green) and after (red) thermal treatment, as well as via thermal annealing under compression (orange). (b) SEM cross-sections reveal the morphology of the middle of the BBCP films prepared from the controlled evaporation from DCM (b), THF before (c) and after (d) thermal annealing, as well as by direct thermal annealing under compression (e). The colored insets are photographs of the samples.

Direct thermal annealing of the polymer powders under compression proved to be the most successful assembly technique, in that it enabled ultra-high MW polymers to reach ordered nanostructures with PC characteristics at NIR wavelengths (Figure 2.5(e & f)). By contrast, in the case of controlled evaporation, most of the high molec-

ular weight polymers ($M_n > 3 \times 10^6$ g/mol) did not assemble into films with distinct Bragg reflection peaks. The unmatched structural order achieved through thermal annealing is highlighted by the fact that the ultra-high MW polymers possessed photonic bandgaps well into the NIR (up to $\lambda_{max} = 1311$ nm), an unprecedented wavelength regime for unswelled BCP photonic crystals. Furthermore, the low energetic barriers to reorganization enable the application of any BCP self-assembly technique to our system, to achieve improved lamellar order and optical performance. As NIR dielectric mirrors, these robust solid state PCs enable a host of exciting applications for BCPs to telecommunications and thermal radiation management.

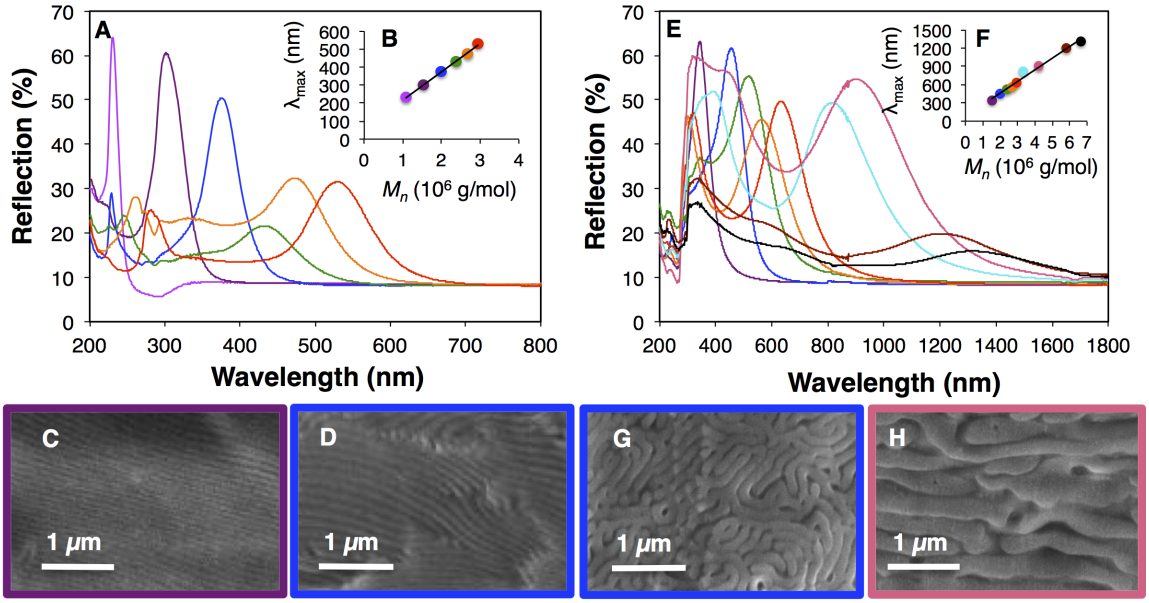

Figure 2.5: (a) Reflectance is plotted as a function of wavelength for the films prepared from the controlled evaporation from THF for several different MW polymers. (b) λ_{max} is plotted against MW for films prepared from the controlled evaporation of THF. SEM cross-sections are shown for the middle of BCP films with $M_n = 1.53 \times 10^6$ g/mol. Linear fit $R^2 = 0.997$. (c) and $M_n = 1.99 \times 10^6$ g/mol (d) prepared from the controlled evaporation of THF. (e) Reflec- tance is plotted as a function of wavelength for the films prepared by thermal annealing under compression for several different MW polymers. (f) λ_{max} is plotted against MW for films prepared by thermal annealing under compression. SEM cross-sections are shown for the middle of BCP films with $M_n = 1.99 \times 10^6$ g/mol. Linear fit $R^2 = 0.984$. (g) and $M_n = 4.21 \times 10^6$ g/mol (H) prepared by thermal annealing under compression.

2.4 Optical Modeling

To justify the proposed mechanism of the observed reflection spectra, transfer matrix simulations [15] were employed to model the reflection spectra of the polymer photonic crystals (Section 8.1). The complex refractive indices of each block were measured for the corresponding brush homopolymers by ellipsometry. The inputs to our script are the frequency-dependent refractive indices, measured first order peak of maximum reflectance, number of layers approximated by SEM, and the weight fractions of each block measured by NMR. An initial guess of the size of each block domain was made using the first order peak of reflection, using the equation $\lambda_{max} = 2(n_1x_1 + n_2x_2)$, assuming equal polymer densities. To account for the increased bandwidth of the reflection peaks due to size dispersity and disorder in the nanostructure, two free parameters were introduced: coefficients of variation (CVs) for layer thickness and phase decoherence. Introducing partial phase decoherence in transfer matrix simulations has been previously demonstrated as a means of approximating interfacial roughness [17]. A normal distribution of thickness and phase perturbation was used, averaged over 1000 simulations, and smoothed to remove noise. Simulation details can be found in Section 8.1, the MATLAB source code is available in Reference [18].

The angle dependent reflection spectra of a well-ordered sample were measured and compared with one-dimensional transfer matrix simulations. The angular frequency response shows good agreement between experiment and simulation 2.6(a). We attribute the difference in amplitude to the angular variation due to the curvature of the lamellae and the differences between the fitted and actual complex refractive indices. Additionally, simulations were run for three samples formed by three different assembly procedures, with different MWs representative of the full range of the series studied (Figure 2.6(b-d)). For our simulations, the CV for the layer thicknesses was chosen to be 10%, which we found to be large enough to demonstrate the effect of size distribution on the line widths of the optical spectra, while small enough to clearly resolve the higher order peaks. Partial phase decoherence further contributes to peak broadening, and is well rationalized considering the roughness observed by

SEM [17]. The qualitative features of the measured spectra are well represented in the simulations (Figure 2.6). Our modeling strongly suggests that the observed lamellar nanostructures consist of alternating polymer layers, which represent 1D photonic crystals. Despite the moderate to poor lamellar alignment observed in the SEM cross-sections, our 1D transfer matrix simulations can qualitatively predict reflection spectra, enabling the design of optical components using this platform.

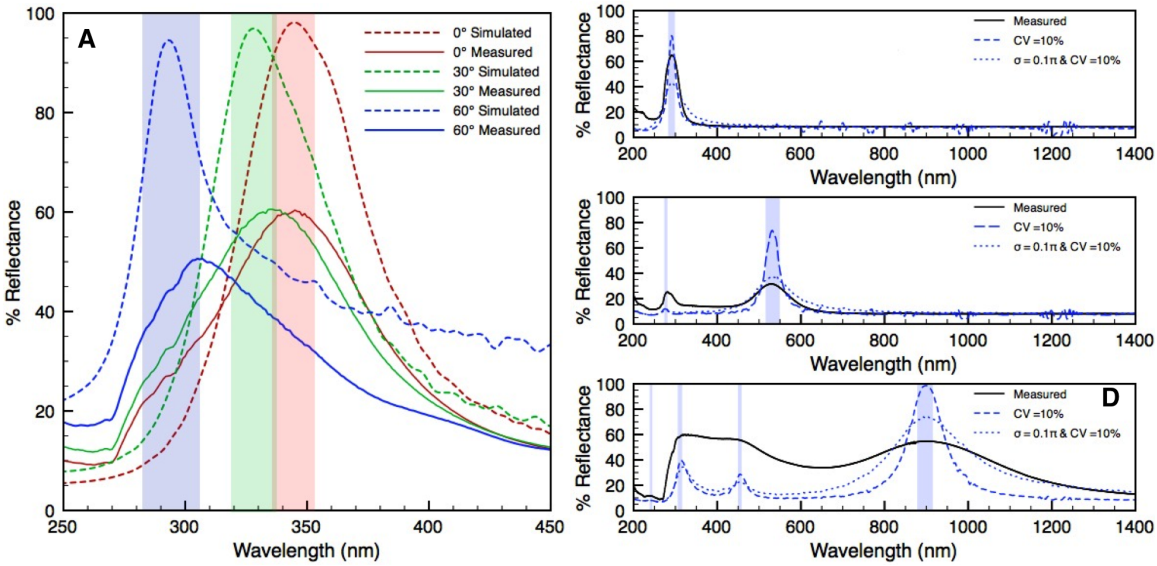

Figure 2.6: (a) The angle-dependent reflection of a film thermally annealed under compression from a BCP with M_n = 1.53 $\times 10^6$ g/mol shows good agreement between the simulated (dashed, size CV = 10%, no decoherence) and measured (solid) spectra. Simulated (dashed, size CV = 10%, with and without partial decoherence) and measured (solid) reflection spectra of three different samples are shown: (b) M_n = 1.53 $\times 10^6$ g/mol, evaporated from DCM, (c) M_n = 2.94 $\times 10^6$ g/mol, evaporated from THF, (d) M_n = 4.21 $\times 10^6$ g/mol, thermally annealed under compression. The shaded areas represent the photonic bandgaps simulated for perfect alternating multilayers with no layer thickness dispersity.

2.5 Tunable Assembly from Rigid Polymer Brushes

Although the reported BBCPs can assemble to IR-reflecting PCs after thermal annealing, we sought to develop a system that could assemble to such domain sizes under ambient conditions in order to enable widespread applications, including infrared-

reflecting paints. We envisioned that increasing the rigidity of the grafts would enhance the overall persistence length of the BBCP, further decreasing chain entanglement and promoting more rapid self-assembly of ultrahigh MW BCPs to even larger domains. The synthesis of BBCPs constructed from rigid isocyanate-based MMs enabled rapid self-assembly of visible and infrared-reflecting photonic crystals through controlled evaporation at ambient temperature. Figure 2.7.

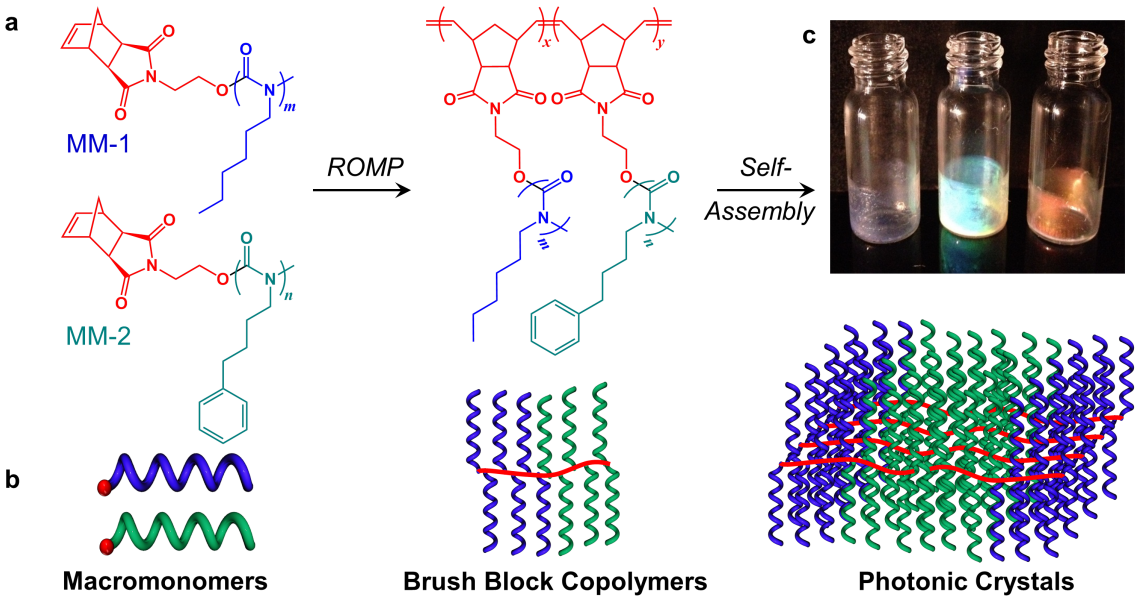

Figure 2.7: (a) Structures of isocyanate-based macromonomers and their ROMP to brush block copolymers. (b) Schematic representation of the synthesis of brush block copolymers from rigid-rod helical macromonomers and their self-assembly toward 1D photonic crystals. (c) Photograph of photonic crystals reflecting violet, green, and red light.

Polyisocyanates are a class of polymers that adopt rigid helical secondary structures[19–21]. In the case of brush copolymers composed of a polystyrene main chain and polyhexyl isocyanate side chains, it has been shown that the rigid side chains result in main chain elongation, compared to similar graft copolymers with random coil side chains [22]. We identified isocyanate-based MMs as promising candidates to investigate whether increased side chain rigidity would facilitate self-assembly to large domain sizes and long-wavelength reflecting PCs. Additionally, the controlled polymerization of isocyanates has been well established by Novak and co-workers utilizing half-titanocene (IV) alkoxide initiators, where the alkoxide group is quantita-

tively incorporated as a chain-end group on the polyisocyanate, providing an efficient means to prepare appropriately functionalized MMs.[23, 24] Embracing Novak's synthetic approach, an *exo*-norbornene half-titanocene derivative (**4**) was conveniently prepared in good yield from the reaction between $CpTiCl_3$ and N-(hydroxyethyl)-*cis*-5-norbornene-*exo*-2,3-dicarboximide in the presence of Et_3N. Complex **4** was subsequently employed to produce *exo*-norbornene functionalized MMs from hexyl isocyanate (HICN, MM-1) and 4-phenyl butyl isocyanate (PBICN, MM-2). These MMs exhibited similar MWs (weight average MW (M_w) = 6.77 and 5.99 kDa for MM-1 and MM-2, respectively) and narrow molecular weight distributions (Đ = 1.05 and 1.07 for MM-1 and MM-2, respectively). The ROMP of MM-1 and MM-2 initiated by **3** was efficient, and could be carried out over a broad range of [MM]:[1] ratios, achieving high MM conversion, producing high MW copolymers with narrow MWDs. Closer examination of the ROMP of MM-1 shows that it exhibits living characteristics (i.e., linear increase in MW with increasing MM conversion, and a nearly constant PDI during the course of polymerization) necessary for successful synthesis of well-defined BCPs in a one-pot synthetic procedure.

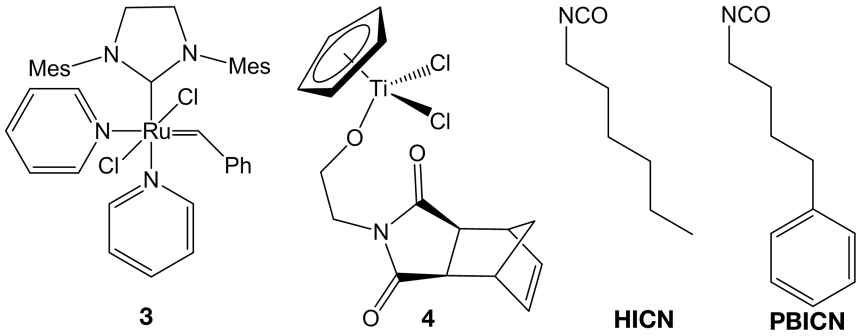

Figure 2.8: Initiators and monomers for synthesizing poly(isocyanate) brushes.

With a series of well-defined BBCPs in hand, we investigated the facile self-assembly of these polymers to PCs. Thin films of the polymers were prepared through controlled evaporation from DCM, THF, $CHCl_3$, or toluene. In contrast to the previously reported lactide/styrene BBCPs, no significant solvent effect was observed on self-assembly, as judged by the nearly identical reflectance spectra and λ_{max} of the films. The self-assembly of these BBCPs to ordered thin-films is dictated through

a delicate interplay of factors, including solvent, kinetics, polymer interactions, and polymer/substrate interactions.[25] Our preliminary explanation for the negligible solvent effect is that the rigid architecture of the isocyanate BBCPs promotes a highly elongated main chain, minimizing solvent as well as polymer interactions. This represents a degree of pre-organization, which accelerates self-assembly to ordered morphologies. As such, films prepared from the controlled evaporation of DCM solutions were analyzed because it is the most volatile solvent and most strongly highlights the rapid self-assembly of the BBCPs. The rapid self-assembly of the BBCPs is qualitatively observed in that the samples with MWs of 1512, 2918, and 4167 kDa produced films that visually appeared violet, green, and red, respectively.

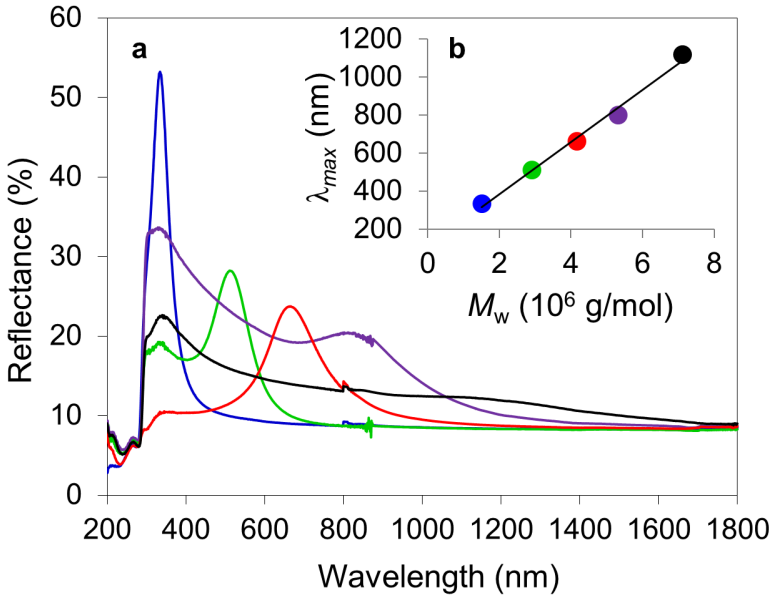

Figure 2.9: (a) Plot of reflectance as a function of wavelength for isocyanate-based BBCP thin films with $M_w = 1512$ (blue), 2918 (green), 4167 (red), 5319 (purple), and 7119 (black) kDa. (b) Plot of λ_{max} as a function of M_w. Color scheme corresponding to M_w is consistent with (a).

To quantitatively measure the PC properties of these materials, reflectance measurements were acquired as a function of wavelength using a spectrophotometer (Figure 2.9(a)). As expected, the violet, green, and red polymer films showed primary reflectance peaks with $\lambda_{max} = 334$, 511, and 664 nm, respectively. It is important to note that the magnitude of reflectance is directly related to the number of layers

in the 1D PC. Therefore, as the thickness of the film was not strictly controlled, a variation in percent reflectance was observed. In theory, optimization of the layer thickness can lead to 100% reflectance at the appropriate wavelength. The BBCP with the next highest MW (5319 kDa) in the series exhibited two broad reflectance peaks at 329 and 801 nm. In the case of the ultrahigh MW BCP ($M_{\mathrm{w}} = 7119$ kDa), extremely broad reflectance was seen extending from 1800 to 300 nm, with a λ_{max} of the primary reflection peak estimated at the plateau with $\lambda_{max} = 1120$ nm. Although the broad signals in the reflection spectrum suggest poor self-assembly, the ability to produce broadly reflecting materials could be desirable in an IR-reflecting building material. The possibility that the domain sizes of the films could be swollen from residual solvent is eliminated because the film properties are unchanged after being dried under vacuum overnight and are stable over the course of at least months at ambient conditions. For comparison, with the lactide/styrene BBCPs, the highest MW polymer that was able to self-assemble through controlled evaporation to a PC structure had a MW of 2940 kDa, with $\lambda_{max} = 540$ nm. Thus, the reflectance data clearly shows that the isocyanate-based BBCPs are superior in regards to facile self-assembly to PCs. Specifically, under less strenuous self-assembly conditions, ultrahigh MW (>7000 kDa) isocyanate-based BBCPs can reflect light with $\lambda_{max} =$ 1120 nm, more than 580 nm longer than the lactide/styrene system. Closer inspection of the primary reflection peaks reveals a highly linear correlation between λ_{max} of this peak with increasing MW of the BBCP ($R^2 = 0.990$), which is in accord with our earlier reported lactide/styrene BBCP PCs (Figure 2.9(b)). As λ_{max} is directly determined by the domain sizes, this observation shows that, within the window of our investigations, there is a linear increase in domain sizes with increasing BCP MW. In contrast, most linear BCPs exhibit a nonlinear increase in domain size with increasing MW that scales theoretically as $MW^{2/3}$.[26] Thus, the rigid architecture and inhibited chain entanglement of BBCPs maintains structural integrity as they self-assemble into ordered morphologies, which allows larger domain sizes to be accessed with fewer number of monomer repeat units than their linear counterparts. This predictability in reflectance enables these PCs to be easily incorporated into a

variety of specific applications, because the reflectance can be readily tuned through the synthetic manipulation of the polymer MW.

Because the domain sizes directly scale with the MW of the BCP, the wavelength of reflected light can be predictably modulated by synthetically controlling the MW of the polymer.[18] Although this approach successfully produces PCs that reflect target wavelengths of light, it requires that a specific MW BBCP be synthesized to reflect each wavelength of light; a more flexible and desirable technology would be post-synthetically tunable, bypassing such application-specific synthetic requirements.

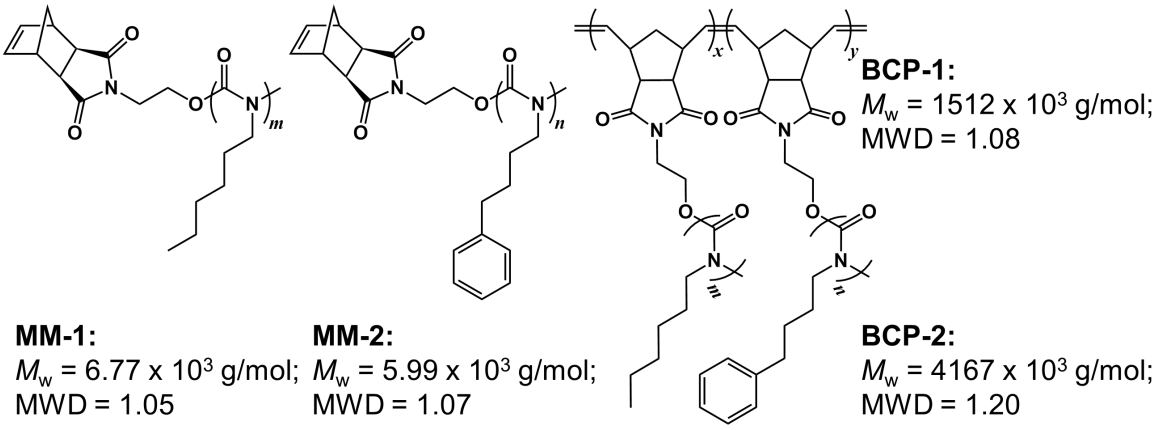

Figure 2.10: Structures and molecular-weight properties of the isocyanate macromonomers and brush block copolymers utilized in the blending study.

In the case of linear, random-coil symmetric BCPs, it has been demonstrated that polymer blends of BCPs of two different MWs can self-assemble to stacked lamellar morphologies if the ratio of the polymer MWs is less than five.[27–29] The resulting size is an average of the relative ratio of the two components and is permitted by the flexibility of linear random-coil BCPs as they access low-energy morphologies, minimizing interfacial energy through a proposed mechanism involving stretching of the low-MW BCP and a compression of the high-MW BCP. Similar blends of linear BCPs, in the presence of a swelling solvent and shear alignment, can exhibit temporary PC characteristics (reflecting light across the visible spectrum), which are lost upon solvent evaporation.[30] Thus, we were motivated to investigate if blends of BBCPs of different MW could afford analogous morphological compromise, despite their inherently rigid architectures, as a means to readily modulate the domain sizes

and thus the bandgaps of the PCs. Using this technique, it was found that the wavelength of reflected light is precisely tunable across the visible spectrum of light and into the NIR region simply through controlling the relative incorporation of the two polymers, greatly enhancing the practicality of BBCP PCs.

The two BBCPs of different MW employed in this study were constructed through sequential ROMP of equal amounts of *exo*-norbornene-functionalized hexyl isocyanate (MM-1) and 4-phenyl butyl isocyanate (MM-2) MMs (Figure 2.10). A film of the lower-MW BBCP (BCP-1: weight average MW [M_{w}] = 1512 $\times 10^3$ g/mol, molecular weight distribution [MWD] = 1.08), prepared by the controlled evaporation from dichloromethane, exhibited a maximum peak reflectivity (λ_{max}) of 360 nm, while the film of the higher-MW BBCP (BCP-2 : M_{w} = 4167 $\times 10^3$ g/mol, MWD = 1.20), prepared in identical fashion, exhibited a λ_{max} = 785 nm. A film prepared from the controlled evaporation of a solution of BCP-1 and BCP-2 in a weight-percent ratio of 50:50 in dichloromethane exhibited a single reflection peak with λ_{max} = 541 nm. By varying the weight-percent ratio of the two BBCPs from 100% BCP-1 to 100% BCP-2, at 10% intervals, a total of 11 different films were prepared. Each PC film showed a primary reflection peak, with λ_{max} observed at increasing wavelengths of light with increasing incorporation of BCP-2. Most impressively, a highly linear trend (R^2 = 0.989) in increasing λ_{max} as a function of increasing percentage of BCP-2 was established, thus allowing the production of PCs that reflect all wavelengths of light across the visible spectrum and into the NIR (Figure 2.11).

These results strongly suggest that despite the rigid architecture of the BBCPs, the blends of the two polymers of different MW are able to assemble to uniform domains, in which the size is dictated by the relative ratio of the two components. We have previously established that the BBCPs rapidly self-assemble to stacked lamellae. However, the mechanism by which the blends form such uniform domains remained unclear. The two most obvious routes would include the conforming assembly of the blends to stacked lamellae, in which the domains scale as an average of the two BCPs, similar to the mechanism followed by linear BCPs, or through a gradual change to an entirely different polymer morphology to compensate for the varying ratios of the two

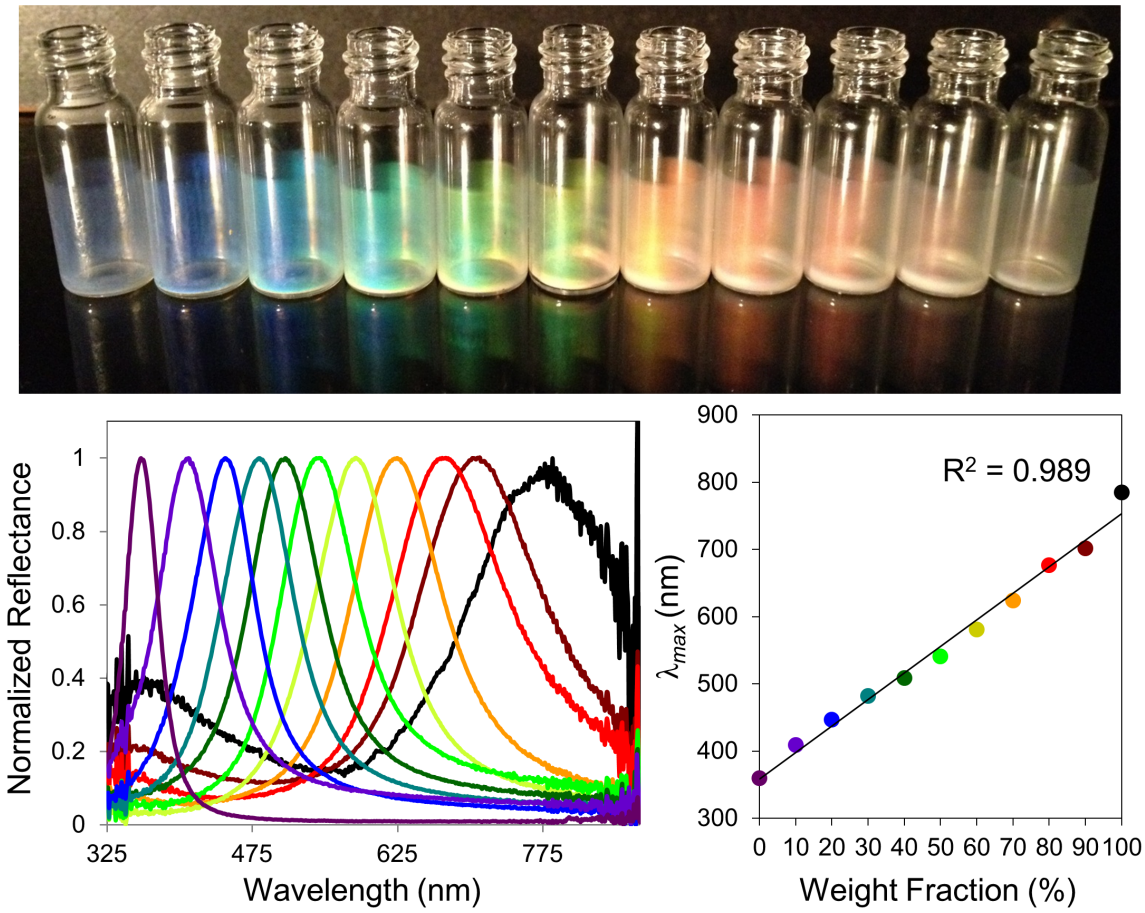

Figure 2.11: (a) Photograph of brush block copolymer blends reflecting light across the visible spectrum (top). Plots of (b) reflectance against wavelength, and (c) maximum peak wavelength of reflectance against weight fraction of blend (% BCP-2) of the different brush block copolymer blends

BCPs. To gain insight into the blending mechanism, scanning electron microscopy was utilized to visually image the morphologies of the films.

For all BCP blends, highly ordered stacked lamellae were observed in the SEM analysis (Figure 2.12). These data strongly support the proposal that the BCPs of different MW are able to adopt structures similar to their linear analogues,[27–29] thus necessitating an elongation of BCP-1 and a structural distortion of BCP-2. Although it is highly unlikely that the BBCPs are able to participate in extreme chain folding because of their inherently rigid structures, bending of BCP-2 to access the lowest-energy state must be occurring to explain the resulting highly uniform domains of the blends.

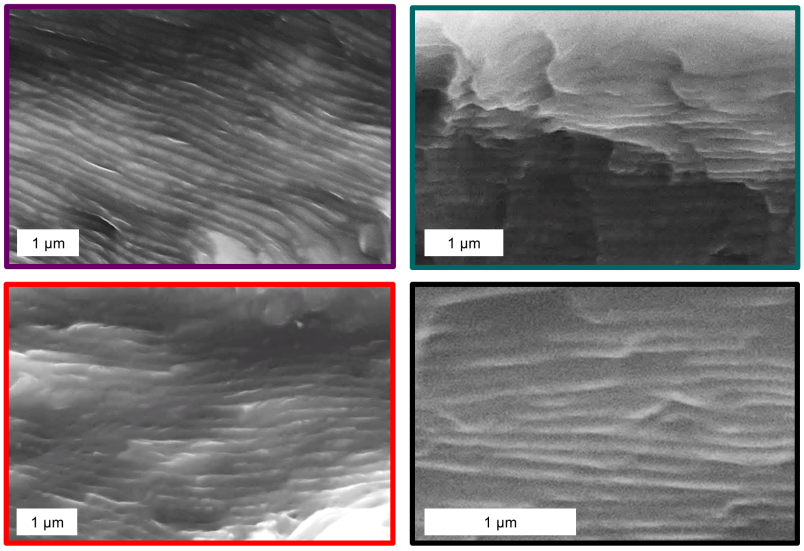

Figure 2.12: SEM images of cross-sections of brush block copolymer blends with a) 0%, b) 30%, c) 80%, and d) 100% of BCP-2. The perspective places the glass substrate parallel with the text.

We have shown that blends between BBCPs of different MW form highly uniform, stacked lamellar morphologies. The resulting domains of the 1D PC architectures scale linearly with the weight-percent incorporation of the two polymers. Thus, a wide range of photonic-band-gap materials can be easily fabricated, simply through blending of two polymers. Because the rigid architecture of BBCPs greatly minimizes chain entanglement, these blends rapidly self-assemble through controlled evaporation from a volatile solvent. Despite their rigidity, there appears to be sufficient flexibility to conform to uniform, layered structures. We foresee that this simple, bottom-up, approach provides an attractive means to precisely tunable photonic band gap materials through the rapid self-assembly of BBCP blends.

2.6 High-fidelity Multilayers from Dendritic Copolymers

One downside of the bottom-up approach of BC self-assembly to PCs is that any morphological disorder results in inefficiencies of the reflector. Especially in precision optics, such inefficiencies are intolerable, and must be eliminated. The molecular BBCP

architecture consists of three polydisperse components: the two macromonomer side chains and the unifying polymer main chain. Because the combination of these nonuniformities could result in morphological disorder (and thus inefficient PCs), we investigated the polymerization of discrete monomers that would still impart steric effects necessary to minimize chain entanglement and enforce a rigid-rod BC main chain.

Although polydispersity is known to enhance the self-assembly of linear BCPs to uniform morphologies [31–34], we hypothesized that minimizing the elements of polydispersity in the polymers could enable the fabrication of more uniform and efficient dielectric mirrors. Despite the fact that the polymeric side chains align parallel with the lamellae, their dispersity could influence nonuniform packing, promoting lamellae curvature, domain size variability, and bandwidth broadening. Near the polymer chain ends, the degree of steric congestion is reduced and the polymeric side chains become perpendicular to the lamellae. In this region the polydisperse polymeric side chains could further increase the dispersity in the lengths of the BBCPs, leading to nonuniform assembly. Intuitively, it could be assumed that main-chain dispersity would have the greatest impact on the ability of the polymer to assemble to highly ordered morphologies. However, we have recently shown that main-chain dispersity is not a large deterrent, as blending two different MW BBCPs (with identical side chains and different degrees of main-chain polymerization) can afford well-ordered morphologies where the domain sizes scale with the weight incorporation of the two components. Regardless, in the context of precision dielectric mirrors, domain size dispersity must be eliminated.

To further probe this topic, we explored the possibility of utilizing discrete monomers that can still produce BCPs with a highly elongated, rigid polymer architecture to reduce the dispersity in the system to increase the fidelity of the dielectric mirrors. It has been demonstrated that dendronized polymers exhibit a minimal degree of chain entanglement due to the steric repulsion between pendant monodisperse wedge side groups.[35–38] Thus, we believed dendronized polymers to be an ideal platform to test our hypothesis. Additionally, as the molar mass of a dendritic monomer can

be considerably less than a macromonomer, an equivalent degree of polymerization within the main chain for both types of polymers would produce dendronized polymers with a significantly reduced MW in comparison to BBCPs. The reduced MW of the dendronized polymer would presumably increase diffusion rates and enhance the rate of self-assembly. Here we report the sequential ROMP of *exo*-norbornene functionalized wedge-type monomers to dendronized BCPs and their self-assembly to highly ordered stacked lamellar nanostructures (Figure 2.13).

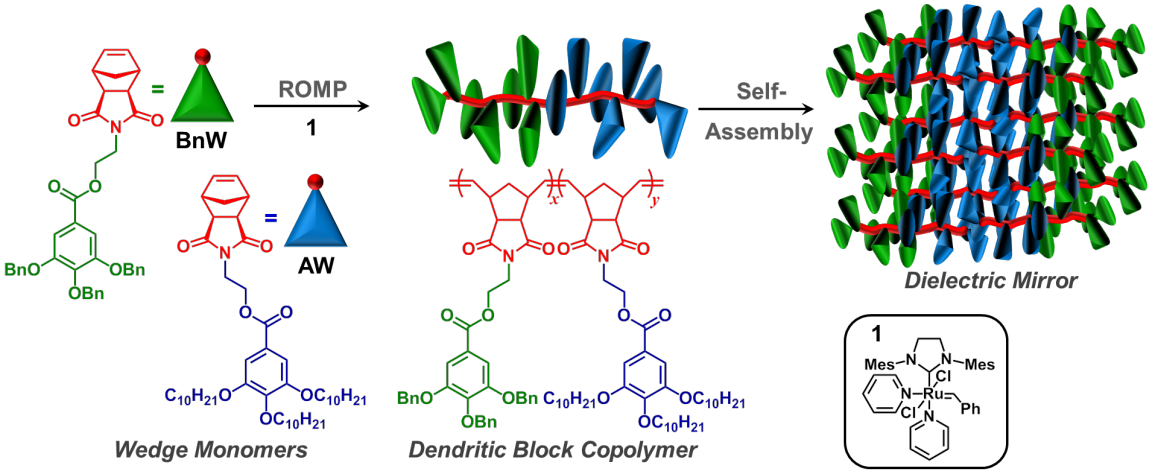

Figure 2.13: Structures of wedge-type monomers and their ROMP to dendronized BCPs. The schematic represents the corresponding synthesis and self-assembly to narrow bandwidth dielectric mirrors.

Details of synthesis can be found in [39]. The films fabricated from the dendronized BCPs possessed significantly narrower bandwidths than our previously reported isocyanate BBCPs with comparable λ_{max}. To directly compare the bandwidths of these dendronized BCP dielectric mirrors with our previously reported results, we calculated the gap-midgap ratio (GMR) by dividing the measured full width at half the λ_{max} (fwhm = $\Delta\lambda$) / λ_{max} (Figure 2.14).

The GMRs of the 1D photonic crystals produced from dendronized BCPs were much smaller (GMR = 9-18%) than from the isocyanate-based BCPs4b,c (GMR = 17-27%) for PCs that reflected light across the visible spectrum (λ_{max} = 334-768 nm). To compare the current PCs with theoretically perfect reflectors, we computationally calculated the GMRs for PCs possessing identical refractive indices as the dendronized

dendronized BCPs			brush BCP		
M_w (kDa)[a]	λ_{max} (nm)[b]	GMR (%)[c,d]	M_w (kDa)[a]	λ_{max} (nm)[b]	GMR (%)[c]
480	330	9 (5)	1512	334	17
570	393	13 (4)	2918	511	25
1250	768	18 (2)	4167	664	27

[a]Determined by light scattering. [b]Determined by spectrophotometer with integrating sphere. [c]GMR = gap−midgap ratio, determined by fwhm/λ_{max}. [d]The number in parentheses represents the theoretical values of the gap−midgap ratio with zero dispersity.

Figure 2.14: Comparison between Bandwidths of Dendronized BCPs and Isocyanate Brush BCPs

BCPs but no layer thickness dispersity. The perfect PCs with identical λ_{max} as the dendronized BCPs had GMRs ranging from 5 to 2%.

We attribute the striking difference between the BCP systems to the fact that the polydispersity in the side groups was eliminated by replacing macromolecular repeat units with well-defined discrete groups, yielding more unified "building blocks" for the formation of highly ordered stacked lamellar morphologies. Additionally, the reduced polymer MW for dendronized BCPs, because of the lower MW of the repeat unit, most likely enables faster diffusion and assembly. In both systems, as the MW of the BCPs is increased, bandwidth broadening is observed, suggesting increased disorder in the bulk morphology. In order to overcome the kinetics for reorganization, the samples were annealed at 100 °C for 24 h. Thermal annealing induced a noticeable red shift ($\Delta\lambda_{max}$ varying from 75 to 345 nm) along with increased bandwidth broadening and decreased reflectance intensity for samples with MW ranging from 480 to 1390 kDa. One hypothesis is that the χ between these very chemically similar monomers is not large enough to enable thermal annealing. Because the effective χ is reduced as the temperature increases, heating can favor mixing, reducing the fidelity of the films, if the χ interaction parameter is low.

Cross sections of freeze-fractured films were stained with RuO_4 and examined by scanning electron microscopy. For the films produced by dendronized BCPs with MW lower than 1390 kDa, stacked lamellar morphologies were observed, as expected for the symmetric BCPs[40]. Remarkable long-range order was observed throughout the

entire bulk of the film, ranging from ∼100-200 uniform layers of alternating domains for the samples with M_w = 480 and 570 kDa. These multilayer films show unprecedented order for BCPs in this size regime. Unfortunately, an increase in MW resulted in a rapid loss in ordering, which was attributed to the dominating influence of chain entanglement that increases the energetic barrier for reorganization. Comparison of the SEM cross sections before and after annealing (Figure 2.15) revealed some improvement in long-range order for samples with M_w = 1390 and 1940 kDa samples, in addition to lamellae thickening (1.3 times on average) for all samples. A significant overall evolution in morphology was detected for the film prepared from the BCP with M_w = 1390 kDa (Figure 2.15(i)). Initially, a poorly defined morphology was observed at the polymer-air interface. After annealing, stacked lamellae with domain sizes ranging between 380 and 400 nm were observed.

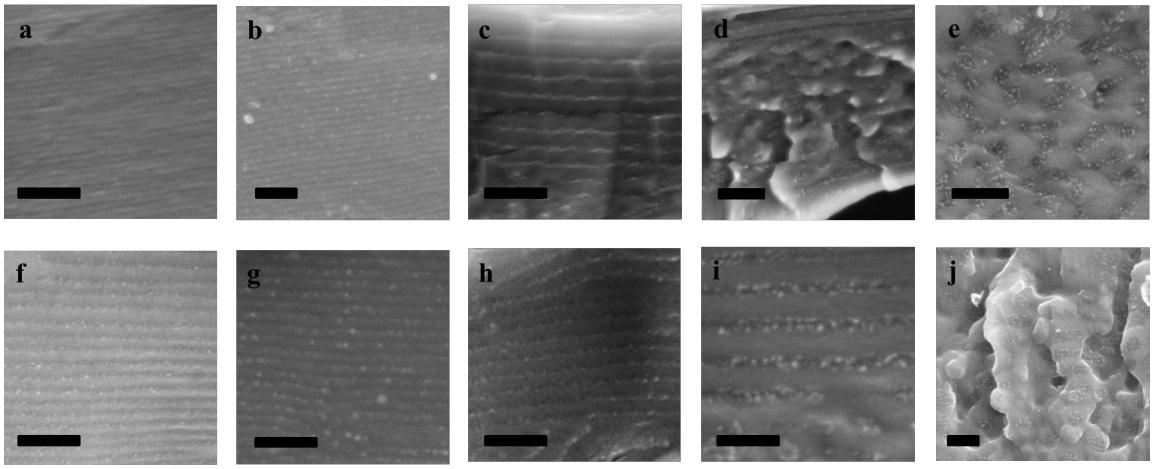

Figure 2.15: SEM cross sections of dendronized BCPs films prepared by controlled evaporation from DCM with M_w = 480 kDa (a, f), 570 kDa (b, g), 1250 kDa (c, h), 1390 kDa (d, i), and 1940 kDa (e, j). Scale bar = 1 μm.

The film produced from the highest MW polymer (M_w = 1940 kDa) also demonstrated a drastic change in morphology. The original sample produced by controlled evaporation from DCM lacked long-range order and exhibited scattered elongated raspberry-like (∼1-1.5 μm long and ∼0.25 μm wide) features (Figure 2.15(e)). Upon annealing, an overall reorganization to a somewhat periodic arrangement, resembling a cylindrical morphology, was observed (Figure 2.15(j)). Similarly, the raspberry-

like features were noted for the 1390 kDa sample at the polymer-substrate interface before thermal annealing. These similarities suggest that before the system reaches the thermodynamic minimum, corresponding to a lamellar morphology, it undergoes a series of metastable states, which become kinetically trapped with the high MW polymers. Even extended annealing (120 h) was unable to annihilate the morphological disorder for the polymer with $M_{\mathrm{w}} = 1940$ kDa. The lack of morphological order for the ultrahigh-MW dendronized BCPs explains the lack of any resonance optical reflection. SEM analysis revealed a minimal change in morphology, which remotely resembled stacked lamellae. We hypothesize that the lamellar morphology evolution occurs through several stages, proceeding through a disordered morphology into a lower energy, metastable morphology, en route to the final thermodynamic minimum.[41] This reorganization becomes exceedingly slow with an increase in the BCP MW. The combination of the reflectance and SEM analysis suggest that the reduced MW of dendronized BCPs, in comparison to BBCPs, allows their more rapid self-assembly to highly ordered PCs. However, the less rigid architecture of dendronized BCPs experiences a higher degree of chain entanglement, which inhibits the ultrahigh-MW polymers from rapidly reaching equilibrium, instead trapping them in a metastable state. Taking into account the annealing-induced morphological evolution observed by SEM, we attempt to explain the changes in the reflectance profiles of dendronized BCPs upon annealing. The shift in λ_{max} is caused by the increase in domain spacing induced by enthalpy-driven thickening of lamellae. However, the thickening was not uniform throughout the bulk of the material, resulting in the domain dispersity and the broadening of the reflectance peak.

2.7 A Modular Blending Strategy for Improved Assembly

The synthetic difficulty inherent to generating the high-MW BBCPs with low dispersity requires re-optimization of the protocols for each new type of BBCP or macro-

molecular brush architecture. In an effort to further facilitate the use of BBCPs as a synthetic platform for multifunctional materials, we demonstrate the blending low-MW homopolymers (HPs) with BBCPs as a powerful means of manipulating their assembly. Blending short, readily synthesized HPs with BBCPs prior to casting a polymer film allows one to control the lamellar array periodicity between ∼100 and 500 nm, tune the photonic band gaps that can be achieved in these films from the UV all the way to the infrared regime (up to $\lambda \approx 1410$ nm), and incorporate different chemical species into the arrays without the need to develop new macromonomers or re-optimize the BBCP synthesis. It is well known that adding HPs to linear block copolymers causes them to swell in a predictable manner.[42–46] However, it is not necessarily obvious that such a methodology would be readily applicable to BBCPs, which are generally regarded as rigid rods. The increased steric hindrance that causes the BBCP rod-like morphology is the very reason they are able to achieve lamellar arrays with large periodicities in the first place. In an initial study, we probed the extent to which these HPs could change the domain spacing of the BBCP arrays. All target BBCPs in this work are symmetric, containing roughly equivalent numbers of polystyrene and poly(lactic acid) macromolecular brushes (MW ∼3.5 and ∼3.1 kDa, respectively). In each of the blends, the BBCPs were combined with equal amounts of PS and PLA HPs by weight. All relevant polymer MWs and PDIs can be found in Reference [47]. These blends were annealed and the resulting films characterized with reflectance measurements, scanning electron microscopy (SEM), and small-angle X-ray scattering (SAXS) to determine the quality and domain spacing of the self-assembled arrays (Figures Figure 2.16. Despite the relatively rigid nature of the BBCP, incorporating low-MW HPs caused the arrays to swell to ∼140% of the periodicity of the non-blended BBCP (Figure Figure 2.16. Moreover, the relationship between periodicity and HP:BBCP weight ratio followed a linear trend up to 67.5 wt% HP (weight ratio of ∼2:1), beyond which the arrays exhibited a large degree of disorder, most likely indicating that the materials had begun to phase-separate at these loadings of HP additives (Figure 2.16(b)). Self-consistent field theory (SCFT, details in [47]) suggest that the HPs are dispersed evenly throughout both BBCP

blocks, with HPs located in the lamellar blocks containing brushes of the same composition (i.e., PS HP in the PS block), with only slightly larger amounts of HP at the center of the lamellae and the interface between two different blocks (Figure 2.16(c)). As a result, the BBCPs can tolerate the presence of a large amount of added HP before phase segregation occurs.

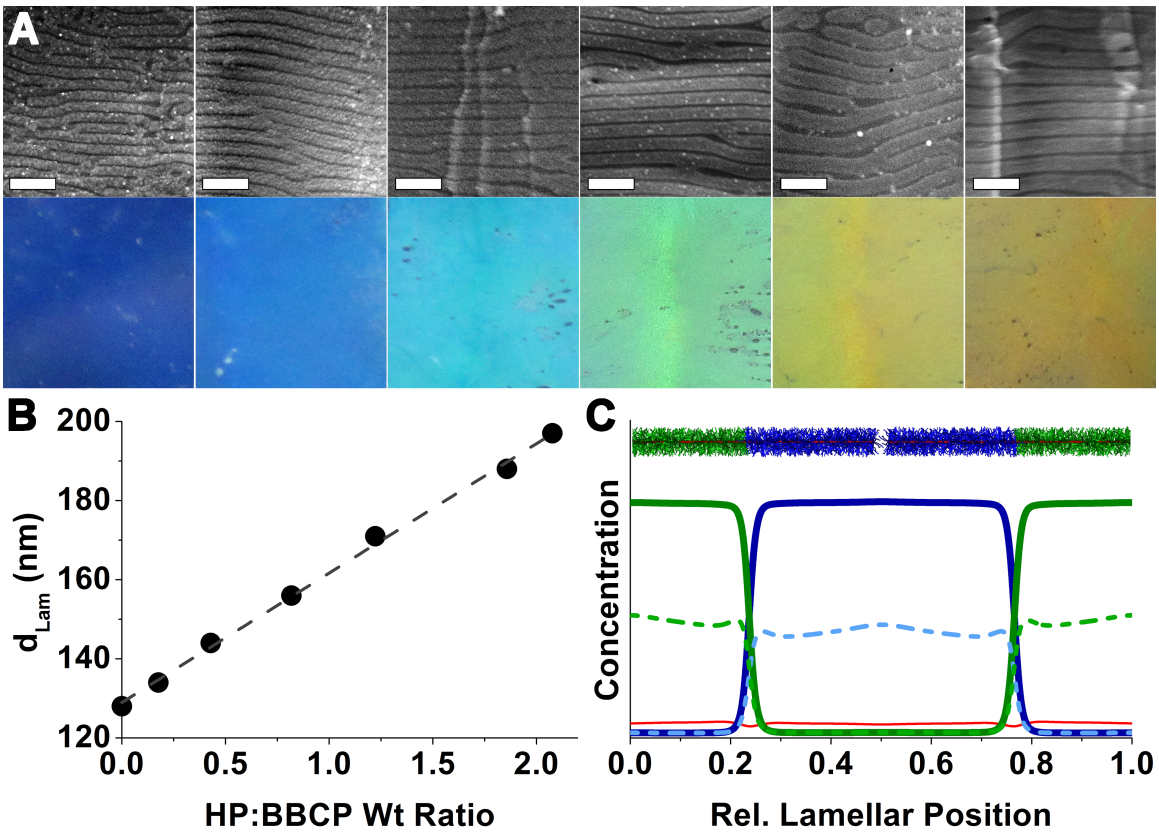

Figure 2.16: (a) SEM cross-sectional images of BBCP arrays with 0, 30, 45, 55, 65, and 67.5 wt% HP (wt ratio of 0 to ∼2); below each SEM image is a plain view image of the film showing increasing photonic band gap positions with added HP. Scale bars are 500 nm. (b) Lamellar domain spacing as a function of added HP (same films as in (a); data obtained via SAXS). (c) Relative concentrations of BBCP brushes and HPs at various positions along a lamella as determined by SCFT simulations: blue traces, PS; green traces, PLA; red trace, the polynorbornene backbone; solid lines, BBCP; dashed lines, HPs. Sample is 45 wt% HP.

To fully investigate the ability of these blends to control the domain spacing of the self-assembled arrays and thus the wavelength of reflected light, a series of BBCPs with overall DP ranging from ∼300 to ∼900 (MW 987-3035 kDa) was synthesized and blended with different amounts of ∼3 kDa HPs. These BBCPs possessed backbone

lengths commensurate with those of the BBCPs previously shown to give highly ordered arrays that reflect light ranging from the UV to the near-IR (up to ∼900 nm). Upon annealing the blends, three interesting observations were inferred from the reflectance spectra (Figure 2.17). First, although the lowest MW BBCP could only be swollen to ∼140% before the quality of the films decreased, higher MW BBCPs could be swollen to accommodate higher levels of HP; they also exhibited a greater degree of swelling with equivalent amounts of HP. The BBCPs could even be swollen to a periodicity that was 180% the value of the corresponding unblended BBCP (Figure 2.17(a)). This increase in the extent to which heavier BBCPs could be swollen is most likely due to the fact that, while higher MW BBCPs possess longer contour lengths, the overall persistence length of this PLA-PS BBCP system is fixed. Thus, the larger BBCPs would be expected to be more contorted in the unblended arrays, allowing for greater swelling upon addition of HPs. Second, the optical properties of the arrays noticeably improved when modest amounts of HP were added, especially for the longest BBCPs (Figure 2.17(b)). Specifically, the values of $\Delta\lambda/\lambda_{max}$ (a measurement of the full-width at half-maximum of the peak relative to the peak maximum) narrowed, indicating greater homogeneity in lamellar periodicity. Additionally, the amount of scattered light at wavelengths outside of the photonic stop bands (e.g., ∼500-750 nm in the 0 wt% system or ∼750-1000 nm in the 65 wt% system) decreased, indicating reduced incoherent scattering from disordered regions of the sample. These phenomena can be explained by the inherent polydispersity of the BBCP backbone lengths. The steric hindrance that the macromonomers impart to the BBCP makes it difficult for the materials to pack into well- ordered lamellae, generating strain in the BBCP backbone. The added HPs are able to fill in gaps between the BBCPs caused by inhomogeneities in BBCP backbone length, alleviating this strain. Most importantly, adding HPs to the BBCP arrays allowed for photonic band gaps at wavelengths significantly longer than have been demonstrated previously (Figure 2.17). Unblended PS-PLA BBCPs have been shown to generate highly reflective films with λ_{max} up to ∼900 nm, generally with modest opacity in the visible range. Materials with λ_{max} 1300 nm were also obtained with these unblended materials, but the ordering was

poor, and thus the materials were broadly scattering in the visible portion of the spectrum. In this study, lamellar arrays that reflect light at ∼1410 nm were readily synthesized, with reduced opacity in the visible. These blended materials were well-ordered enough to observe second- and third-order harmonic reflectance peaks in some samples, indicating morphological fidelity previously unachievable for these large periodicities.

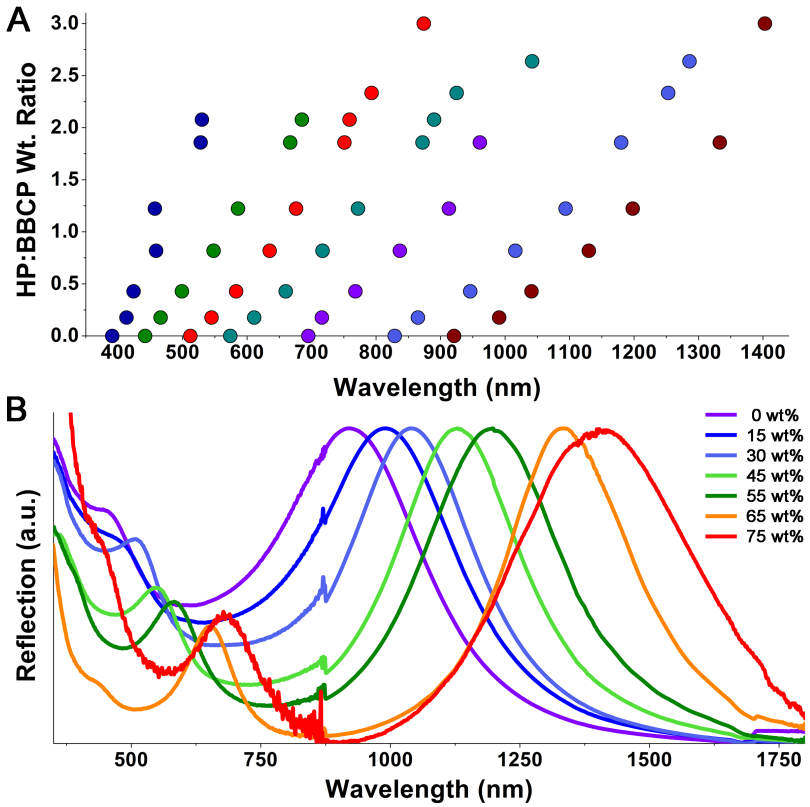

Figure 2.17: (a) BBCP/HP blends allow the photonic band gap of the self-assembled arrays to be easily tuned from 390 to 1410 nm. Each color corresponds to a specific BBCP; some BBCPs could be swollen to ∼180% of their initial domain spacing. (b) UV-vis spectra of the highest MW BBCP (brown circles in a) with increasing HP wt%. Samples were well-ordered enough to observe higher order resonances at λ/m (e.g., at ∼625 nm (m = 2) and ∼450 (m = 3) in the orange trace).

The addition of HPs to the BBCPs improves their overall ordering, thus improving the optical properties of the films. Additionally, this approach enables the incorporation of functional groups that might otherwise be difficult to attach to the BBCPs directly. In principle, a random copolymer (RCP) composed predominantly

of monomers identical to those in the BBCP macromonomers could serve as a useful vehicle to bring pendant functional groups into the arrays without the need to directly attach them to the BBCPs. Such functional groups could be used to increase the utility of these films by altering the refractive index of a given block (thereby increasing reflectivity),[48] providing a means to cross-link the films and increase their stability,[49] or allowing the films to be dynamically manipulated with the application of external stimuli.[44, 50] Through these studies, we have developed a polymeric platform to fabricate hybrid multilayer materials with tunable periodicities.

2.8 Applications

With an appreciation of the synthetic challenges, and a solid understanding of the polymer physics at play, we have been seeking to apply this materials platform to real world applications. The functional flexibility of our approach enables a host of new directions for functional, compliant and stimuli-responsive photonic elements. Additionally, the ability to synthetically and post-synthetically dial-in PCs with resonant reflection spanning from the UV to NIR enables a number of optical applications. Here, we outline a unique application of BBCPs to serve as a spectrally selective window paint, in order to improve the energy efficiency of building and vehicle envelopes.

Buildings are the nations largest consumers of energy and constitute roughly 40% of carbon dioxide emissions. Building envelope inefficiencies, largely attributed to windows, doors, and roofs, result in the loss of ∼30% of this energy. While windows lower energy demand for artificial lighting, provide view, and offer aesthetic value, they are thermally inefficient in winter compared to insulated walls and they allow solar radiation (both visible and NIR) to dramatically overheat the buildings in summer. Window inefficiencies cost the US over $40 billion annually in lost energy, highlighting the pressing need to address this energy waste epidemic. Replacing or upgrading inefficient windows with energy-efficient windows that are transparent to visible light but reflect NIR thermal radiation will dramatically reduce cooling loads in warm climates. While several existing solutions are commercially available, high

upfront costs are a major deterrent for many consumers and impede the rate of implementation. A low-cost retrofit option for inefficient windows is needed to rapidly address this waste.

Current solar control window technologies that prevent the transmission of NIR solar radiation most often consist of tinting or reflecting materials. Window tinting is unavoidably accompanied by broadband photon absorption, which can transfer heat through the window and also increase the need for artificial lighting. In terms of preventing the absorption of solar radiation, reflective coatings are a superior technology; an ideal coating selectively reflects NIR solar energy while allowing a desired amount of visible daylight to pass unobstructed.

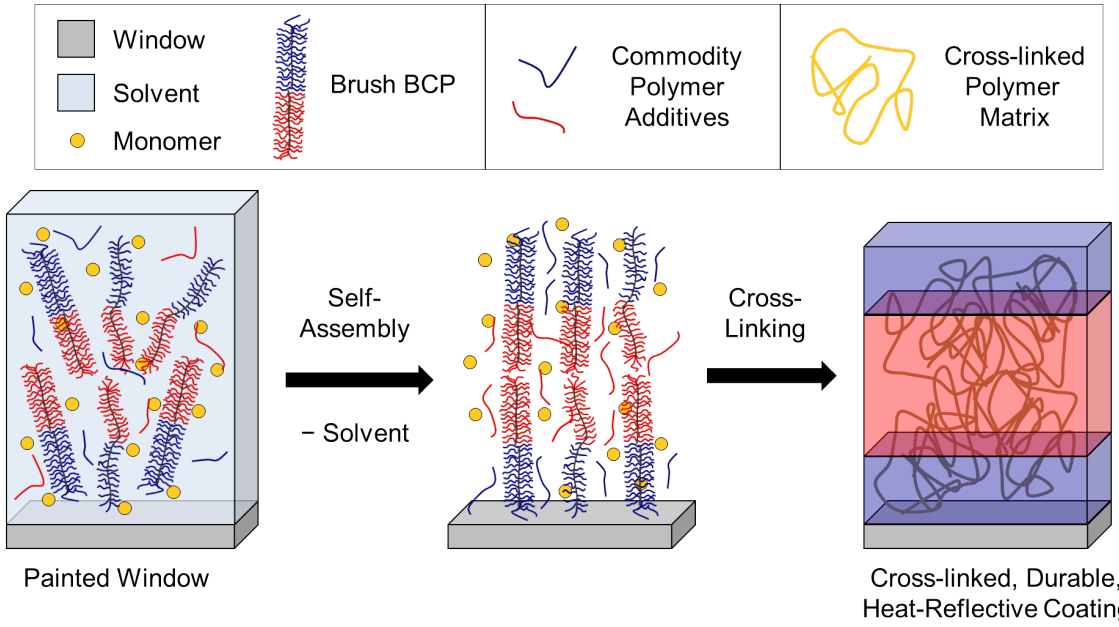

Figure 2.18: Our proposed paintable solar-control window film. Self-assembly results in a multilayer nanostructure the solvent dries, after the coating is applied. A reactive monomer provides a means to crosslink the film to provide a durable, IR-reflective coating.

Dielectric mirrors (1D PCs) are excellent coatings for transmitting visible light through a window while reflecting NIR radiation, which carries approximately half of the suns heat. The wavelength of reflection can be optimized by tuning the refractive index of the materials and periodicity of the layers. Dielectric mirrors are highly efficient at offsetting cooling costs for buildings in sunny climates and quickly achieve

payback. For residential buildings, the payback time is around 5 years and as low as 2-3 years for commercial buildings. Despite these attractive economic and environmental features, the currently fabricated reflective film technology presents some drawbacks. The current technology to fabricate polymeric dielectric mirror coatings consists of top-down approaches such as co-extrusion or layer-by-layer depositions of different dielectric materials with precision apparatus. These coatings must be fabricated off-site and then installed onto windows as a film. The high upfront costs for the films and their installation can deter people from the initial investment. Installation of a film is difficult: it requires a trained professional for proper installment and cannot be applied to curved surfaces. Furthermore, if the film is damaged, it must be replaced entirely, as repair is not possible. This concept of paintable coatings has great potential to improve current technologies by delivering a superior product at a fraction of the cost, motivating both commercial and residential consumers to engage in this energy- and cost-saving initiative.

We have revealed that the cost of these coatings can be drastically reduced through blending the molecular brush copolymers with commodity plastics, including linear polystyrene. These anisotropic advanced materials can contain as much as 75% by weight of commodity materials, using the brush block copolymer as a nanostructured template. Moreover, by incorporating linear polymer additives, the fidelity and performance of the films is increased, in part due to the stress relief granted during film formation by the additive. We propose to develop a commercially viable technology to retrofit inefficient windows with a spectrally selective, infrared-reflective polymeric coating through a simple, low-cost paint. Realization of this technology will present a disruptive solution for increasing building energy efficiency through thermal transport mitigation in windows.

The final goal of the project is a paint formulation and procedure to apply the infrared-reflective window coating that will be ready for scale-up. To verify that the performance and cost of our technology meet our targets as a superior product, we will demonstrate the feasibility through applying the coating to standard 30 x 60 inch residential windows to demonstrate cost-competitiveness, performance, and

durability. *En route* to this objective, our technical approach will consist of formulating a paint comprising brush block copolymers, linear polymer additives, polymerizable monomers, polymerization initiator, and environmentally benign solvent (Figure 2.18). Our efforts will build on optimizing our established technologies with brush block copolymers and linear polymers derived from commodity polystyrene and polyacrylic plastics to make high-performance films. Tailoring the polymer compositions will enable the film and polymerizable monomer to be deposited from benign alcohol solvents. During the drying process, the polymerization of the monomer will be initiated to produce a cross-linked, durable coating.

We believe that the quantitative technical performance can be comparable to other leading technologies, at a drastically lower installation cost. Specifically, the concept targets delivering a window coating that is transparent to visible light (85%) and rejects 97% of infrared radiation, while being installed at a fraction of the cost of current dielectric films. Additionally, we propose that our system could be engineered to independently tune the transmission of visible and NIR light, enabling precise anti-glare or tinting properties where desired.

References

(1) Hu, M.; Xia, Y.; McKenna, G. B.; Kornfield, J. A.; Grubbs, R. H. *Macromolecules* **2011**, *44*, 6935–6943.

(2) Hadjichristidis, N.; Pitsikalis, M.; Pispas, S.; Iatrou, H. *Chemical Reviews* **2001**, *101*, 3747–3792.

(3) Neiser, M. W.; Okuda, J.; Schmidt, M. *Macromolecules* **2003**, *36*, 5437–5439.

(4) Xia, Y.; Kornfield, J. A.; Grubbs, R. H. *Macromolecules* **2009**, *42*, 3761–3766.

(5) Xia, Y.; Olsen, B. D.; Kornfield, J. A.; Grubbs, R. H. *Journal of the American Chemical Society* **2009**, *131*, 18525–18532.

(6) Joannopoulos, J. D.; Johnson, S. G.; Winn, J. N.; Meade, R. D., *Photonic crystals: molding the flow of light*; Princeton university press: 2011.

(7) Lin, S. Y.; Fleming, J. G.; Hetherington, D. L.; Smith, B. K.; Biswas, R.; Ho, K. M.; Sigalas, M. M.; Zubrzycki, W.; Kurtz, S. R.; Bur, J. *Nature* **1998**, *394*, 251–253.

(8) Masuda, H.; Ohya, M.; Asoh, H.; Nakao, M.; Nohtomi, M.; Tamamura, T. *Japanese Journal of Applied Physics* **1999**, *38*, L1403.

(9) Campbell, M.; Sharp, D. N.; Harrison, M. T.; Denning, R. G.; Turberfield, A. J. *Nature* **2000**, *404*, 53–56.

(10) Jeon, S.; Park, J.-U.; Cirelli, R.; Yang, S.; Heitzman, C. E.; Braun, P. V.; Kenis, P. J. A.; Rogers, J. A. *Proceedings of the National Academy of Sciences of the United States of America* **2004**, *101*, 12428–12433.

(11) Braun, P. V.; Wiltzius, P. *Nature* **1999**, *402*, 603–604.

(12) Bertone, J. F.; Jiang, P.; Hwang, K. S.; Mittleman, D. M.; Colvin, V. L. *Physical Review Letters* **1999**, *83*, 300–303.

(13) Vayer, M.; Hillmyer, M. A.; Dirany, M.; Thevenin, G.; Erre, R.; Sinturel, C. *Thin Solid Films* **2010**, *518*, 3710–3715.

(14) Zalusky, A. S.; Olayo-Valles, R.; Wolf, J. H.; Hillmyer, M. A. *Journal of the American Chemical Society* **2002**, *124*, 12761–12773.

(15) Orfanidis, S. Electromagnetic waves and antennas., 2008.

(16) Gu, W.; Huh, J.; Hong, S. W.; Sveinbjornsson, B. R.; Park, C.; Grubbs, R. H.; Russell, T. P. *ACS Nano* **2013**, *7*, 2551–2558.

(17) Troparevsky, M. C.; Sabau, A. S.; Lupini, A. R.; Zhang, Z. *Optics Express* **2010**, *18*, 24715–24721.

(18) Sveinbjörnsson, B. R.; Weitekamp, R. A.; Miyake, G. M.; Xia, Y.; Atwater, H. A.; Grubbs, R. H. *Proceedings of the National Academy of Sciences* **2012**, *109*, 14332–14336.

(19) Yashima, E.; Maeda, K.; Iida, H.; Furusho, Y.; Nagai, K. *Chemical reviews* **2009**, *109*, 6102–6211.

(20) Green, M. M.; Park, W.; Sato, T.; Teramoto, A.; Lifson, S.; Selinger, R. L.; Selinger, J. V. *Angewandte Chemie International Edition* **1999**, *38*, 3138–3154.

(21) Mayer, S.; Zentel, R. *Progress in polymer science* **2001**, *26*, 1973–2013.

(22) Kikuchi, M.; Lien, L. T. N.; Narumi, A.; Jinbo, Y.; Izumi, Y.; Nagai, K.; Kawaguchi, S. *Macromolecules* **2008**, *41*, 6564–6572.

(23) Patten, T. E.; Novak, B. M. *Journal of the American Chemical Society* **1996**, *118*, 1906–1916.

(24) Patten, T. E.; Novak, B. M. *Journal of the American Chemical Society* **1991**, *113*, 5065–5066.

(25) Albert, J. N.; Epps, T. H. *Materials Today* **2010**, *13*, 24–33.

(26) Matsen, M. W.; Bates, F. S. *Journal of Polymer Science Part B: Polymer Physics* **1997**, *35*, 945–952.

(27) Yamaguchi, D.; Hashimoto, T. *Macromolecules* **2001**, *34*, 6495–6505.

(28) Kane, L.; Satkowski, M. M.; Smith, S. D.; Spontak, R. J. *Macromolecules* **1996**, *29*, 8862–8870.

(29) Hashimoto, T.; Yamasaki, K.; Koizumi, S.; Hasegawa, H. *Macromolecules* **1993**, *26*, 2895–2904.

(30) Parnell, A. J.; Pryke, A.; Mykhaylyk, O. O.; Howse, J. R.; Adawi, A. M.; Terrill, N. J.; Fairclough, J. P. A. *Soft Matter* **2011**, *7*, 3721–3725.

(31) Darling, S. B. *Progress in Polymer Science* **2007**, *32*, 1152–1204.

(32) Lynd, N. A.; Meuler, A. J.; Hillmyer, M. A. *Progress in Polymer Science* **2008**, *33*, 875–893.

(33) Lynd, N. A.; Hillmyer, M. A. *Macromolecules* **2005**, *38*, 8803–8810.

(34) Widin, J. M.; Kim, M.; Schmitt, A. K.; Han, E.; Gopalan, P.; Mahanthappa, M. K. *Macromolecules* **2013**, *46*, 4472–4480.

(35) Schlüter, A. D.; Rabe, J. P. *Angewandte Chemie International Edition* **2000**, *39*, 864–883.

(36) Zhang, A.; Shu, L.; Bo, Z.; Schluter, A. D. *Macromolecular Chemistry and Physics* **2003**, *204*, 328–339.

(37) Rajaram, S.; Choi, T.-L.; Rolandi, M.; Fréchet, J. M. *Journal of the American Chemical Society* **2007**, *129*, 9619–9621.

(38) Chen, Y.; Xiong, X. *Chemical Communications* **2010**, *46*, 5049–5060.

(39) Piunova, V. A.; Miyake, G. M.; Daeffler, C. S.; Weitekamp, R. A.; Grubbs, R. H. *Journal of the American Chemical Society* **2013**, DOI: 10.1021/ja4081502.

(40) Fredrickson, G. H.; Bates, F. S. *Annual Review of Materials Science* **1996**, *26*, 501–550.

(41) Rastogi, S.; Spoelstra, A. B.; Goossens, J. G. P.; Lemstra, P. J. *Macromolecules* **1997**, *30*, 7880–7889.

(42) Urbas, A.; Sharp, R.; Fink, Y.; Thomas, E. L.; Xenidou, M.; Fetters, L. J. *Advanced Materials* **2000**, *12*, 812–814.

(43) Valkama, S.; Kosonen, H.; Ruokolainen, J.; Haatainen, T.; Torkkeli, M.; Serimaa, R.; Brinke, G. ten; Ikkala, O. *Nature Materials* **2004**, *3*, 872–876.

(44) Kang, Y.; Walish, J. J.; Gorishnyy, T.; Thomas, E. L. *Nature materials* **2007**, *6*, 957–960.

(45) Winey, K. I.; Thomas, E. L.; Fetters, L. J. *Macromolecules* **1991**, *24*, 6182–6188.

(46) Shull, K. R.; Winey, K. I. *Macromolecules* **1992**, *25*, 2637–2644.

(47) Macfarlane, R. J.; Kim, B.; Lee, B.; Weitekamp, R. A.; Bates, C. M.; Lee, S. F.; Chang, A. B.; Delaney, K. T.; Fredrickson, G. H.; Atwater, H. A.; Grubbs, R. H. *Journal of the American Chemical Society* **2014**, *136*, 17374–17377.

(48) Su, H.-W.; Chen, W.-C. *Journal of Materials Chemistry* **2008**, *18*, 1139–1145.

(49) Bang, J.; Bae, J.; Löwenhielm, P.; Spiessberger, C.; Given-Beck, S. A.; Russell, T. P.; Hawker, C. J. *Advanced Materials* **2007**, *19*, 4552–4557.

(50) Yoon, J.; Lee, W.; Thomas, E. L. *Macromolecules* **2008**, *41*, 4582–4584.

Chapter 3

Resonant Dielectric Structures for Improved Photovoltaics

Portions adapted with permission from Grandidier, J.; Weitekamp, R. A.; Deceglie, M. G.; Callahan, D. M.; Battaglia, C.; Bukowsky, C. R.; Ballif, C.; Grubbs, R. H.; Atwater, H. A. "Solar Cell Efficiency Enhancement via Light Trapping in Printable Resonant Dielectric Nanosphere Arrays". *Physica Status Solidi (a)* **2012**.

Chapter Abstract

Resonant dielectric structures are a promising platform for addressing the key challenge of light trapping in thin-film solar cells. We theoretically and experimentally demonstrate enhanced efficiencies in photovoltaic cells via resonant dielectric nanosphere arrays. Two distinct amorphous silicon photovoltaic architectures were improved using this versatile light-trapping platform. In one structure, the colloidal monolayer couples light into the absorber in the near-field acting as a photonic crystal (PC) light-trapping element. In the other, it acts in the far-field as a graded index antireflection coating to further improve a cell which already included a state-of-the-art random light-trapping texture to achieve a conversion efficiency over 11%. For the near-field flat cell architecture, we directly fabricated the colloidal monolayer on the device through Langmuir-Blodgett deposition in a scalable process that does not degrade the active material. In addition, we present a novel transfer printing method, which utilizes chemical crosslinking of an optically thin adhesion layer to tether sphere arrays to the device surface. The minimally invasive processing conditions of this transfer method enable the application to a wide range of solar cells and other optoelectronic devices.

3.1 Introduction

Thin-film photovoltaic (PV) cells have a number of key advantages over wafer-based devices, including reduced active material usage, weight, and cost [1]. However, the corresponding loss in optical absorption often limits cell efficiency, mitigating the advantages of thin-film absorber cells. Dielectric texturing [2] and optimized antireflection coatings [3] are commonly employed in silicon (Si) wafer-based PVs to increase light absorption. A textured active material increases light trapping; however, the large-scale features that are commonly employed for crystalline Si solar cells cannot be employed for thin-film cells, which often have total thicknesses of the order of the optical wavelength. As well, physical modification of the absorber layer by patterning or etching can result in degraded material quality and thus reduced carrier collection efficiency [4]. It is therefore desirable to develop a light-trapping strategy for thin-film cells that does not in any way compromise the electronic performance of the absorber, junction, and passivation layers. Plasmonic structures [5–7], gratings [8], photonic crystals (PC) [9], Mie resonators [10, 11], and dielectric diffractive structures [12] have all been recently investigated as light-trapping elements. In this context, colloidal arrays of resonant dielectric spheres represent an attractive approach because they are low loss and do not impact the electronic performance of the device.

When arrays of nanospheres are placed at wavelength-scale distances from a thin-film cell, the resonant modes in the spheres leak into the semiconductor layer, increasing absorption. Our group previously reported simulations which predict that a nanosphere array on top of a thin-film hydrogenated amorphous silicon (a-Si:H) or gallium arsenide solar cell can significantly increase both light absorption in the active layer [13, 14] and device efficiency [15]. Here, we report experimental results that are in good agreement with the predictions from full field finite-difference time-domain (FDTD) optical simulations, and device physics simulations. Angle-resolved external quantum efficiency (EQE) measurements were performed and compared to rigorous coupled wave analysis (RCWA). Our experimental results support the light-trapping mechanism suggested by simulation.

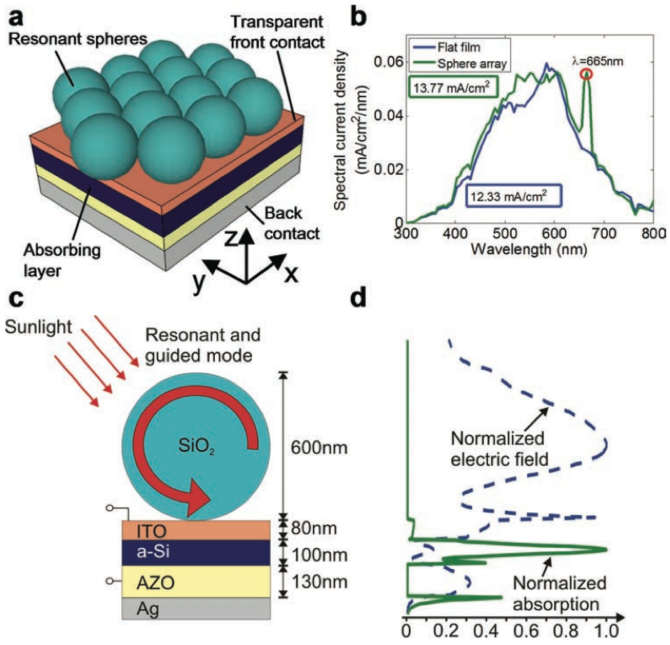

Figure 3.1: (a) A 2D colloidal crystal on a-Si solar cell. (b) The simulated absorption of the cell with and without the sphere array. The sharp resonance is due to coupling to the resonant modes of the colloidal array. (c) A vertical cross section of the cell. (d) The normalized electric field and absorption profile as a function of depth into the structure. [13]

3.2 Fabrication

3.2.1 Solar Cell Fabrication

Amorphous silicon solar cells with an intrinsic absorber layer thickness of 250 nm were deposited in *p-i-n* sequence by plasma-enhanced chemical vapor deposition in an industrial KAI reactor with parallel plate configuration. More details can be found in Reference [16]. The flat cell was deposited on an 80-nm thick sputtered aluminum back reflector covered by 70 nm of sputtered zinc oxide (ZnO). A 70-nm thick sputtered indium tin oxide (ITO) was used as transparent front electrode and efficient antireflection coating. The cells were patterned to 5 x 5 mm^2 by lift-off and SF_6 reactive ion etching.

3.2.2 2D Colloidal Crystal Fabrication

Experimentally, one of the main challenges to realizing resonant nanosphere enhanced solar cells is in fabricating a large-area, high-fidelity monolayer of closely packed spheres. Diffractive coupling occurs when the spheres are periodically arranged as a 2D colloidal crystal [17]. Hexagonally packed spheres of relatively uniform diameter offer an optimal geometry to enhance the efficiency in the cell via PC resonances. Many methods of colloidal crystal assembly can be found in the literature, including controlled evaporation [18], sedimentation [19], and spin coating. Compared to many other attempted techniques, we found Langmuir-Blodgett (LB) deposition [20] to yield the highest quality 2D colloidal crystals of silica spheres with diameters near visible wavelengths and to have the highest long-range order and lowest number of multilayer and gap defects. The trough we used is intended for samples of a few cm^2, but this technique has been extended to full wafers [21] and could potentially be scaled to PV module dimensions. We used uniform silica spheres with a nominal diameter of 700 nm. Our simulations indicated that this diameter would result in the highest photocurrent enhancement for a thin-film a-Si:H solar cell [22]. Other potential materials for the spheres, such as polystyrene or TiO_2 are discussed in Reference [22]. The silica nanospheres were functionalized with aminopropyl(diethoxy)methyl silane, and deposited from a dilute suspension in 1:4 ethanol:dichloromethane, compressed on an acidic aqueous sub-phase. We found that the long-range order of the colloidal crystals was highly dependent on the pH of the sub-phase. We attribute this result to the electrostatic repulsion of the protonated RNH_3^+ ions on the functionalized sphere surface, which mitigate sphere-sphere attraction in the suspension. Reduced aggregation would account for the improved long-range order and reduced multilayer formation. For this study, we used a solution of pH ≈ 2.5, corresponding to two drops of concentrated hydrochloric acid in 250 mL deionized water. The detailed deposition procedure can be found in Section 8.

Figure 3.2(a) depicts the LB process used to deposit a uniform monolayer array of silica nanospheres atop the thin-film a-Si:H solar cell. Scanning electron microscopy

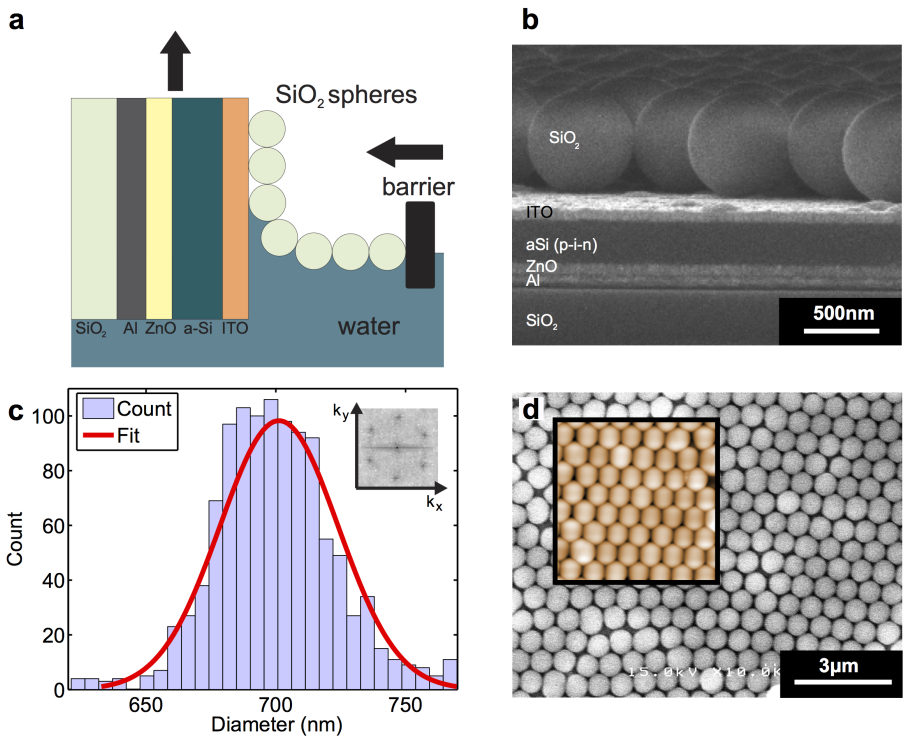

Figure 3.2: A silica colloidal monolayer on a solar cell. (a) Schematic of the sphere deposition on the solar cell using the Langmuir-Blodgett method. (b) SEM cross-section of the solar cell with resonant spheres on top. (c) Size distribution histogram of the spheres and the corresponding Gaussian fit. The inset displays a Fourier transform of an SEM image of the spheres. (d) SEM image with a corresponding atomic force micrograph as an inset (on the same scale).

(SEM) as well as atomic force microscopy (AFM) images of the nanosphere array are shown in Figure 3.2(b) and (d). The influence of the separation between the sphere array and the active layer is discussed in Reference [15]. The Fourier transform of a large-area SEM image of the nanosphere array yields an average periodicity of $\lambda = 700$ nm. Because the spheres are closely packed, we assume that the average periodicity is equal to the average diameter of the spheres. From the direct space of an SEM image, we are able to estimate the sphere size distribution on a sample of about 1000 spheres using image analysis software (imageJ). We assume a Gaussian distribution for the sphere size, which fits the counted distribution relatively well (Figure 3.2(c)).

3.3 Simulation & Measurement

3.3.1 Illumination at Normal Incidence

We measured the EQE of cells coated with dielectric nanospheres and repeated this measurement after removing the spheres from the surface (Figure 3.3(a)) using a Q-tip and methanol. We do not expect this gentle removal process to affect the optical or electrical properties of the solar cell. The coated cells showed broadband enhancement over the measured spectrum. Weighting the EQE by the AM1.5G solar spectrum gives, for the flat cell, a short circuit current density of 8.8 mA/cm^2, and for the cell coated with spheres 9.6 mA/cm^2, corresponding to a relative enhancement of 9.1%. Using an AM1.5G solar simulator, we performed white light current voltage measurements on five similar solar cells coated with spheres and with the spheres subsequently removed. The average relative enhancement for the efficiency is 7.0 $\pm$ 1.8%, and 8.5 $\pm$ 1.5% for the short circuit current (J_{sc}), in good agreement with the measured EQE weighted by the AM1.5G solar spectrum. Figure 3.3(b) plots the current-voltage measurement for the solar cell demonstrating the highest efficiency enhancement, which is almost 10% from 4.39 to 4.81%. We were able to reproduce these current-voltage curves with full 3D finite element device physics simulations [15, 23], taking the generation rate as calculated via FDTD as input.

In order to analyze each of the features in the measured EQE, we first plot the result of the simulation for spheres of the median diameter, 700nm, in Figure 3.4(b). We verified experimentally and theoretically [15] that the EQE is independent of the polarization at normal incidence. Several sharp and distinct peaks are observed in this simulation.

For three points on this plot, we plot the electric field intensity for a cross section at the middle of a sphere in the same plane as the polarization of the normal incident plane wave in Figures 3.4(c-e). It can be seen that numerous resonant modes exist within the experimental size distribution of the spheres, covering a broad range of wavelengths. To explain the entire experimental spectra, we must consider multiple optical coupling mechanisms that are possible with these wavelength-scale resonant

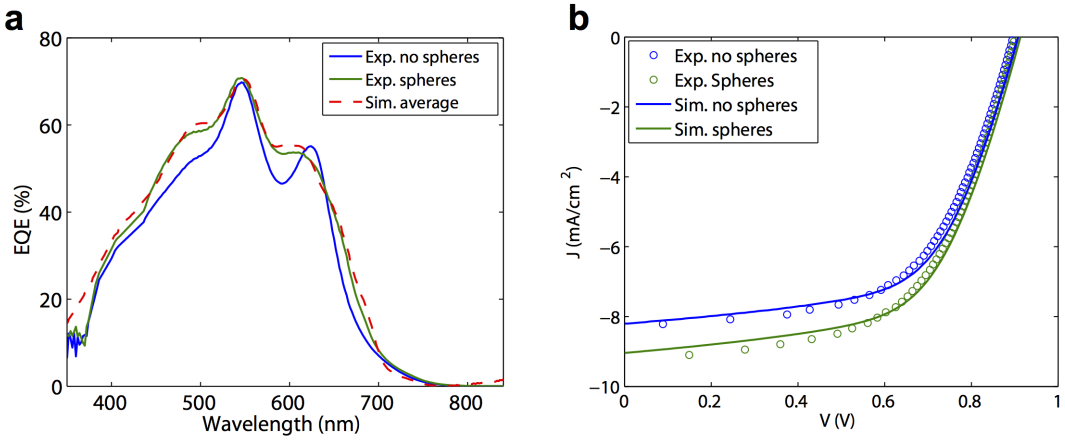

Figure 3.3: Photovoltaic performance at normal incidence. (a) EQE measurement of the flat solar cell with and without dielectric spheres on top. The red dashed line corresponds to optical simulations of a solar cell with spheres on top weighted by the average size distribution. (b) Corresponding current-voltage curve measured with an AM1.5G solar simulator and corresponding device physics simulation.

structures, depending on the region of the spectrum we consider. For wavelengths between approximately 350 nm and 550 nm, we observe EQE enhancement that is relatively independent of the size distribution of the spheres. We attribute this enhancement mainly to the Fabry-Perot resonance formed by the array of spheres as similar features are observed in a homogeneous slab with the volume-weighted refractive index of the spheres in air. We attribute the enhancement in the spectral range between 550 nm and 750 nm to coupling to in-plane leaky modes of the 2D PC bandstructure, greatly broadened due to the experimental size distribution of the spheres. To explain this enhancement, we simulate 21 cases for sphere diameters varying between 650 nm and 750 nm using the observed size distribution range shown in Figure 3.2(c). Each simulation assumes an infinite array of spheres with periodic boundary conditions. In order to account for the measured distribution of the sphere size, we weight the set of simulations by the Gaussian distribution represented in Figure 3.2(c). The resonant features of the experimental spectrum and the weighted average spectrum are very well matched (Figure 3.3(a)). From this analysis, we conclude that the features in the experimental EQE spectra from 550 nm to 750 nm are associated with the excitation of resonant modes of the colloidal monolayer [13] and thus that

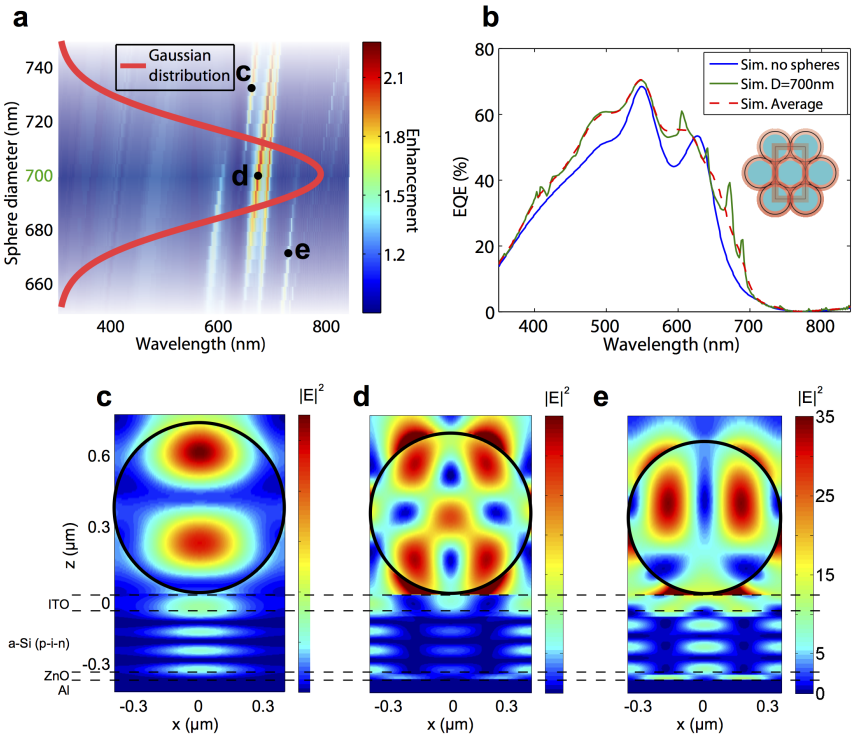

Figure 3.4: FDTD simulations of a resonant dielectric structure on a solar cell. (a) Map of the enhancement of the EQE of an a-Si:H solar cell with spheres over the EQE of the cell without spheres as a function of the wavelength for the different sphere diameters across the measured size distribution, and the Gaussian fit used to weight the individual simulations (in arbitrary units, taken from Figure 3.2(c)). (b) Optically simulated EQE for the PV structure with and without dielectric spheres on top. (c-e) For each labeled peak on (a): the electric field intensity in V^2m^{-2} for a cross section at the middle of a sphere.

the observed enhancement in this spectral range is due to leaky PC modes. Prior literature also attributes these resonant features to both PC modes and Mie resonances [24] or whispering gallery modes [13]. This result demonstrates that the excitation of modes within a low loss dielectric resonant structure can have a significant impact on the EQE enhancement of a solar cell. Reflection measurements of a 2D colloidal crystal on a Si wafer support the proposed mechanism of enhancement (Figure 3.5).

3.3.2 Angle-dependent Performance

We then measured the angle dependence of the EQE in both TE and TM polarizations and plot in Figure 3.6(a) the average relative EQE enhancement for angles varying

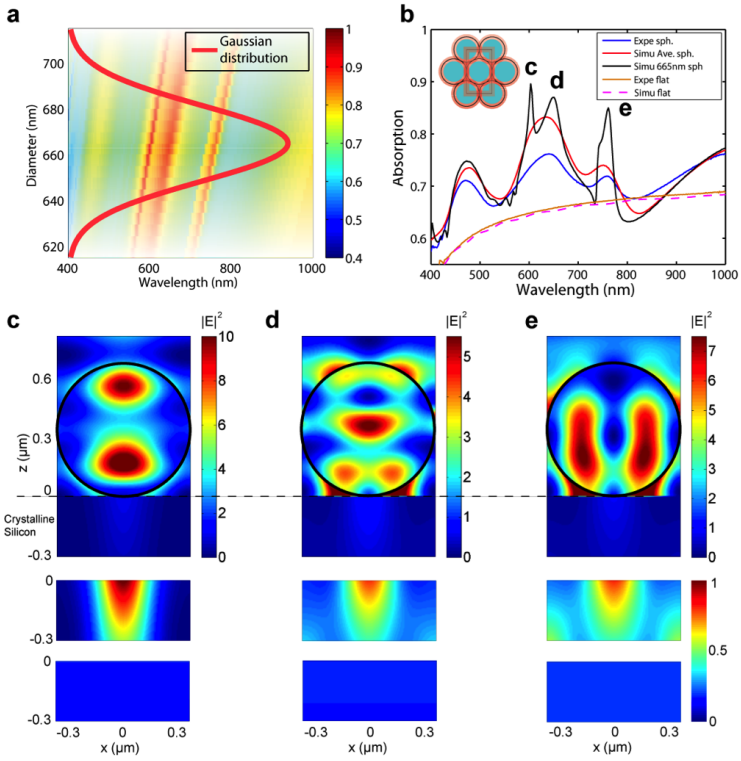

Figure 3.5: Simulated vs. measured absorption of a resonant dielectric structure on flat Si. (a) Map of the absorption as a function of the wavelength for the different sphere diameters across the measured size distribution. The Gaussian distribution of sphere diameters, used to weight each individual simulations, is plotted on top, with arbitrary amplitude. (b) Simulated and measured absorption for the photovoltaic structure with dielectric spheres on top of it. (c,d,e) For each labeled peak on b: electric field intensity for a cross section at the middle of a sphere. Below on a different color scale is the electric field intensity for a cross section within the first 300 nm of absorbing layer and below that, the equivalent case without spheres.

between 0°and 70°. The observed EQE enhancement bands account for the variation of the structure's resonances as a function of the angle of incidence. In order to evaluate the performance of the photovoltaic structure, we interpolated angle-resolved data [25] of the incident solar energy on a sunny day to match the resolution of our EQE measurements corresponding to Figure 3.6(a). Figure 3.6(b) shows the equivalent simulated plot using RCWA for 700 nm diameter spheres. We then compare the angle-dependent photocurrent generated by a flat cell and a cell with spheres (Figure 3.6(c)) and calculate the relative short circuit current enhancement due to the colloidal crystal (Figure 3.6(d)). It varies between 5.0% (at 55°) and 8.9% (at

0°) with an average of 6.3% through the day. The strongest enhancement is observed at normal incidence. The relatively angle-independent enhancement is a promising result; it demonstrates that these resonant dielectric structures can couple direct and scattered sunlight throughout the day.

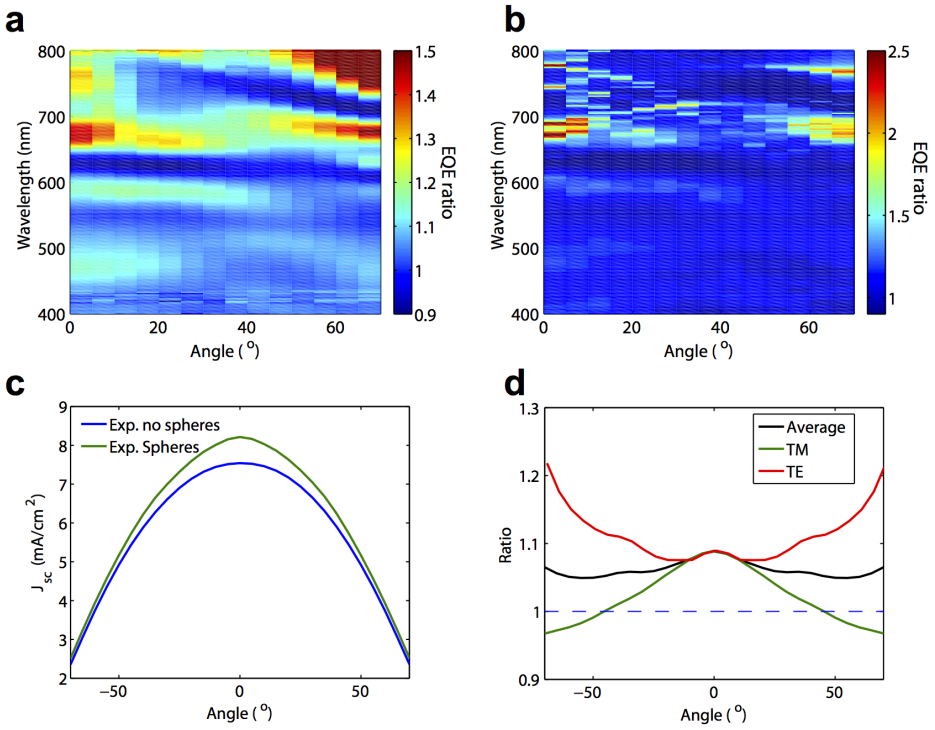

Figure 3.6: (a) Angle resolved measurement of the EQE enhancement, averaged over TE and TM polarizations. Calculated from the ratio of the sphere coated EQE to the flat cell EQE. (b) Corresponding simulation using RCWA for the median size sphere diameter (700 nm). (c) J_{sc} generated by the active material for the case with and without spheres. TE and TM polarization were averaged to account for the unpolarized nature of solar radiation. Tabulated data of solar irradiance was used to weight the measured absorption [25]. (d) Relative enhancement over the flat solar cell as a function of the incident angle for TE, TM and averaged polarizations.

3.3.3 Anti-Reflective Coating of a High Performance Cell

Finally, we demonstrate performance enhancement from a sphere array on an a-Si:H solar cell with a state-of-the-art architecture [26] and a high initial efficiency of 10.9%. This solar cell consists of a rough ZnO/a-Si:H/ZnO structure deposited on

glass (Figure 3.7(a)). It was deposited on a 2 μm thick transparent ZnO front electrode grown by low-pressure chemical vapor deposition featuring the characteristic naturally textured pyramidal surface morphology [26]. The ZnO surface was treated with argon plasma to optimize the morphology for cell deposition. A 2.5 μm thick transparent ZnO layer was used as a back electrode in combination with a white diffuse dielectric back reflector. The sensitivity of the ZnO towards the acidic aqueous environment from which we draw the spheres prevented the direct organization of the colloidal crystal on the cell surface. To overcome this issue, we developed a transfer printing technique based on the work of Yang [27] (Figure 3.7(a)). The colloidal crystals were fabricated as previously described, on a glass slide. For each cell, a poly(dimethylsiloxane) (PDMS) stamp was pressed into the colloidal array, peeled away, and then pressed onto the device surface, which was first spin-coated with 15-20 nm of poly(vinyl alcohol) (PVA) from an aqueous solution containing 5% gluteraldehyde. The cells were heated to 100 °C under argon for 2 hours to crosslink the polymer around (and to) the sphere base. Despite the fact that the nominal PVA thickness is only 2-3% of the sphere diameter, the colloidal crystals were effectively transferred to the device surface with high fidelity and good yield. We attribute this robust adhesion to the fact that gluteraldehyde can couple to both the hydroxyl groups of the polymer as well as the amines on the sphere surface, enabling both polymer/polymer and polymer/sphere crosslinking (Figure 3.7(a)). Generally, it is crucial that the PVA spacer remain optically thin, as an adjacent material can perturb the resonant modes and parasitically confine light. The performance of the solar cell with and without the sphere array is plotted in Figures 3.7(c) & 3.7(d). A relative enhancement of 1.8% is seen for the highest efficiency, which reaches 11.1%. Enhancement in EQE occurs around 450 nm and 650 nm, resulting in a short circuit current increase of 1.8% from 15.9 mA/cm^2 to 16.2 mA/cm^2. Fill factor and open circuit voltage remain the same at about 75% and 910 mV, respectively. Due to its structural complexity, we did not simulate the full cell architecture. While PC mode resonances are not directly observed for this cell architecture, the 2D colloidal crystal nevertheless proves an effective antireflection coating. We attribute the enhancement here to the

graded index provided by the sphere geometry [28], which is supported by transfer matrix simulations (Figure 8.1). These results contrast with the flat cell, where the spectral features associated with near-field coupling between the PC modes and the active layer could not be accounted for by this simple graded index model. While the resonant features are not observed in the EQE spectrum of the absorber layer with the colloidal crystal in the far field, this example demonstrates that our approach can be combined with other state-of-the-art light-trapping techniques, specifically active layer texturing.

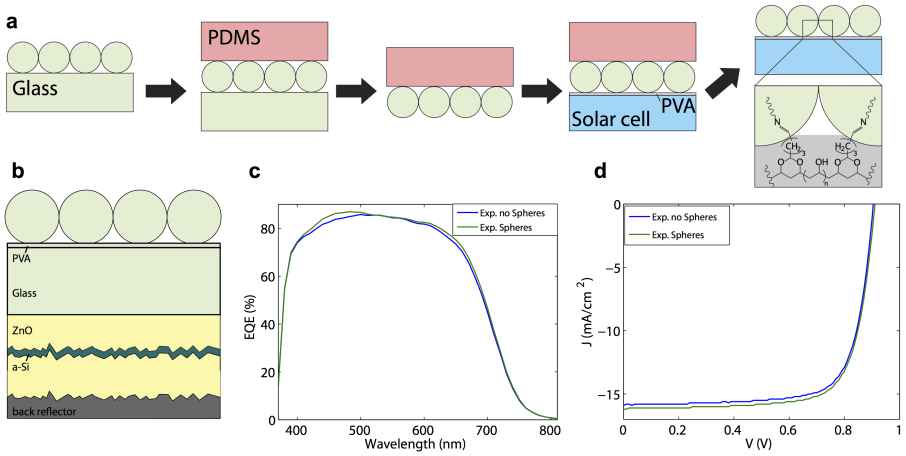

Figure 3.7: (a) Fabrication steps of the transfer printing technique used to coat the solar cell with nanospheres. A PDMS stamp is pressed into the 2D colloidal crystal formed on a glass slide by Langmuir-Blodgett deposition. The PDMS stamp is then peeled away to ink the stamp with spheres. PDMS and spheres are pressed onto the solar cell coated with 15nm PVA and heated for 2 hours at 100 °C to crosslink PVA. Finally the PDMS stamp is peeled away to leave a printed colloidal crystal embedded in the cross-linked PVA film. The inset depicts possible bonding arrangements between the aminated sphere array and glutaraldehyde crosslinked PVA network. (b) 2D cross section of the rough a-Si:H solar cell. (c) Measured EQE and (d) current-voltage with and without spheres.

3.4 Conclusion

We have experimentally enhanced the efficiency of thin-film a-Si:H solar cells using PC modes of resonant dielectric structures. This type of light trapping could enable one to reduce the thickness of the active layer, resulting in electrical improvement and

cost reduction. When the resonant structure is near the active absorbing layer, the proposed mechanism of coupling through PC resonances is verified by measurements of silica nanosphere arrays on a flat a-Si:H solar cell. Due to the fabricated geometry of our resonant dielectric structures, the relative enhancement of absorption is largely insensitive to the incident angle of the sunlight. This is important for many photovoltaic applications, such as residential installations, where tracking is cost prohibitive and diffuse light accounts for a significant fraction of the available solar energy. This type of modification can be employed after device fabrication, and combined with other light trapping schemes to further enhance photovoltaic performance. We are also considering higher index materials like TiO_2 spheres. Such high-index material can be embedded in poly(ethylene-vinyl acetate) (EVA) [22], which is commonly used for solar cell encapsulation. We have developed a method that enables the transfer of high fidelity colloidal crystals to device surfaces, using an optically thin and chemically robust adhesion layer. Finally, we have demonstrated that 2D colloidal crystals can also improve the efficiency of ultra-high efficiency amorphous silicon solar cells, which already incorporate random texturing as a light-trapping element. Our methods are relevant to improving a variety of other devices, including photodetectors, LEDs, photoelectrochemical cells, bioreactors, and sensors. Resonant dielectric structures offer a versatile light-trapping solution, which is simple to implement and has significant potential to improve solar energy conversion.

References

(1) Shah, A. V.; Schade, H.; Vanecek, M.; Meier, J.; Vallat-Sauvain, E.; Wyrsch, N.; Kroll, U.; Droz, C.; Bailat, J. *Progress in photovoltaics: Research and applications* **2004**, *12*, 113–142.

(2) Yablonovitch, E.; Cody, G. D. *Electron Devices, IEEE Transactions on* **1982**, *29*, 300–305.

(3) Zhao, J.; Green, M. A. *Electron Devices, IEEE Transactions on* **1991**, *38*, 1925–1934.

(4) Hsu, C.-M.; Battaglia, C.; Pahud, C.; Ruan, Z.; Haug, F.-J.; Fan, S.; Ballif, C.; Cui, Y. *Advanced Energy Materials* **2012**, *2*, 628–633.

(5) Atwater, H. A.; Polman, A. *Nature materials* **2010**, *9*, 205–213.

(6) Catchpole, K. R.; Polman, A. *Optics express* **2008**, *16*, 21793–21800.

(7) Li, X.; Hylton, N. P.; Giannini, V.; Lee, K.-H.; Ekins-Daukes, N. J.; Maier, S. A. *Optics express* **2011**, *19*, A888–A896.

(8) Pala, R. A.; White, J.; Barnard, E.; Liu, J.; Brongersma, M. L. *Advanced Materials* **2009**, *21*, 3504–3509.

(9) Bermel, P.; Luo, C.; Zeng, L.; Kimerling, L. C.; Joannopoulos, J. D. *Optics express* **2007**, *15*, 16986–17000.

(10) Mann, S. A.; Grote, R. R.; Osgood, R. M.; Schuller, J. A. *Optics express* **2011**, *19*, 25729–25740.

(11) Spinelli, P.; Verschuuren, M. A.; Polman, A. *Nature communications* **2012**, *3*, 692.

(12) Kroll, M.; Fahr, S.; Helgert, C.; Rockstuhl, C.; Lederer, F.; Pertsch, T. *physica status solidi (a)* **2008**, *205*, 2777–2795.

(13) Grandidier, J.; Callahan, D. M.; Munday, J. N.; Atwater, H. A. *Advanced Materials* **2011**, *23*, 1272–1276.

(14) Grandidier, J.; Callahan, D. M.; Munday, J. N.; Atwater, H. A. *Photovoltaics, IEEE Journal of* **2012**, *2*, 123–128.

(15) Grandidier, J.; Deceglie, M. G.; Callahan, D. M.; Atwater, H. A. *Journal of Photonics for Energy* **2012**, *2*, 024502–1.

(16) Battaglia, C.; Hsu, C.-M.; Söderström, K.; Escarre, J.; Haug, F.-J.; Charrière, M.; Boccard, M.; Despeisse, M.; Alexander, D. T.; Cantoni, M., et al. *ACS nano* **2012**, *6*, 2790–2797.

(17) Cole, R. M.; Sugawara, Y.; Baumberg, J. J.; Mahajan, S.; Abdelsalam, M.; Bartlett, P. N. *Physical review letters* **2006**, *97*, 137401.

(18) Mihi, A.; Zhang, C.; Braun, P. V. *Angewandte Chemie* **2011**, *123*, 5830–5833.

(19) Jiang, P.; Bertone, J. F.; Hwang, K. S.; Colvin, V. L. *Chemistry of Materials* **1999**, *11*, 2132–2140.

(20) Hsu, C.-M.; Connor, S. T.; Tang, M. X.; Cui, Y. *Applied Physics Letters* **2008**, *93*, 133109.

(21) Zhu, J.; Yu, Z.; Fan, S.; Cui, Y. *Materials Science and Engineering: R: Reports* **2010**, *70*, 330–340.

(22) Grandidier, J.; Callahan, D. M.; Atwater, H. A. In *Photovoltaic Specialists Conference (PVSC), 2012 38th IEEE*, IEEE: 2012, pp 003325–003327.

(23) Deceglie, M. G.; Ferry, V. E.; Alivisatos, A. P.; Atwater, H. A. *Nano letters* **2012**, *12*, 2894–2900.

(24) López-García, M.; Galisteo-López, J. F.; López, C.; García-Martín, A. *Physical Review B* **2012**, *85*, 235145.

(25) Marion, W. F.; Kroposki, B.; Emery, K.; Del Cueto, J.; Myers, D.; Osterwald, C., *Validation of photovoltaic module energy ratings procedure at NREL*; National Renewable Energy Laboratory: 1999.

(26) Battaglia, C.; Escarré, J.; Söderström, K.; Charrière, M.; Despeisse, M.; Haug, F.-J.; Ballif, C. *Nature Photonics* **2011**, *5*, 535–538.

(27) Yan, X.; Yao, J.; Lu, G.; Chen, X.; Zhang, K.; Yang, B. *Journal of the American Chemical Society* **2004**, *126*, 10510–10511.

(28) Fang, C.-Y.; Liu, L.; Lee, Y.-C.; Chen, H.-L.; Wan, H.; Yu, C.-C. *Advanced Functional Materials* **2013**, *23*, 1412–1421.

Part II

Functional Lithography

Chapter 4

Top-down Fabrication

Chapter Abstract

"Top-down" lithographic methods for precisely patterning materials represent a complimentary approach to self-assembly. In this introductory chapter, we first briefly outline different classes of lithography. Some of the well-adopted chemical mechanisms behind photolithography will be discussed, particularly in the context of ultraviolet-activated thin-films. This chemistry is crucial to modern microfabrication techniques —it is in many ways the physical embodiment of Moore's Law. We outline some of the limitations of the existing photopatterning methodologies, primarily with respect to the diversity of materials that can be employed. Finally, we introduce the concept of functional lithography, a guiding principle for the work in this thesis.

4.1 Introduction

Lithography is the science of patterning, the chemistry of image formation. Generally speaking, xerography, inkjet-, laser- and screen-printing are all everyday embodiments of lithography. In modern micro- and nanofabrication, photons and electrons are utilized to activate localized chemistry to precisely define and differentiate various device domains. Within the field of photolithography, there are a wide variety of implementations which harness photons from the infrared to soft x-ray regions of the electromagnetic spectrum. In this introductory chapter, we will primarily focus on ultraviolet-activated photochemistry, as it represents the most widespread manifestation of photolithography.

There are a number of methods by which the optical flux can be patterned to generate the desired image. Rastering a focused beam, projection through a mask and diffraction via a grating are some of the most commonly employed. In integrated circuit fabrication, the pattern defined by the photomask (or reticle) is concentrated and tessellated across the wafer surface. Figure 4.1 outlines the optical setup of a so-called "stepper" lithography tool.

One method of improving the throughput of lithographically defined features is through imprint lithography. In many ways, this is simply stamping a pattern into a material. In this process, a master stamp can be defined lithographically, and reproduced via molding techniques to create a number of "daughter" stamps. These stamps can be used to replicate the desired features multiple times before new daughter stamps must be made due to deterioration. Nanoimprint lithography represents a currently deployed embodiment of this technology, which utilizes electron-beam lithography to create stamps with nanoscale features. While it may take multiple days to write a master using electron-beam lithography, modern imprinting tools can pattern full wafers in less than one minute. The promise of this technology is to leverage the nanoscale precision with the rapid throughput of stamping. In practice, it can be very difficult to achieve the same pattern fidelity in a repeatable manner. As a result, industries in which the pattern fidelity is crucial, such as in integrated

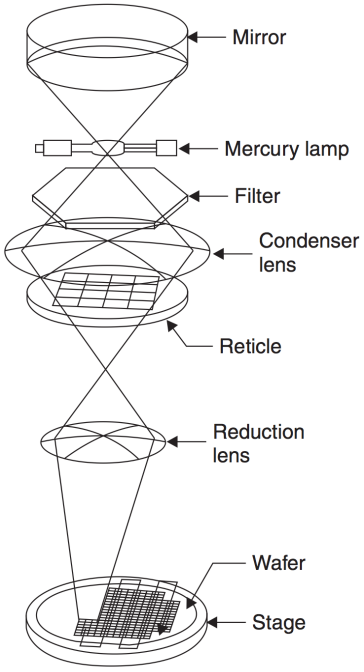

Figure 4.1: A schematic of a photolithography stepper exposure tool is depicted. The mercury lamp light is filtered, collimated, concentrated, masked in the reticle, and concentrated again. The wafer below can be translated to tessellate the image across the surface. Image from Reference [1]

circuits, have been hesitant to rely on imprint lithography.

4.2 Photolithography

Photolithography is the patterning technique at the foundation of microfabrication, the core of modern integrated circuit technology. In a photoresist, the pattern of optical irradiation is converted to a pattern of chemically distinct regions, typically through photoinitiated functional group cleavage or crosslinking. Many modern photoresists employ the concept of "chemical amplification", in which a photogenerated catalyst reacts with many sites.[2, 3] For example, photoacid generators are commonly employed in chemically amplified resists, either to catalyze a ring-opening polymerization or initiate a cascade of deprotective bond scissions within a polymer matrix, imparting new solubility properties to the irradiated regions. While there are a number of light-mediated reactions that could in principle be employed in photolithogra-

phy, very few have been implemented. Despite the fact that there are hundreds of commercially available photoresists, the functional diversity amongst these materials is severely limited. In most applications, the photoresist serves the sole purpose of a sacrificial mask or mold; very rarely is the resist material incorporated as a structural element or chemically functional interface. The ability to generate new kinds of chemically functional materials directly via photolithography would enable a host of new applications, for example in microelectromechanical systems (MEMS), microfluidics, patterned biomaterials, and artificial optical materials.

A photoresist is a material system capable of undergoing a photoactivated chemical change, such that the properties of the irradiated domains contrast those of the starting material. Other synonymous terms include photopolymers and photocurable resins. We will primarily use the term photoresist throughout this thesis for simplicity, though in many cases the final pattern is not meant to "resist" another chemical process. Additionally, we will focus on photoresists that are primarily organic. Photopatterning via the light-induced heating and sintering of inorganic particles represents another class of patternable materials that we will not discuss further.

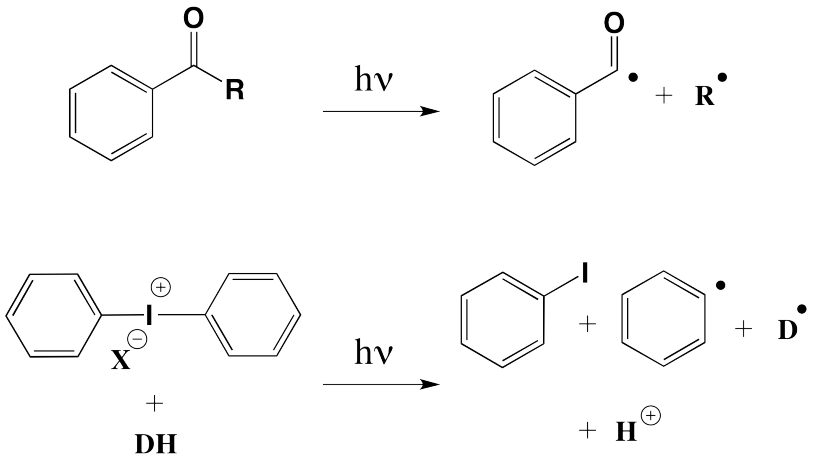

Figure 4.2: Two representative mechanisms for (top) photoradical and (bottom) photoacid generation.

The two most common photoactivation mechanisms in lithography are photoradical and photoacid generation. Figure 4.2 depicts two representative examples. Aromatic ketones can undergo photoinduced bond homolysis to generate radical pairs,

which can then initiate radical polymerization of unsaturated monomers such as acrylates and styrenes. Photoradical initiation is widely used in UV-curing applications, in part due to the wide variety of available monomers and oligomers for radical polymerization. The second wide-spread mechanism is via acid-catalyzed chemistry, initiated by a photoacid generator (PAG). Acid-catalyzed polymerizations of epoxides and vinyl ethers are often utilized to form crosslinked UV-curable gels. These types of photoresists, in which a liquid or semi-solid resin is crosslinked into a solid matrix, are referred to as "negative" photoresists, because the irradiated region remains as the image. PAGs can also be used to make "positive" photoresists, where the irradiated portions can be selectively dissolved. Acid-catalyzed deprotection of esters and carbonates is one example of a positive resist, where the ester deprotection drastically increases the polarity of the irradiated regions, which are washed away in a polar solvent.

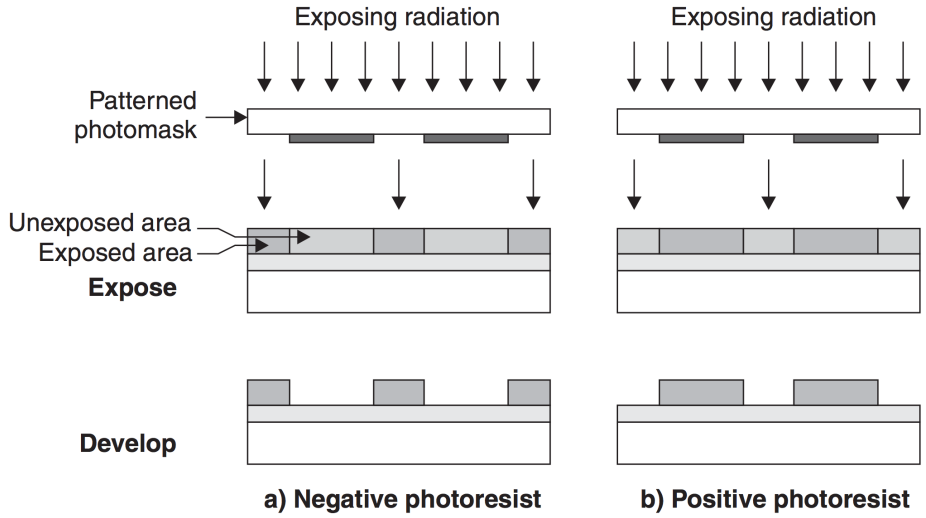

Figure 4.3: In a negative photoresist, the illuminated domains are retained, typically via crosslinking or polarity-changing deprotection. In a positive resist, the illuminated domains are selectively removed, typically via polarity-changing deprotection. Image from Reference [1].

A key design element of many photoresists is the concept of chemical amplification.[2, 3] In a chemically-amplified photoresist, a photoactivated event begins a cascade of reactivity through the generation of a catalyst. Acid-catalyzed thermolysis of esters is widely regarded as the first example of a chemically-amplified photore-

sist.[2, 3] In this system, the acid generated by the arlyonium PAG is used to catalyze thermolytic ester deprotection by heating the film after exposure. Each equivalent of acid can deprotect thousands of equivalents of ester, and thus the photochemistry has been "amplified". The advantage of an amplified system is that the total optical flux into the material can be very low. This was a critical advance in the early days of lithography, because high-power UV sources were expensive and the throughput time of the photolithographic process was the major cost driver.

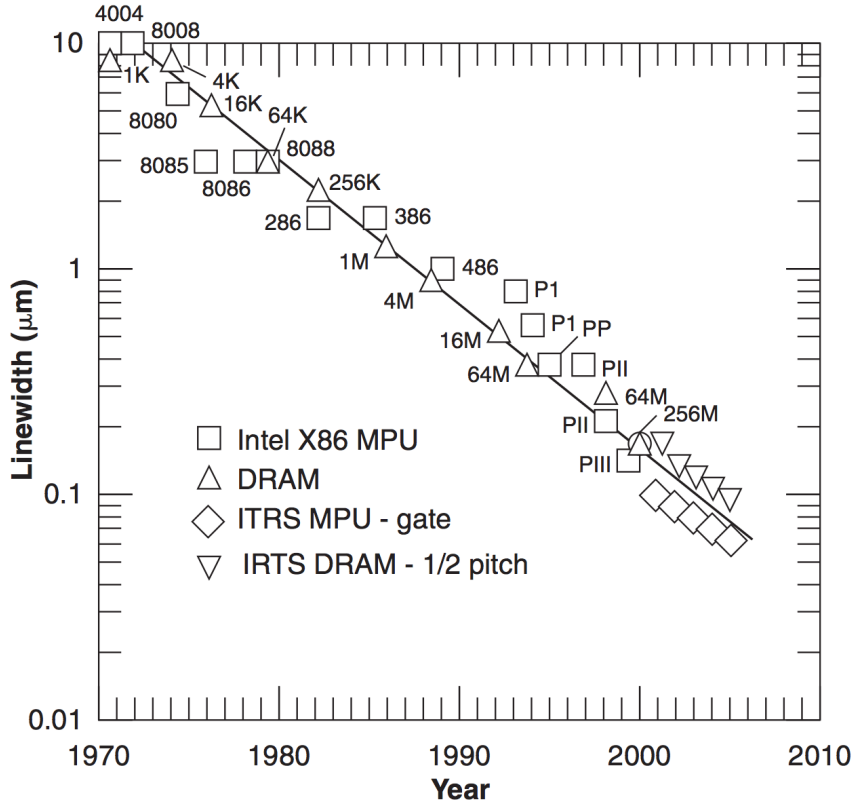

Figure 4.4: A selected history of photolithography linewidth improvement, to illustrate Moore's Law. Image from Reference [1].

Today, chemically amplified resists are less common in integrated circuit fabrication, in part because one of the most valuable properties of a photolithographic properties is the resolution. In a chemically amplified system, the acid diffusion lowers the resolution. With the availability of modern high-intensity light sources, the throughput times have been dramatically reduced. The resolution of photolithography is a direct driver of Moore's Law, the observation (and prediction) that the

density of transistors on an integrated circuit chip would double every two years. Figure 4.4 shows historical trends in photoresist linewidths.[1]

One other mechanism for improving the resolution is through multiphoton activation using a highly focused light-source, with an energy significantly lower than that required to activate the chemistry. Due to the statistics of absorption events, multiphoton absorption can beat the diffraction limit. Multiphoton lithography is particularly relevant to 3D nanofabrication and will be discussed in more detail in Chapter 7.

4.3 3D Printing

While most of the research and development of photolithographic processes has been in the context of 2D patterning of thin films, 3D implementations of these ideas have matured over the last few decades into blossoming technologies. Stereolithography (SLA) (also called optical fabrication, photo-solidification, solid imaging, and resin printing) was invented in 1986 by Charles Hull, it utilizes the iterative printing of thin layers of photoresist to build up a 3D object.[4] A beam from a blue or UV diode is rastered in a 2D plane to crosslink a negative photoresist. After each layer is written, the stage on which the object is being written is translated, fresh resin flows into the plane, and the process repeats. Digital light processing (DLP) is a variant of this approach, where a reconfigurable mask is used to digitally project a 2D image onto each plane. In principle, this has a higher throughput than SLA, as there is no time spent rastering. Very recently, a version of DLP was engineered such that the stage can be continuously translated, instead of the write-stop-reflow-translate process described above. This variant is called continuous liquid interface production (CLIP) [5]; it can write certain structures $\sim$ 100x faster than currently available SLA printers. While this is certainly an exciting development for printing many open geometries, the speed of the CLIP process is mass-transport limited, making it difficult to obtain large solid structures at these improved write speeds.

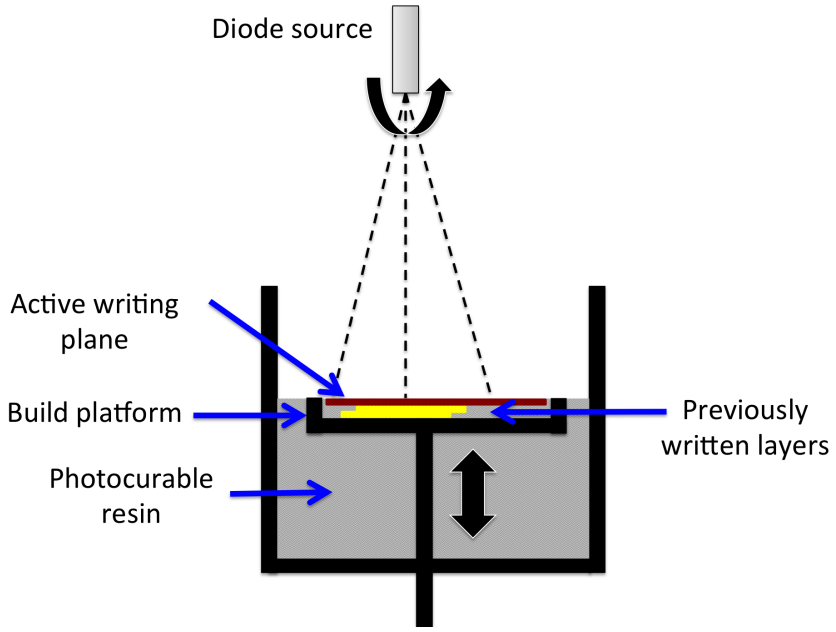

Figure 4.5: A schematic representation of stereolithography. The photoresist is cured in layers by rastering a diode source in one plane at a time, building up the structure slice-by-slice.

4.4 Towards Functional Lithography

Current methods for patterning functional materials are highly inefficient, due to the incompatibility of existing chemistry with materials having tailored optical, mechanical, and biological properties. As a result, many desirable structured materials are prohibitively expensive to fabricate and lead to environmentally harmful waste. There is a critical need to replace these methods with a straightforward, cradle-to-cradle approach to the fabrication of functional materials, interfaces, and nanostructures. Despite the fact that there are hundreds of commercially available photoresists, the functional diversity amongst these materials is severely limited. In most applications, the photoresist serves the sole purpose of a sacrificial mask or mold; very rarely is the resist material utilized as an intentional element. This is because the acid- and radical-catalyzed reactions used to pattern the resists are inherently incompatible with many desirable functional groups and materials. This chemical incompatibility manifests as an incredible amount of inherent waste; in addition to the waste generated in making photoresists, the material is discarded in its entirety by the end of

the process. To enable the direct patterning of functional materials, we need new chemistry.

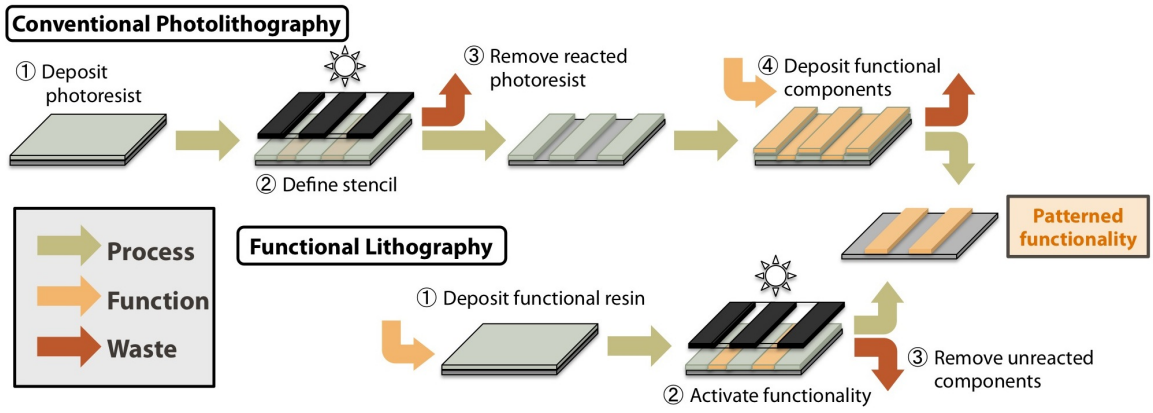

Figure 4.6: The key concept of functional lithography is the direct patterning of the desired materials properties. This reduces the overall number of steps involved to achieve a given patterned functionality, as well as the waste associated with first generating a stencil, and subsequently removing the stencil and any excess functional material.

References

(1) Jones, S. W. *IC Knowledge LLC* **2008**, *1*, 1–109.

(2) Ito, H.; Willson, C. G. *Polymer Engineering & Science* **1983**, *23*, 1012–1018.

(3) Frechet, J. M. J.; Ito, H.; Willson, C. G. *Proc. Microcircuit Eng* **1982**, *82*, 260.

(4) Hull, C. W., *Apparatus for production of three-dimensional objects by stereolithography*, US Patent 4,575,330; Google Patents: 1986.

(5) Tumbleston, J. R.; Shirvanyants, D.; Ermoshkin, N.; Janusziewicz, R.; Johnson, A. R.; Kelly, D.; Chen, K.; Pinschmidt, R.; Rolland, J. P.; Ermoshkin, A.; Samulski, E. T.; DeSimone, J. M. *Science* **2015**, *347*, 1349–1352.

Chapter 5

Photoactivation of Ruthenium Olefin Metathesis Catalysts

Portions adapted with permission from Weitekamp, R. A.; Atwater, H. A.; Grubbs, R. H. "Photolithographic Olefin Metathesis Polymerization". *J. Am. Chem. Soc.* **2013**.

Chapter Abstract

Patterning functional materials is a central challenge across many fields of science. The ability to lithographically fabricate micro- and nanostructures has been one of the most impactful technological breakthroughs of the last century. In part due to the complexity of the chemical processes in photoresists, there is a limited variety of materials that can currently be patterned by photolithography. We report a negative tone photoresist using a photoactivated olefin metathesis catalyst, which can be quickly prepared in a one-pot synthesis from commercially available starting materials. The resist is based on a ruthenium vinyl ether complex, widely regarded as inactive towards olefin metathesis. The combination of this photoactivated catalyst with the fidelity and functional group tolerance of ruthenium-mediated olefin metathesis enables a host of new possibilities for photopatterned materials.

5.1 Introduction

Olefin metathesis is a robust synthetic methodology that has led to new polymeric materials with many applications, such as drug delivery,[1] organic electronics,[2] and photonic crystals.[3, 4] A number of latent olefin metathesis catalysts have been developed, using variety of activating stimuli, including pH, heat, and light.[5, 6] Photoinitiated ring opening metathesis polymerization (ROMP) has been demonstrated with many different transition metals, including tungsten,[7] ruthenium,[8–10] and molybdenum.[11] Photoinitiation mechanisms include triggered alkylidene formation,[7] as well as ligand dissociation through both direct photoexcitation[8] and indirectly via a photoacid generator.[9, 10] Despite these many examples, an olefin metathesis based photoresist has not yet been developed. Part of the challenge in developing such a system is achieving a stark contrast between the reactivity of the catalyst in the light and the dark. Additionally, the requirements of ambient stability and processability present barriers to the industrial implementation of transition metal based photocatalysts. We demonstrate that the standard quenching procedure for ROMP reactions generates a photoactive latent catalyst and exploit this serendipitous discovery in the facile synthesis of a new family of photocurable materials.

The addition of vinyl ethers is a widely employed method of quenching ROMP reactions.[12] The regioselective formation of vinyl ether complexes is extremely rapid and irreversible under certain conditions, leading to the use of vinyl ether trapping as a tool for determining catalyst initiation rates.[13] The resultant Ru Fischer-type carbenes are generally considered to be unreactive, although our group previously reported that some of these complexes can be competent olefin metathesis catalysts at elevated temperatures.[14] Quenching a living ROMP reaction yields a methylene-terminated polymer chain and a presumably 14-electron ruthenium vinyl ether. While the phosphine or pyridine ligands typically found on ruthenium ROMP catalysts could in principle re-coordinate to the quenched complex, the statistical likelihood of this is low considering the concentration and stoichiometry of typical ROMP reactions. In addition, the air-sensitivity of the ruthenium vinyl ether complexes certainly aids

in the quenching process, through almost immediate decomposition of the alkylidene species. A typical quenching procedure utilizes excess vinyl ether and immediate precipitation of the polymer to remove the catalyst. We show that if this sensitive ruthenium vinyl ether complex can be stabilized, reactivity can be retriggered by ultraviolet (UV) irradiation.

Here we report a method of patterning using a ruthenium photocatalyst, which we term PhotoLithographic Olefin Metathesis Polymerization (PLOMP). In this procedure, a latent metathesis catalyst is activated by light to react with the olefins in the surrounding environment. We demonstrate a negative tone resist by using the photocatalyst to crosslink a difunctional ROMP monomer within a matrix of linear polymer. In principle, a positive tone resist could also be developed by using light-triggered secondary metathesis events to increase the solubility of the irradiated regions. This can be considered a "chemically-amplified" resist, in that the photoactive species is a catalyst for the crosslinking of the polymer matrix. The versatility of ruthenium-mediated olefin metathesis can now be utilized to photopattern a variety of functional materials via PLOMP, advancing the field of photoinitiated olefin metathesis from a curiosity to materials science applicable to mass micro-fabrication.

5.2 Results

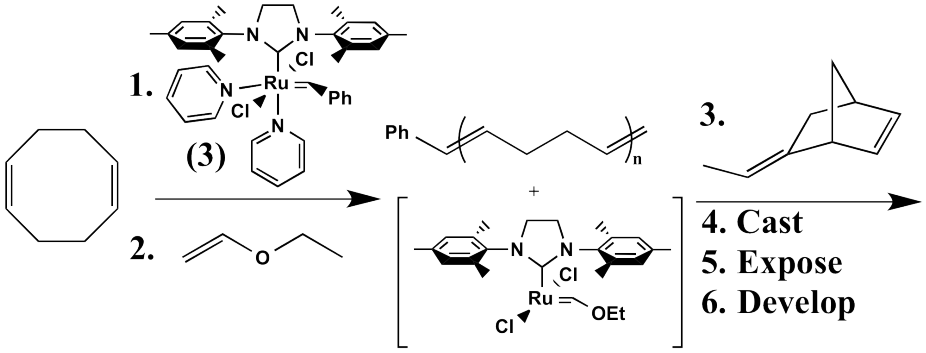

Figure 5.1: The one-pot preparation of a PLOMP resist. **PLOMP Recipe 1.0**

Our one-pot preparation from commercially available starting materials can be completed in the span of a few hours. It should be noted that the photoactive vinyl

ether complex is sensitive to oxygen, heat and light. Preparation of the resist should be carried out under an inert atmosphere for best results. First, complex **3** is employed to afford the ROMP of 1,5-cyclooctadiene (COD) (Figure 5.1). This reaction is sufficiently complete in minutes, and is subsequently quenched with ethyl vinyl ether. After removing the volatiles in vacuo, the linear poly(COD) is dissolved in a difunctional monomer, such as 5-ethylidene-2-norbornene (ENBE). The chemical composition and molecular weight of the linear polymer, the amount of ENBE and the excess of vinyl ether can all be modulated to tune the properties of the photoresist. The presence of some excess vinyl ether is beneficial for mitigating dark polymerization of the resist material. In our PLOMP resists, the high viscosity of the solution as well as the possibility of dative bonding from the surrounding olefins likely contribute to stabilizing the photocatalyst (Figure 5.2). Despite the sensitivity of the ruthenium vinyl ether complexes, we found that viscous resist solutions could be used successfully under ambient benchtop conditions for months.

These olefin-rich solutions proved to be competent UV photoresists, at both 254 nm and 352 nm. Silicon coupons (1 cm^2) were cleaned with piranha and rinsed with copious amounts of deionized water, isopropanol, and acetone. For consistent adhesion, the coupons were first heated to 150 °C for 1-2 minutes to remove adventitious moisture and cooled under a stream of argon immediately prior to casting. Approximately 0.1 mL of the resist solution was deposited on each 1 cm^2 coupon and spun at 2500 - 7000 RPM for 60 seconds, depending on the desired thickness. Under 254 nm irradiation, we were able to cure 1-2 micron thick films in 60 to 90 seconds using a benchtop 8-watt lamp. With our 352 nm blacklight bulb, the necessary exposure times were significantly longer, ranging from 5-15 minutes depending on the batch and film thickness. Films up to approximately 500 nm thick were patterned at wafer scale using printed photomasks (Figures 5.3 & 5.4). We were able to reliably fabricate bar structures with a width and spacing down to 30 microns with good fidelity (Figure 5.3). Optimization using a commercial mask aligner and collimated source will certainly improve the resolution and fidelity of our PLOMP resists. While we were able to work with some batches of the resist under ambient conditions for many weeks

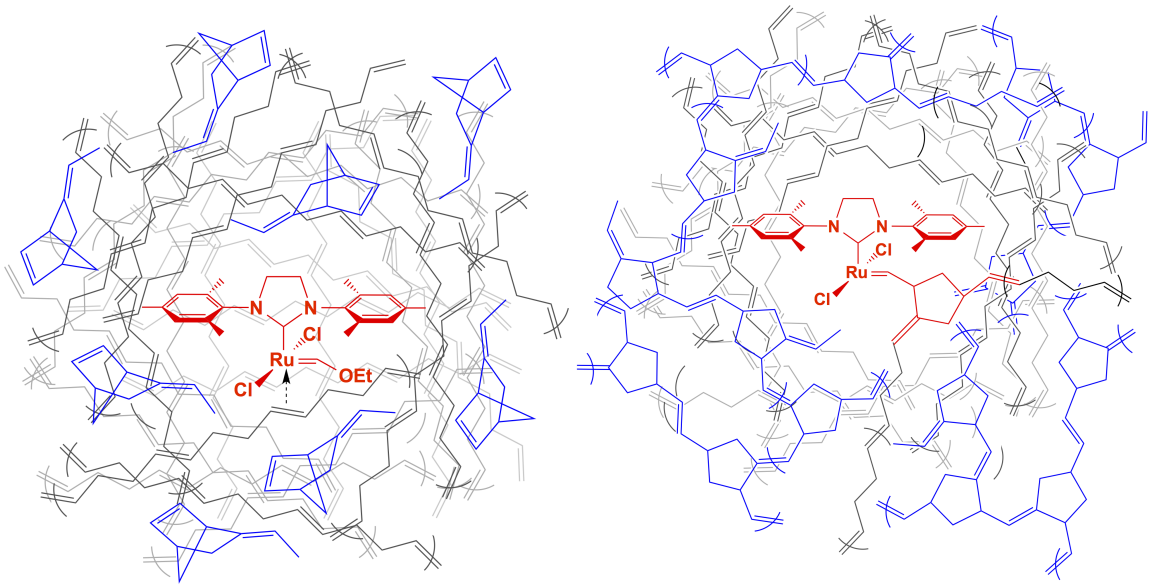

(a) The proposed latent resisting state

(b) After irradiation, the catalyst begins crosslinking.

Figure 5.2: A cartoon depicting the proposed environment of the PLOMP resist. We propose that the viscous, olefin rich solution stabilizes the sensitive vinyl ether complex through dative bonding, as depicted. The photoactivated catalyst (red) crosslinks the ethylidene norbornene molecules (blue) into the matrix of poly(COD) (gray).

before the performance deteriorated, a significant delay between spin casting and exposure led to inconsistent results. This is not surprising, considering the increased surface-to-volume ratio after spin casting and the known air-sensitivity of these vinyl ether complexes. The onset of background (dark) crosslinking of the difunctional monomer may also contribute to this observation.

One advantage of our PLOMP resist over many commercial resists is the ability to maintain surface adhesion to the native oxide surfaces of silicon wafers without any specialized surface treatment. By contrast, many commercial photoresists require HF etching of the oxide and/or surface derivatization with reactive molecules such as hexamethyldisilazane. In this respect, our PLOMP resists offer a safer and more versatile alternative, as the polymer composition can be easily tuned to modulate adhesion.

Currently, ruthenium-mediated ROMP is employed in a number of industrial scale

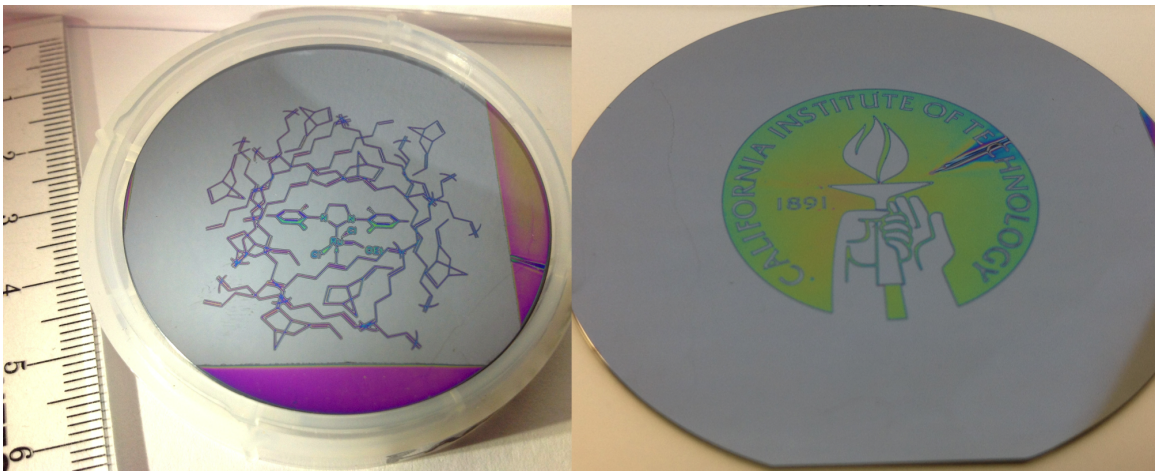

Figure 5.3: PLOMP was used to pattern 2-inch diameter silicon wafers with a black-light lamp ($\lambda = 352$nm) and a printed photomask.

applications, including high-modulus resins and extremely chemically resistant materials. PLOMP can provide UV-curable and patternable coatings with these desired materials properties. Finally, the ability to generate many batches of resist in a single workday enables rapid prototyping for future development. After finishing this proof-of-principle demonstration, we sought to develop PLOMP into a platform for patterning functional materials.

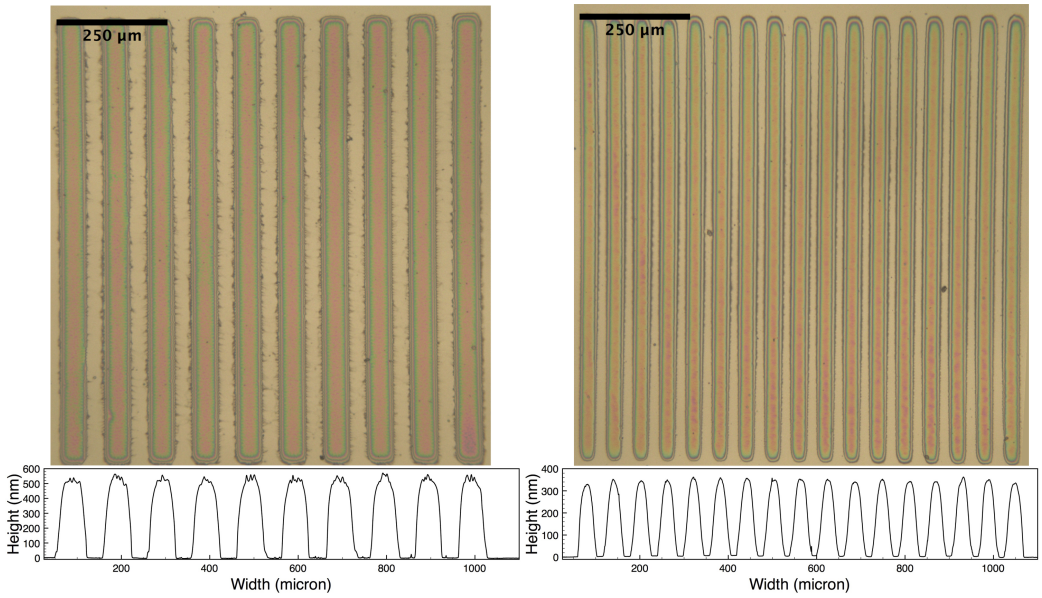

Figure 5.4: (Top) Micrographs of 1 mm long bars, with widths of 50 μm (left) and 30 μm (right). (Bottom) The height profiles of the same bar arrays are shown, as measured by profilometry.

5.3 PLOMP 1.0 - Recipe

A standard PLOMP resist recipe, Version 1.0: catalyst **3** (1.3 mg) was placed under argon and dissolved in 2 mL dichloromethane. To this catalyst solution was quickly added 1.5 mL 1,5-cyclooctadiene, the solution became a semi-solid in 10 seconds and was allowed to react for 1 minute before quenching with 3 mL ethyl vinyl ether. The viscous solution was slowly stirred for 5 minutes, sealed under argon, and sonicated for 1 hour. The volatiles were removed on a rotary evaporator, to yield semisolid poly(COD), colored light yellow by the quenched catalyst (the photoactive vinyl ether complex). Ethylidene norbornene (10 mL) was added to this mixture, which was cooled to 0 °C and sonicated for 1 hour. The partially dissolved mixture was placed on an ice bath and stirred until fully dissolved, while allowing the bath to warm to room temperature. The result is a light yellow, viscous solution weighing approximately 10 grams.

5.4 Control Experiments

To show that the catalyst is necessary for the resist to function, the standard resist prep was used except the polymer was precipitated into methanol to extract the quenched catalyst. Catalyst **3** (1.3 mg) was placed under argon and dissolved in 2 mL dichloromethane. To this catalyst solution was quickly added 1.5 mL 1,5-cyclooctadiene, the solution became a semi-solid in 10 seconds and was allowed to react for 1 minute before quenching with 3 mL ethyl vinyl ether. The viscous solution was very slowly stirred for 5 minutes, after which 5 mL methanol was added. The suspension was sonicated for 20 minutes, the brown solution was decanted, and the off-white solid polymer was washed three times with 10 mL of methanol. The polymer was dried in vacuo, and dissolved in 10 mL 5-ethylidene-2-norbornene to afford a very pale yellow, viscous solution. This solution was cast as before and exposed for 6 minutes at 254 nm (4 times the standard exposure for the analogous resist) with no evidence of pattern formation. After developing with hexanes, a clean Si surface was recovered. As well, prolonged irradiation of pure ENBE at both 254 nm and 352 nm did not render any change in viscosity or other evidence of crosslinking. The addition of BHT (2,6-Di-tert-butyl-4-methylphenol) to the PLOMP resist did not appear to change its behavior, which suggests that the mechanism does not involve radicals.

To support the hypothesis that the ruthenium vinyl ether complex is intact inside the PLOMP resist, the 1H NMR spectra of a PLOMP resist and complex **5** were compared. The resist was prepared by the standard recipe above. Complex **5** was prepared as reported by Louie. The spectra strongly support the proposed composition of the PLOMP photoresist; the alkylidene protons in each spectrum are less than 1 ppm apart (Figure 5.5).

^{1}H NMR spectra in CD_2Cl_2 of complex **5** and a PLOMP photoresist. The region of the alkylidene proton is shown to highlight the similarity between the two. No other peaks were observed in the downfield region (δ = 11 - 22 ppm), suggesting that no other ruthenium alkylidene species are present in any significant quantity.

To support the hypothesis that dative bonding from the highly olefinic resist sta-

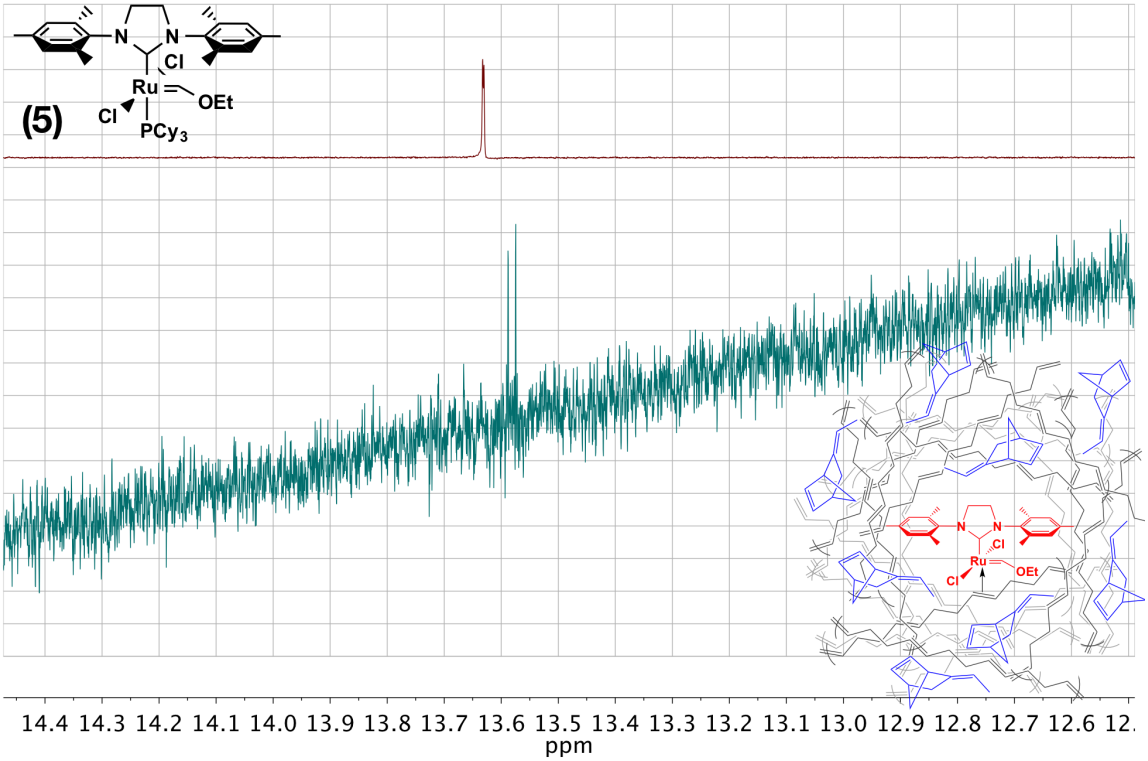

Figure 5.5: The carbene regions of the ^{1}H NMR spectra are compared. The shift of the PLOMP resist is within 1 ppm of the Ru vinyl ether complex reported by Louie. [14]

bilizes the photoactive complex, two experiments were performed. First, the formally 14-electron ruthenium vinyl ether species can be prepared by quenching the 2nd generation Grubbs-Hoveyda catalyst with ethyl vinyl ether. This complex immediately crosslinks ENBE, suggesting that there is a ligand present in the resist that stabilizes the photoactive catalyst. Obvious candidates for this ligand include the original pyridine ligands from complex **3** or the olefins in the viscous resist material. Wenzel and coworkers have demonstrated the ability to remove pyridine ligands using acids such as trifluoroacetic acid (TFA).[15] If only the removal of a pyridine ligand was required to reactivate the complex, we would expect that crosslinking could also be triggered by acid. However, the addition of TFA lead to no change in viscosity after 24 hours. In fact, the PLOMP resist was still able to function in the presence of TFA; no change in behavior was observed for 254 nm photopatterning, 30 minutes after adding TFA. While these experiments do not explicitly rule out the presence of

a pyridine-coordinated complex, they strongly suggest that dative bonding from the surrounding olefins is the more likely mechanism of catalyst stabilization. This olefin could belong to the poly(COD), ENBE, or excess ethyl vinyl ether.

References

(1) Johnson, J. A.; Lu, Y. Y.; Burts, A. O.; Xia, Y.; Durrell, A. C.; Tirrell, D. A.; Grubbs, R. H. *Macromolecules* **2010**, *43*, 10326–10335.

(2) Sailor, M. J.; Klavetter, F. L.; Grubbs, R. H.; Lewis, N. S. *Nature* **1990**, *346*, 155–157.

(3) Sveinbjörnsson, B. R.; Weitekamp, R. A.; Miyake, G. M.; Xia, Y.; Atwater, H. A.; Grubbs, R. H. *Proceedings of the National Academy of Sciences* **2012**, *109*, 14332–14336.

(4) Miyake, G. M.; Piunova, V. A.; Weitekamp, R. A.; Grubbs, R. H. *Angewandte Chemie International Edition* **2012**, *51*, 11246–11248.

(5) Monsaert, S.; Vila, A. L.; Drozdzak, R.; Van Der Voort, P.; Verpoort, F. *Chemical Society Reviews* **2009**, *38*, 3360–3372.

(6) Vidavsky, Y.; Lemcoff, N. G. *Beilstein journal of organic chemistry* **2010**, *6*, 1106–1119.

(7) Schaaf, P. A. van der; Hafner, A.; Muhlebach, A. *Angewandte Chemie International Edition in English* **1996**, *35*, 1845–1847.

(8) Wang, D.; Wurst, K.; Knolle, W.; Decker, U.; Prager, L.; Naumov, S.; Buchmeiser, M. R. *Angewandte Chemie International Edition* **2008**, *47*, 3267–3270.

(9) Keitz, B. K.; Grubbs, R. H. *Journal of the American Chemical Society* **2009**, *131*, 2038–2039.

(10) Khalimon, A. Y.; Leitao, E. M.; Piers, W. E. *Organometallics* **2012**, *31*, 5634–5637.

(11) Subbotina, I. R.; Shelimov, B. N.; Kazansky, V. B. *Kinetics and catalysis* **1997**, *38*, 678–684.

(12) Maynard, H. D.; Okada, S. Y.; Grubbs, R. H. *Macromolecules* **2000**, *33*, 6239–6248.

(13) Sanford, M. S.; Love, J. A.; Grubbs, R. H. *Journal of the American Chemical Society* **2001**, *123*, 6543–6554.

(14) Louie, J.; Grubbs, R. H. *Organometallics* **2002**, *21*, 2153–2164.

(15) Wenzel, A. G.; Blake, G.; VanderVelde, D. G.; Grubbs, R. H. *Journal of the American Chemical Society* **2011**, *133*, 6429–6439.

Chapter 6

Functional Lithography via PLOMP

Chapter Abstract

The previous chapter described the discovery of photoactuated reactivity of otherwise latent ruthenium complexes. In this chapter, we summarize our efforts to transform this discovery into a platform for patterning functional materials. We present three strategies for functional group incorporation, as well as a preliminary substrate scope for PLOMP. The poor stability of our pre-catalysts towards oxygen and heat was improved through the addition of stabilizing ligands. A substrate scope study demonstrates compatibility of PLOMP with a variety of functional additives. Ongoing efforts towards a number of specific applications of PLOMP are presented, such as robust chemical etch masks, peptide-functional surfaces towards biologically active scaffolds, new nanoimprintable materials, and electrocatalytic thin-films.

6.1 Strategies for Functional Group Incorporation

The functional group tolerance of ruthenium-mediated olefin metathesis has been leveraged to access a wide-variety of materials with tailored chemical, mechanical, optical and biological properties.[1] We have begun to explore the tolerance of our PLOMP process towards other functionalities, in hopes of developing a toolbox for materials patterning applications. We have demonstrated three complementary techniques for incorporating functionality into our PLOMP resists. The simplest method of diversification is simply via the addition of a functional molecular additive containing an olefin capable of cross- or ring-opening metathesis. This approach enables the rapid derivatization of a single "parent" recipe, but is limited by the chemical compatibility of the additive with the resist solution. This can present a challenge for highly polar additives, for example, as the parent resists are composed almost entirely of hydrocarbons. Additionally, it can be difficult to predict the degree to which the functionality will be incorporated into the material, which will depend on the local concentration and rate of metathesis relative to other crosslinking events. This method is also typically limited to relatively low loadings of functional additives, largely due to the solubility of the additive in the resist.

Alternatively, we have demonstrated the ability to copolymerize functional ROMP monomers into the poly(cyclooctadiene) backbone to guarantee the incorporation of the desired functionality into the linear polymer matrix. In this method, the degree of incorporation can be precisely defined and quantified before photopatterning. One downside to this approach is that many of the processing conditions for lithography, such as thin-film casting parameters or development chemistry, will likely need to be re-optimized to a greater extent than in the molecular additive approach. Nevertheless, once this process has been developed, this approach has many advantages over the molecular additive route.

Finally, functionality can be specifically incorporated onto the polymer chain ends, via the use of a symmetric internal olefin.[2, 3] These olefins are often referred to as "chain-transfer agents", as they terminate the chain with a functionality and release

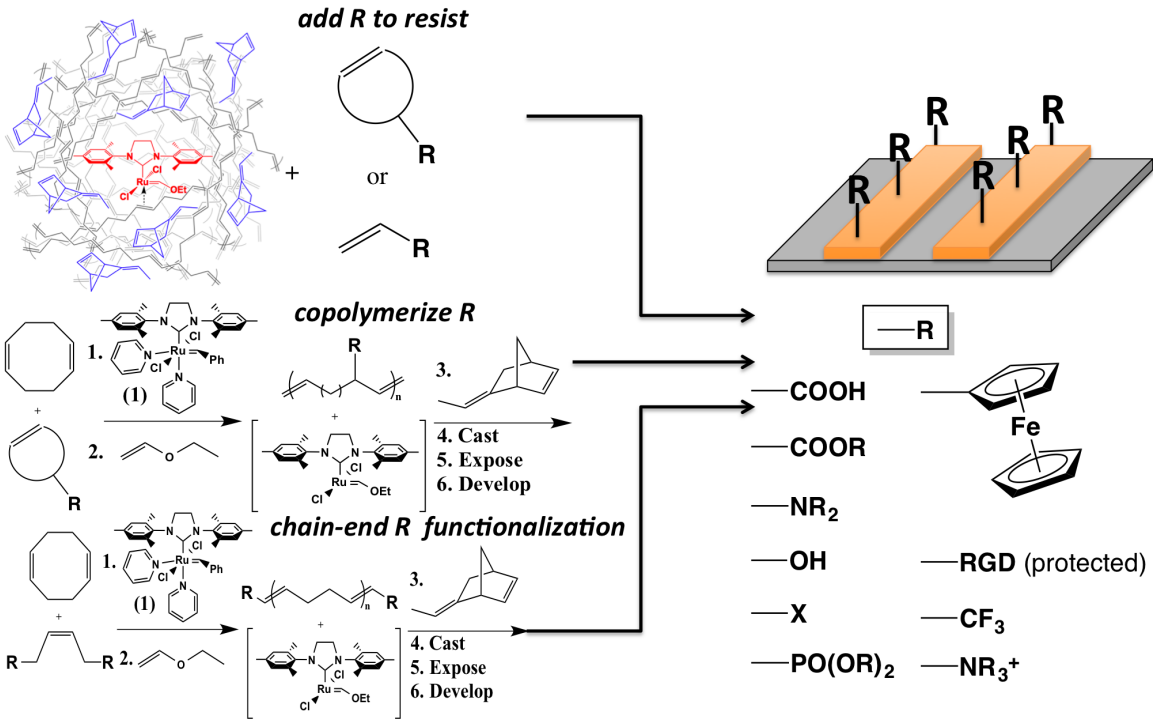

Figure 6.1: Three routes to functional group incorporation: directly via molecular additives, and via copolymerization with a functional monomer, via a functional chain-transfer agent.

the catalyst, to initiate a new polymer chain. They can be utilized to simultaneously control the molecular weight of the polymerization, as well as provide specific functionality to the chain ends, resulting in so-called "telechelic" polymers. This approach offers alternative architectures which could provide unique chemical properties, such as chain-end coupling or tailored rheology. One use of chain transfer agents has been to incorporate multiple polymerization mechanisms into a single polymeric backbone, which could prove useful in designing tailored materials properties.[3]

6.2 Improving the Pre-catalyst Stability

One of the original inspirations for the development of a metathesis-based photoresist was the idea of being able to photopattern highly crosslinked materials, such as poly(dicyclopentadiene) (poly(DCPD)). After the development of our initial PLOMP resist using ENBE & poly(COD), we sought to develop a strategy to enable the pho-

topatterning of pure poly(DCPD). As shown in Figure 6.2, we were able to perform a partial polymerization of DCPD, by mitigating the reactivity with excess pyridine and quenching the reaction at the desired viscosity with various alkyl vinyl ethers. This viscous solution could then be cured using ultraviolet light to a crosslinked solid.

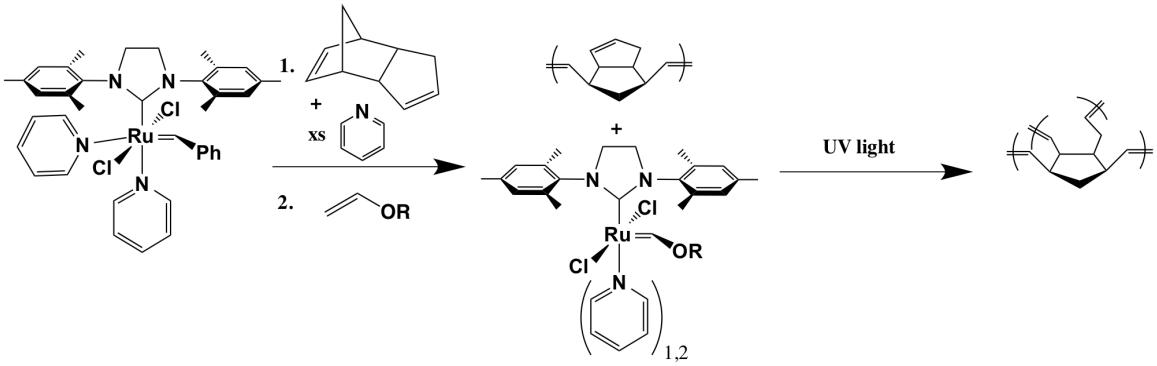

Figure 6.2: In our first attempt towards an all-DCPD PLOMP photoresist, we employed an excess of pyridine to slow down catalyst **3**. Through this controlled polymerization, we were able to quench the reaction at the desired viscosity using alkyl vinyl ethers. Irradiation re-activates the catalyst to afford a crosslinked solid.

One significant drawback to the strategy presented in Figure 6.2 is that the partially-cured resins eventually crosslinked over the course of a few days when stored dark at ambient temperature. Presumably the high-reactivity of DCPD facilitates this background reactivity, which is exothermic and highly non-linear. We sought to address this challenge through the incorporation of additional ligands in order to develop a more latent PLOMP pre-catalyst.

A handful of ligands were screened and are depicted in Figure 6.3. The general conditions for these studies involved the partial polymerization of DCPD via catalyst **2**, quenching at the desired approximate viscosity with ethyl vinyl ether and one of the ligands. Only 1,10-phenanthroline was able to stabilize the catalyst such that the reaction mixture was stable in the dark for weeks or months. During these studies, we found it more reliable to use **2**, as it takes tens of minutes in DCPD solutions before there is any apparent change in viscosity. By contrast, catalyst **3** will fully crosslink DCPD in less than one minute, unless inhibited by excess ligands such as phosphines or nitrogen donors.

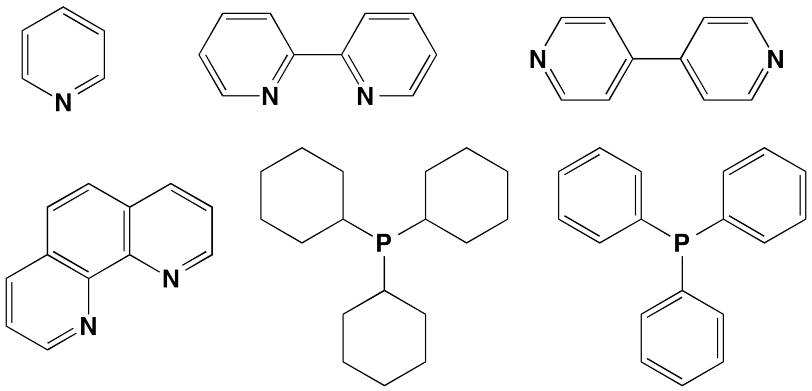

Figure 6.3: These ligands were added to the DCPD-based resist above, in an attempt to stabilize the pre-catalyst. Only 1,10-phenanthroline resulted in a solution which was stable for many months.

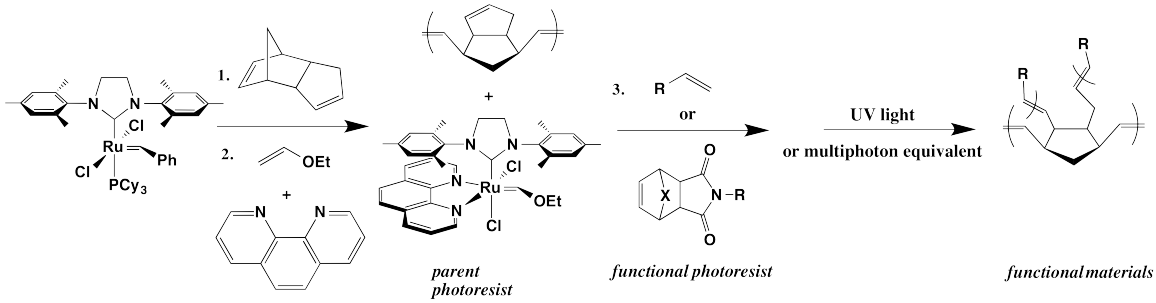

Figure 6.4: This figure outlines the process of derivatizing PLOMP 2.0 photoresists with molecular additives. First, the partial polymerization of DCPD is afforded via catalyst **2**, and quenched at the desired viscosity. This parent resist can then be derivatized with various additives, to rapidly produce functional variants.

We were able to isolate the proposed latent pre-catalyst via an analogous synthetic approach, as described in Section 8.3. Interestingly, the crystal structure of the 1,10-phenanthroline adduct, complex **6** revealed an isomerization of the chloride ligands from *trans* to *cis*. Presumably the steric clash of the phenathroline and the mesityl groups of the NHC ligand are a major cause for the preference of this isomer in the solid state. There is some evidence from our group and others which suggests that the *cis*-chloride isomer of related complexes are not kinetically competent for olefin metathesis, and must first isomerize to the *trans* configuration before entering the catalytic cycle.[4, 5] This isomerization event could account for some of the improved latency of this complex, compared to the other Fischer-type carbenes studied here.

Key advantages of the phenanthroline-chelated precatalyst include improved sta-

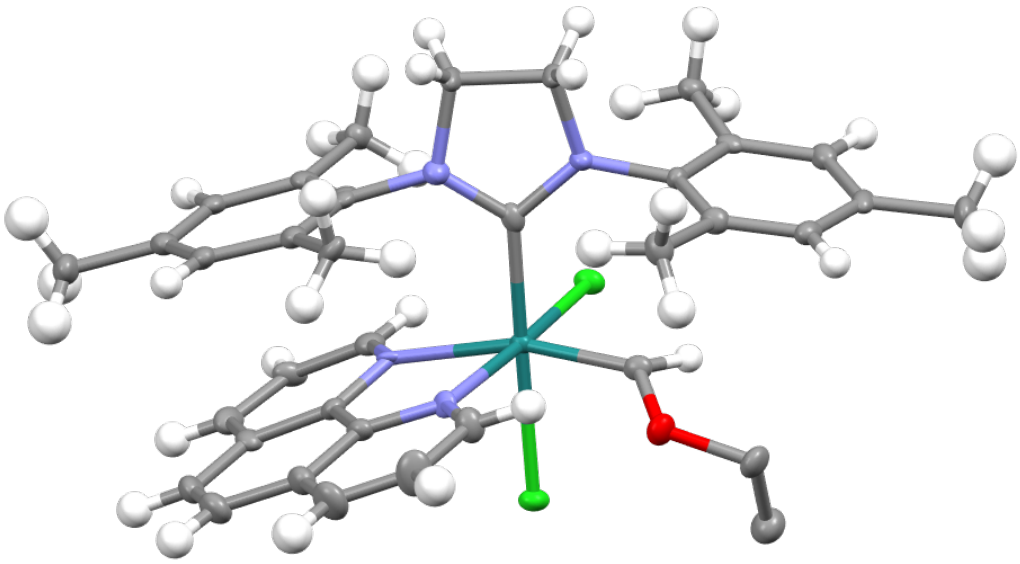

Figure 6.5: The solid-state structure of our phenanthroline-chelated precatalyst, complex **6**, reveals isomerization of the chloride ligands to a *cis* configuration.

bility towards heat and oxygen, in stark contrast to the PLOMP 1.0 recipe. This enabled many of the studies on multiphoton PLOMP, described in detail in Chapter 7, as it provided both an extended working window and lifted many of the restrains on resin composition. We were able to use this marked improvement in catalyst stability to develop a modular photopatterning platform, which we will refer to as PLOMP 2.0.

6.3 PLOMP 2.0 Recipe

A solution of 95% DCPD and 5% ENBE (by volume, 10 mL in total) was first degassed with argon in a scintillation vial, placed within a room-temperature water bath, and stirred at 1500 RPM. Under argon, 2.1 mg of catalyst **2** dissolved in 100 microliters of

degassed chloroform was injected into the solution. After 25-30 minutes, the solution was at the desired approximate viscosity: still stirring, but viscous enough that the meniscus does not slosh when shaken. The reaction was quenched at this time with 2.5 mg 1,10-phenanthroline in 0.5 mL of ethyl vinyl ether, stirred for an additional 5 minutes, and stored in the dark overnight. Overnight, the light pink solution became ruby red, which we believe was due to the formation of complex **6**. This viscous red solution was used directly as a PLOMP photoresist.

6.4 Compatibility Scope of Molecular Additives

With the more stable PLOMP 2.0 resist in hand, we sought to explore the compatibility scope of molecular additives to demonstrate the utility of our patterning methodology to a variety of functional materials. Our initial efforts in this area were limited to adding small molecule, olefin-containing additives directly to the PLOMP 2.0 resist, and subsequently testing the compatibility of these added functionalities with our thin-film, UV-cured photolithography process. This versatile approach enables rapid prototyping, as a single batch of the parent resist can yield dozens of functional variants. A wide variety of additives, shown in Figure 6.6, were successfully employed using this technique, albeit at relatively low loadings.

These compounds are added by dissolving them in either chloroform or acetonitrile, then adding a small amount of this solution to a portion of the resist. The compounds shown in Figure 6.6 have all been successfully incorporated into resists at 0.1% by weight without significantly effecting the photolithographic process. A few have been incorporated successfully at 1% by weight, but at this high level of loading, solubility is a limiting factor. Typically, the functional monomers were added as chloroform or acetonitrile solutions. Often, the addition of a small amount of water is sufficient to help polar compounds to dissolve in acetonitrile. Somewhat surprisingly, the addition of water into the resist does not lead to any apparent negative effects on the basic functionality of the resist.

The improved stability of complex **6** also necessitates different processing con-

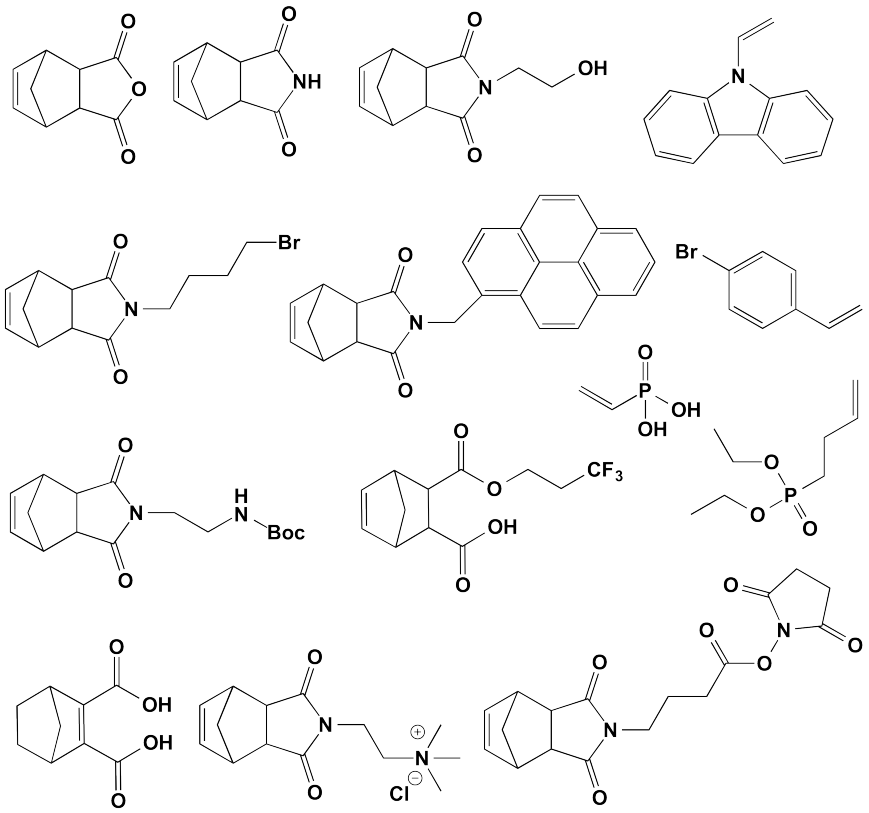

Figure 6.6: A variety of compatible molecular additives. All of these functional monomers could be incorporated into the resist at 0.1 % by weight into the PLOMP 2.0 parent resist, without impacting the lithographic process.

ditions for the PLOMP 2.0 resists. Specifically, while the PLOMP 1.0 resists were not stable at elevated temperatures, the PLOMP 2.0 resists actually benefit from both pre- and post-exposure baking steps during thin-film patterning. The benefits of pre-exposure baking for this system can be rationalized in two ways. First, there is excess vinyl ether in the parent resist that could quench the crosslinking process after photoactivation, but can be easily removed with heating. Second, the glass transition temperature of the partially polymerized poly(DCPD) in the PLOMP 2.0 resist is likely much higher than the poly(COD)-based PLOMP 1.0 resist. Pre-heating is a common strategy to relieve residual stress, rendering higher-density thin-films before patterning. The benefits of post-exposure baking can be rationalized by the fact that the phenanthroline ligand can likely re-coordinate to the ruthenium complex during crosslinking, slowing or halting the process. By heating the film after exposure, the

rate of polymerization can be increased to achieve higher crosslinking densities. The details of the patterning process are described in Section 8.3.

The results of this substrate scope study suggest that the PLOMP 2.0 photoresist can be modified to yield a versatile toolbox. The only functionalities that we specifically had trouble incorporating in any amount were alkynes. Is is possible that some form of alkyne metathesis is responsible for this observation, although we could not rule out other impurities. We were delighted to find that amines did not interfere with the patterning process, as these can be problematic for other homogeneous metathesis reactions because of their tendency to coordinate to the ruthenium center. Given that our proposed photoactivation mechanism for complex **6** is through photodissociation of an amine ligand, it is possible that these amines can also be induced to dissociate under irradiation. Post-exposure heating may also mitigate the deleterious effects of the amines on reactivity.

One of the disadvantages of the molecular additive approach to diversification is the difficultly of maintaining homogeneity throughout the process. While it was possible to incorporate low loadings (0.1%) of a variety of small molecule additives, many of these underwent phase separation at even 1% loading. Even in cases where the initial resist solution was homogeneous, some additives were found to precipitate during the spin-coating process, when a large fraction of the volatiles are removed from the material. Figure 6.7 shows an example of crystallite formation within the thin film, as seen through a microscope.

Another ongoing challenge within this project is the characterization of the final composition of the patterned film. While we have shown here the compatibility of many molecular additives with the PLOMP 2.0 resist system, we have not yet fully elucidated the extent to which the added functionalities are incorporated. Ongoing work includes the development of a method of probing the degree of functional group incorporation through Fourier Transform Infrared (FTIR) spectroscopy. Additionally, we hope to elucidate the availability of the the molecular additives to serve as active surface-functional handles for further derivatization of the material. With our current process, this has been challenging to validate for many reasons, including limited

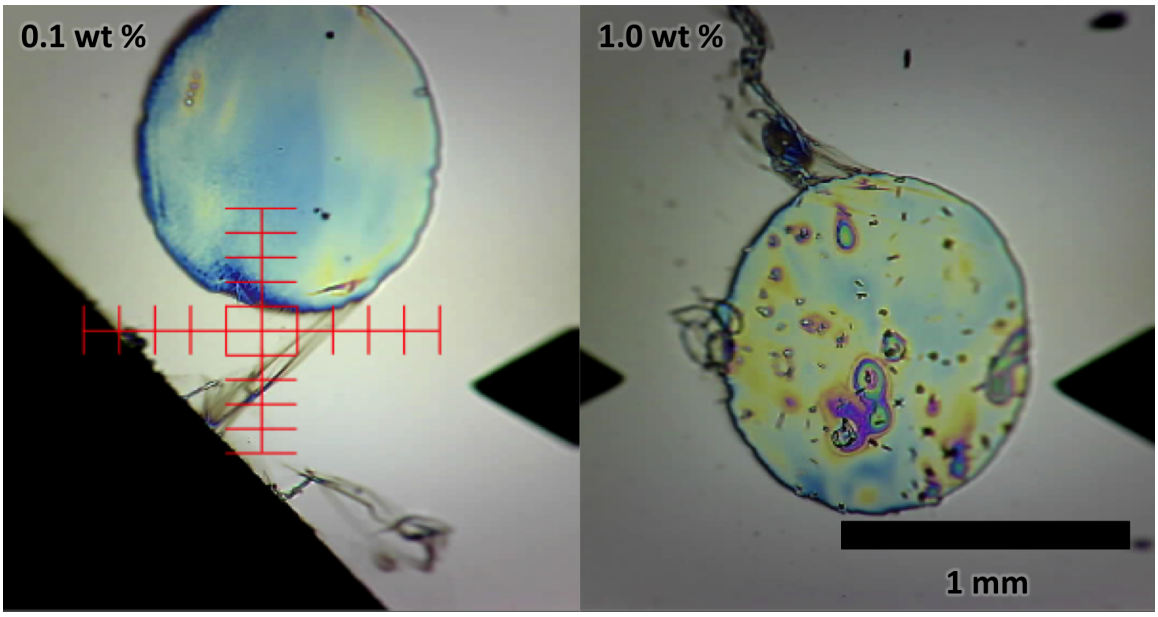

Figure 6.7: This photograph reveals that at higher loadings, the monomer additives can cause phase segregation within the PLOMP films. This particular image shows crystallization of the alcohol-functional monomer *N*-(hydroxyethanyl)-*cis*-5-norbornene-*exo*-2,3-di-carboximide at 1 wt% loading.

surface-area, low loadings, and the difficulty of preparing samples compatible with many of the highly surface-sensitive (and non-destructive) spectroscopic techniques, such as as attenuated total reflectance (ATR) methods of FTIR.

6.5 Progress Towards Robust Chemical Etch Masks

Hydrofluoric acid (HF) is used to etch silica, metal oxides and other silicate glasses. However, there are currently a very limited number of options for protecting materials from concentrated HF (50 % aqueous). A robust, patternable, HF-resistant material would enable new methods of selectively etching glass, opening up a number of applications in microfabrication. Previous solutions to this problem include the arduous patterning of chromium, polycrystalline silicon, amorphous silicon, aluminum, silicon nitride, or chromium/gold. These examples all involve many-step processes that are complex and expensive to implement. Recently, the ability to etch more than 600 microns into fused silica using a commercially available photoresist (ProTEK PSA)

from Brewer Science was reported [6], but this product has been pulled from the market due to issues of irreproducibility. In summary, while there have been a number of reported methods of masking fused silica for concentrated HF etching, the methods are either irreproducible or too complex for commercial feasibility.

The impressive acid resistance of bulk poly(DCPD) and related crosslinked ROMP polymers inspired our efforts to use our PLOMP photoresist as a corrosion-resistant mask for HF etching. Typically, buffered HF solutions are used in etching processes, because buffering favors the formation of the trifluoride anion over the fluoride. The small fluoride anion is able to diffuse much more rapidly through the polymeric networks, and can begin to etch the glass directly underneath the resist, which results in defects and peeling. Because HF etches the glass isotropically, there will always be some "undercutting", as depicted in Figure 6.8. If the adhesion between the resist and the substrate is not sufficiently strong, the peeling of the resist away from the feature edge can drastically effect the geometry of the resulting structure.

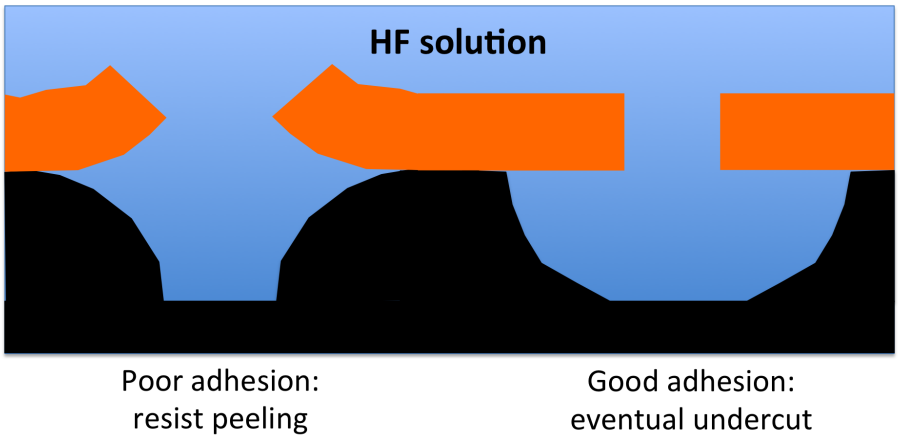

Figure 6.8: Effects of surface adhesion on etched feature geometry.

We were successfully able to employ our PLOMP 1.0 photoresist as an etch mask for concentrated HF, although a number of challenges remain. PLOMP dots 1 mm in diameter were patterned on a glass slide, by irradiating through a shadow mask at $\lambda = 254$ nm for 2 minutes. The measured height of the features was approximate 1 micron. After submerging the slides into concentrated HF for 1 minute, features approximately 30 microns tall were etched into the glass. The etch rate was so high

that it was difficult to tell the difference between lateral undercutting of the mask and diffusion through it. Attempts to extend this result to thermally-grown silica, a much denser oxide than the fused borosilicate glass used to make these substrates, proved challenging.

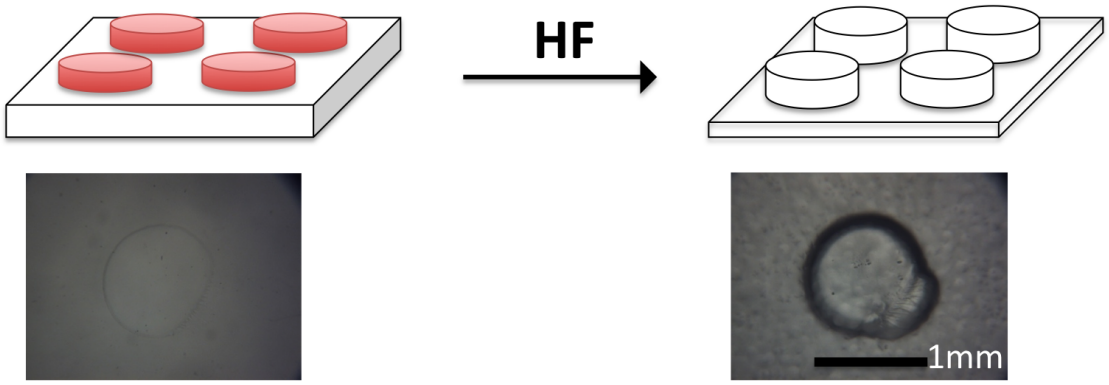

Figure 6.9: Results of etching silicate slides with concentrated HF (50%).

The ability to etch using unbuffered HF would enable the etch rates to be increased approximately 50-fold. This would potentially enable deeper oxide etching than previously possible, or higher throughput for currently accessible features. A number of considerations must be taken into account to move forward with this application, including the surface adhesion of the resist, the crosslinking density, accessible film thicknesses, and procedure for removing the resist after the etching process. We found that the PLOMP resists could typically be removed with piranha (sulfuric acid and hydrogen peroxide) solution after the etching process. While we have not yet developed this idea into a useful microfabrication process, in the future we hope to leverage the unique materials properties of our ROMP-based materials to solve this challenging engineering problem.

6.6 Peptide-Functional Surfaces toward Cell Scaffolds

Surface functionality plays an integral role in the biological recognition of synthetic materials. Cell adhesion and intracellular signaling are mediated by transmembrane receptors known as integrins. In vivo, integrins bind to proteins in the extracellular matrix, such as fibronectic.[7] The design of functional interfaces capable of interacting with integrins represents a key strategy in the development of robust methods for promoting cell growth on synthetic materials.[7–10] The short peptide sequence arginine - glycine - aspartic acid (RGD) has been identified as the minimal binding domain of fibronectin, which is necessary to recognize cell surface integrins. [11, 12] A wide variety of materials modified with RGD peptides have been employed to facilitate cell adhesion in a number of applications, including wound healing.[13–15]

We hoped to leverage the functional-group tolerance of PLOMP to enable the direct photopatterning of peptide-functionalized micro- and nanostructures, towards new materials capable of serving as cell scaffolds with unique properties and geometries. The norbornene-functionalized peptides, depicted in Figure 6.10, had already been synthesized in our group, as reported in Reference [16]. We collaborated with Tracy Clevenger and Dennis Clegg at UC Santa Barbara to test the viability of stem cells on our RGD-functionalized PLOMP films.

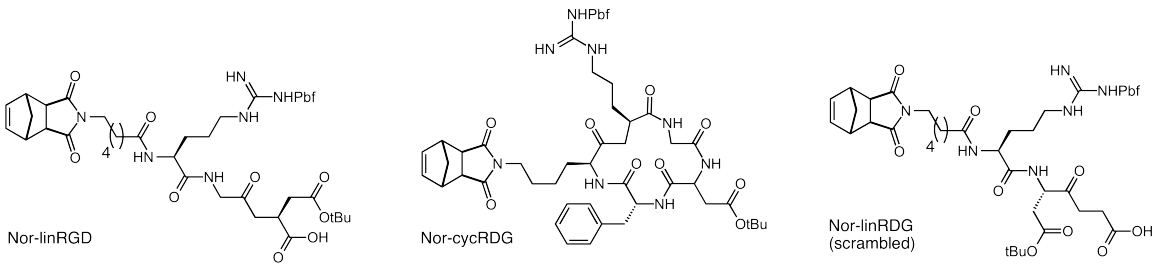

Figure 6.10: Structures of norbornene-functionalized peptides used to enhance cell growth on our PLOMP materials.

As a preliminary study to probe the ability of these peptide additives to modulate the biological compatibility of our PLOMP photoresists, we simply added these

peptide-functional monomers as dilute solutions in chloroform, with a target loading of 0.1 to 0.2 % by weight, to our PLOMP 1.0 photoresist. Crosslinked films of approximately 1 micron in thickness were achieved by spinning the resist onto a silicon substrate at 7000 RPM, irradiating the films at $\lambda = 254$ nm for 90 seconds, and developing the films in hexanes for 1-2 minutes. For these samples, the corner of each chip was masked as an internal control, both to validate the PLOMP process and for comparison of unintentional cell binding. These samples were shipped to UCSB to test stem cell adhesion and growth.

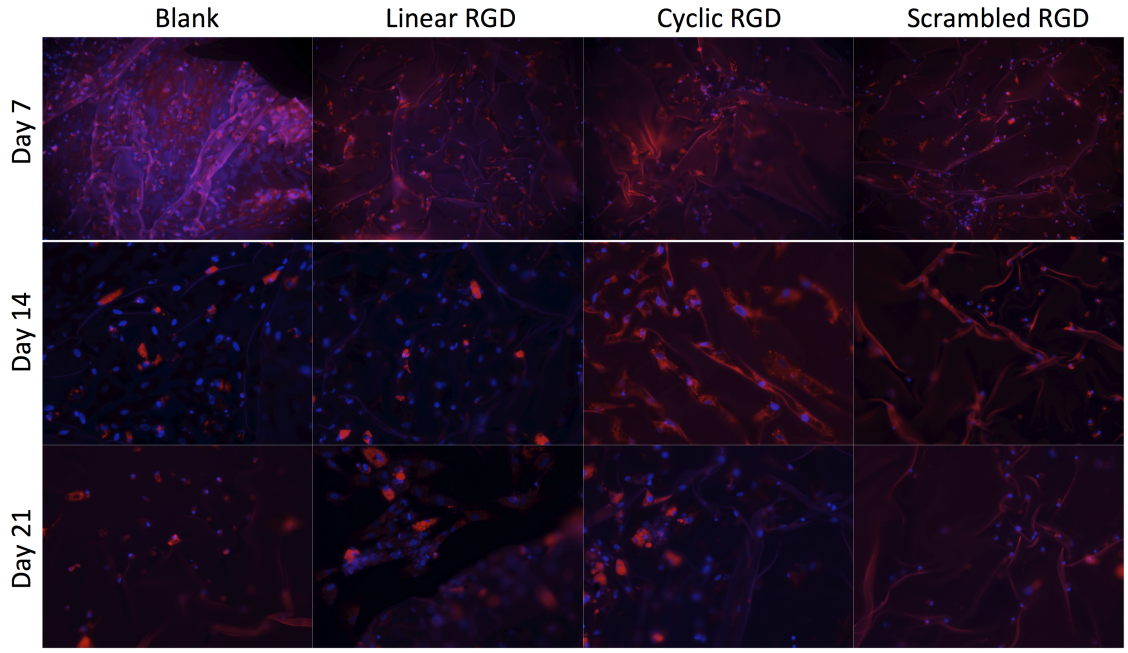

Figure 6.11: Results of a stem cell growth trial on RGD-functional PLOMP films. While there is evidence of adipogenic differentiation for our RGD-functionalized films, the improvement over the controls is not particularly stark. Red - LipidTOX. Blue - Hoescht

The use of the "scrambled" RDG negative control is to attempt to differentiate between changes in surface polarity and actual chemical recognition. These preliminary results do show growth and differentiation on our RGD-functionalized surfaces, but do not conclusively demonstrate a drastic improvement over the controls. Further studies will be required to probe the concentration dependence of the peptide on stem-cell growth. We hope to explore the effects of mechanical modulus and

microstructure geometry on stem-cell differentiation.

6.7 Nanoimprint Lithography via PLOMP

As mentioned in Chapter 4, nanoimprint lithography is a powerful technique for replicating 2D nanostructures. In our experiments to realize nanoimprint lithography of PLOMP resists, we utilized substrate conformal imprint lithography (SCIL).[17] Like other variations of nanoimprint lithography, the process starts by patterning a silicon master stamp using electron-beam lithography and etching. SEM images of the master stamp used in our experiments are shown in Figure 6.12. Most of our master stamps consisted of arrays of cylindrical pillars, with diameters and heights on the order of a few hundred nanometers.

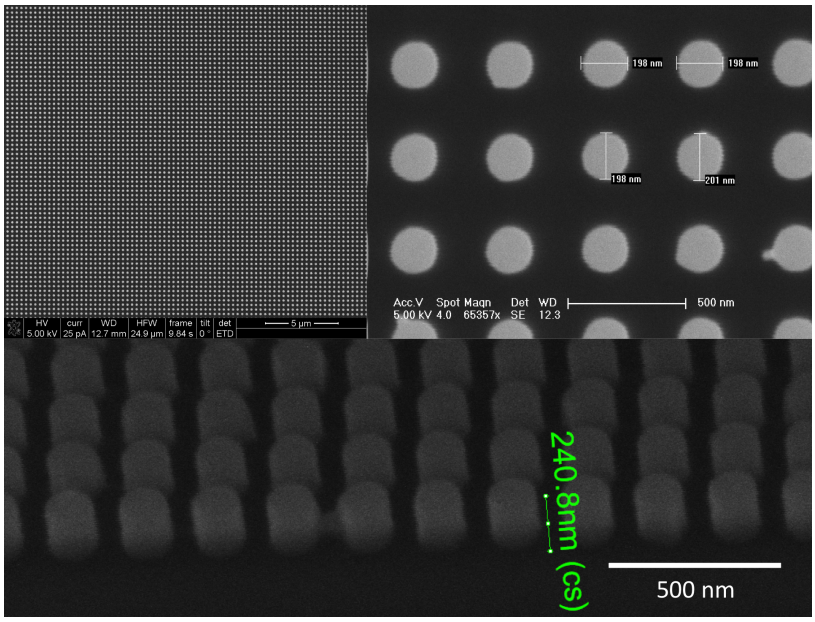

Figure 6.12: SEM images of our silicon master stamp for nanoimprint lithography reveal an array of cylindrical pillars.

Poly(dimethylsiloxane) (PDMS) stamps were cured using this silicon master as a mold, following the procedure in Refrence [17]. Verschuuren showed that in order to maintain the structural integrity of these nanoscale features, it was necessary to use a multilayer PDMS stamp.[17] The thin layer containing the features consists

of a high-modulus PDMS resin, referred to as X-PDMS, which contains additional crosslinking groups, inspired by chemistry developed by Whitesides.[18–20] The rest of the stamp is composed of a traditional PDMS resin, to provide flexibility (hence conformal) to the bulk of the stamp. Using this dual-modulus approach, Verschuuren was even able to imprint over defects on the wafer surface, such as unwanted pieces of particulate matter.

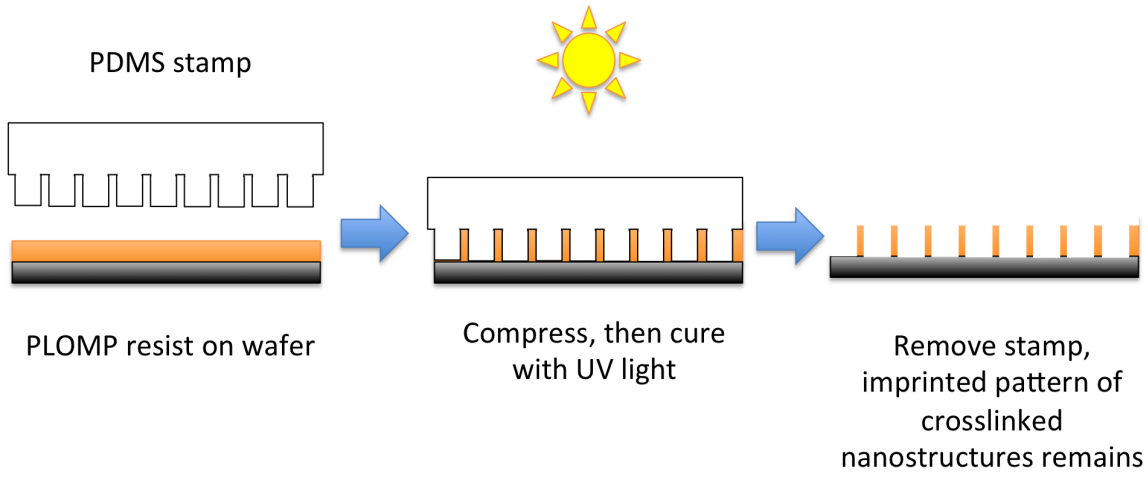

Figure 6.13: A schematic outline of nanoimprint lithography using PLOMP.

We were successfully able to use the SCIL process to demonstrate the feasibility of nanoimprinting our PLOMP resists. Thin films of our PLOMP 1.0 resist were cast onto silicon chips (1 x 1 cm) using a spin-coater, at 8000 RPM. To achieve thin films, it was necessary to dilute the published PLOMP 1.0 recipe with 50% ENBE to reduce the viscosity. The nanopatterned side of the PDMS stamp was brought into contact with the PLOMP resist, and the two sides were compressed together using binder clips. The films were exposed using a blacklight (360 nm) UV lamp, which illuminated the resist by transmitting through the PDMS stamp, for 20-30 minutes. After curing, the stamp was peeled away, leaving a nanopatterned crosslink polymer film on the surface.

In future work, we plan to extend this proof-of-principle to demonstrate imprinting of chemically functional nanostructures. For many of the applications we have discussed, nanoimprint lithography could provide an attractive route to high-throughput

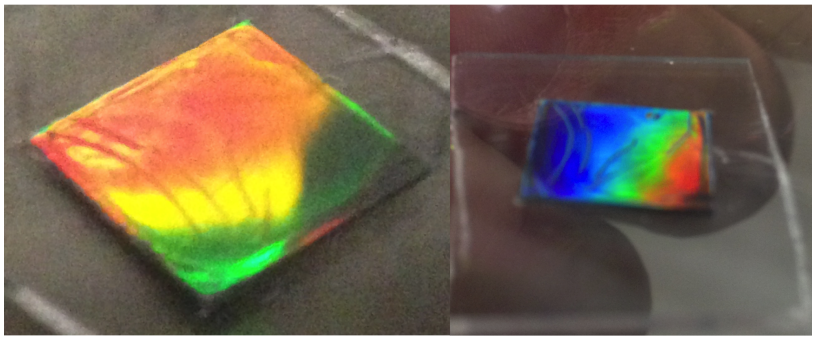

Figure 6.14: Photographs of nanoimprinted films via PLOMP. The diffractive colors from the nanopillar array provide evidence of successful pattern transfer.

patterning. For example, we may be able to utilize our developments towards HF-resistant materials here, to afford robust nanoimprintable etch masks. As well, we plan to explore the possibility of generating photonic crystals with surface-functional groups, which could be used as optically-read chemical sensors.

6.8 Electrocatalytic Films for Selective CO_2 Reduction

CO_2 is a linear and relatively unreactive molecule that has attracted attention in recent years as part of a renewable energy landscape through its conversion to chemical fuels. We propose that PLOMP can afford thin-films which simultaneously serve as cross-linked chemical barriers and functionalized catalytic scaffolds for the selective electrocatalytic reduction of CO_2. These films will tether activating agents and catalysts to the electrode surface, as well as protect the interface from unwanted side-reactions —specifically O_2 reduction. We plan to incorporate molecular pre-activators to alter the structure of the CO_2 molecule for selective access to high-value fuels via heterogeneous electroreduction of the pre-activated CO_2 at low overpotential.

In order to achieve the efficient conversion of CO_2 to chemical fuels, a catalyst is required to lower the activation energy of the chemical reduction. Many reaction pathways with comparable activation energies or shared reaction intermediates are generally accessible, leading to a variety of reaction products during heterogeneous

catalysis. For efficient photoelectrochemical CO_2 reduction, the catalyst needs to be able to readily receive electrons from the semiconductor substrate and protons from the electrolyte. Additionally, side reactions such as O_2 reduction and semiconductor degradation must be mitigated. We are working to leverage the versatility of the PLOMP platform to address the aforementioned challenges in photoelectrochemical CO_2 reduction. ROMP accessible materials have been demonstrated as functional supports, oxygen-barrier materials, and corrosion resistant materials, properties we hope to leverage in our design.

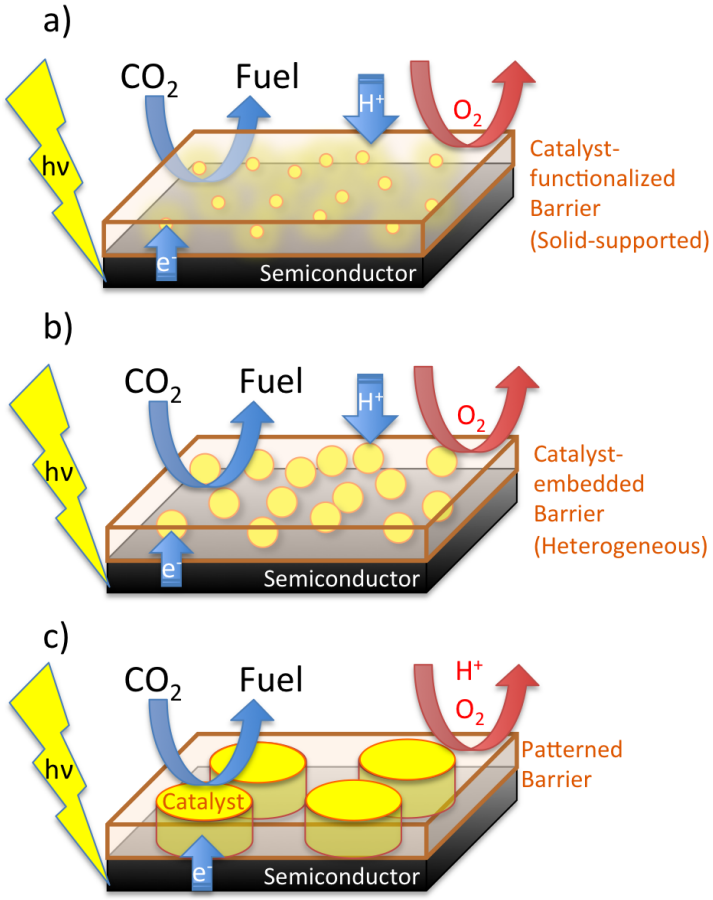

Figure 6.15: Three possible architectures for the electrocatalytic thin films, using (a) solid-supported small molecule catalysts, (b) embedded heterogeneous catalysts, such as nanoparticles, or (c) patterned catalytic domains surrounded by a protective barrier.

Although significant effort has been specifically centered around catalyst development for reducing dissolved CO_2, the present proposal aims to show that CO_2-bending

through formation of a molecular adduct not only increases local concentration of CO_2 prior to any catalytic transformation, but also moves the potential of the reduction of pre-activated substrate to more positive values. The capture and pre-bending of the substrate also allows electrode-driven CO_2 reduction to occur with high product selectivity, as we have demonstrated in our preliminary studies. We propose to take advantage of the functional group tolerance of PLOMP to tether both activating agents and catalysts to the electrode substrate.

We have demonstrated the applicability of our PLOMP process to thin-film electrochemical through a proof-of-principle study. Vinyl ferrocene was incorporated into thin-films of the cross-linked photoresist material on a glassy carbon electrode. The thin-films demonstrated reversible electrochemistry via cyclic voltammetry, even after the films had been soaked in a sulfuric acid solution overnight. This demonstrates the ability of the PLOMP process to tether catalysts to electrode surfaces and withstand the acidic conditions necessary for the CO_2RR. Currently, the conductivity of the films is too low for practical implementation, but we are confident that we can address this challenge via chemical functionalization.

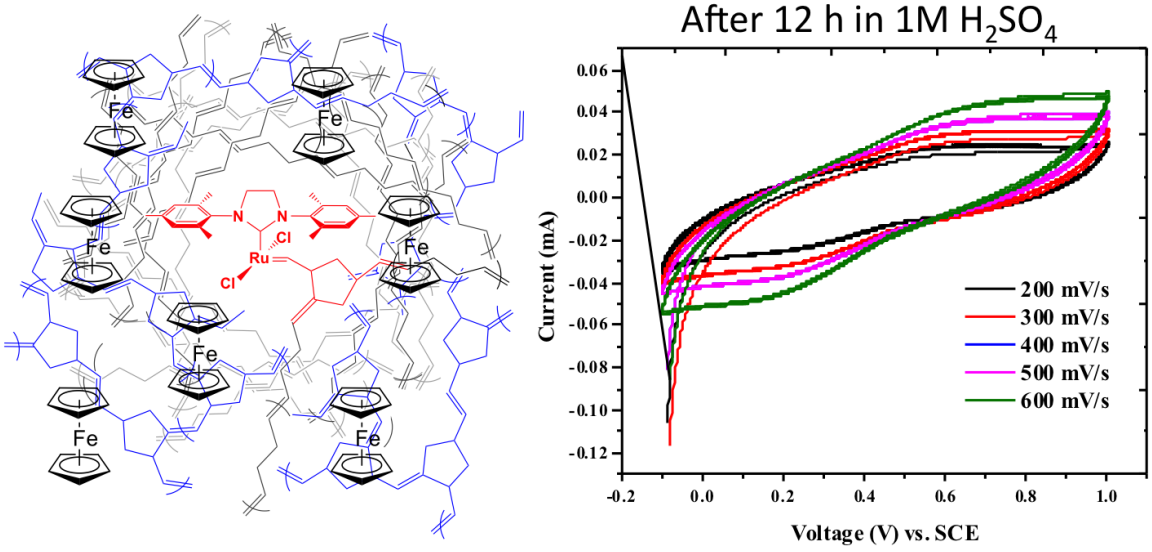

Figure 6.16: Cyclic voltammogram of a PLOMP film containing vinyl ferrocene.

As depicted in Figure 6.15, there are a variety of possible architectures for incorporation of the catalyst into the PLOMP photoresist. Our preliminary work with vinyl

ferrocene demonstrates the ability to incorporate molecular catalysts into the thin-film, as depicted in Figure Figure 6.15(a). Additionally, we believe that we will be able to incorporate heterogeneous nanoparticle catalysts into the films, as depicted in Figure 6.15(b). Finally, we propose an alternative geometry in which we photolithographically pattern our PLOMP barrier, with a catalytic surface comprising the remainder of the surface area. This final approach would perhaps enable more rapid incorporation of our strategy into existing JCAP testbeds. A combination of these approaches could also be explored. Preliminary electrochemical experiments will guide our decision of which architectures to pursue further.

6.9 Future Directions

There are many exciting possibilities to use photoactivated metathesis as a means of patterning materials with diverse functionality. We have been working towards a number of applications, each with their own unique challenges. While we have demonstrated the compatibility of a wide variety of molecular additives with the PLOMP process, we are currently working towards the development of a robust and modular process for patterning microstructures with chemically functional interfaces. As well, the applications that we have mentioned each require tailored materials properties, and optimization of the composition will be a necessary next step. Much of the work here would benefit from improved quantification of the key materials properties at play: viscosity, absorbance spectra, density of functional incorporation, and crosslinking kinetics. We hope that the lessons learned through these experiments will facilitate more controlled development in the future.

References

(1) Slugovc, C. *Macromolecular rapid communications* **2004**, *25*, 1283–1297.

(2) Hillmyer, M. A.; Grubbs, R. H. *Macromolecules* **1995**, *28*, 8662–8667.

(3) Matson, J. B.; Grubbs, R. H. *Macromolecules* **2008**, *41*, 5626–5631.

(4) Zirngast, M.; Pump, E.; Leitgeb, A.; Albering, J. H.; Slugovc, C. *Chemical Communications* **2011**, *47*, 2261.

(5) Ung, T.; Hejl, A.; Grubbs, R. H.; Schrodi, Y. *Organometallics* **2004**, *23*, 5399–5401.

(6) Nagarah, J. M.; Wagenaar, D. A. *Journal of Micromechanics and Microengineering* **2012**, *22*, 035011.

(7) Akiyama, S. K.; Olden, K.; Yamada, K. M. *Cancer and Metastasis Reviews* **1995**, *14*, 173–189.

(8) Hersel, U.; Dahmen, C.; Kessler, H. *Biomaterials* **2003**, *24*, 4385–4415.

(9) Sakiyama-Elbert, S. E.; Hubbell, J. A. *Annual Review of Materials Research* **2001**, *31*, 183–201.

(10) Langer, R. *Accounts of Chemical Research* **2000**, *33*, 94–101.

(11) Pierschbacher, M. D.; Ruoslahti, E. *Nature* **1984**, 30–3.

(12) Xiong, J.-P.; Stehle, T.; Zhang, R.; Joachimiak, A.; Frech, M.; Goodman, S. L.; Arnaout, M. A. *Science* **2002**, *296*, 151–155.

(13) Pettit, D. K.; Hoffman, A. S.; Horbett, T. A. *Journal of biomedical materials research* **1994**, *28*, 685–691.

(14) Aucoin, L.; Griffith, C. M.; Pleizier, G.; Deslandes, Y.; Sheardown, H. *Journal of Biomaterials Science, Polymer Edition* **2002**, *13*, 447–462.

(15) Verrier, S.; Pallu, S.; Bareille, R.; Jonczyk, A.; Meyer, J.; Dard, M.; Amedee, J. *Biomaterials* **2002**, *23*, 585–596.

(16) Patel, P. R.; Kiser, R. C.; Lu, Y. Y.; Fong, E.; Ho, W. C.; Tirrell, D. A.; Grubbs, R. H. *Biomacromolecules* **2012**, *13*, 2546–2553.

(17) Verschuuren, M. A. *PhD Thesis* **2010**.

(18) Odom, T. W.; Love, J. C.; Wolfe, D. B.; Paul, K. E.; Whitesides, G. M. *Langmuir* **2002**, *18*, 5314–5320.

(19) Odom, T. W.; Thalladi, V. R.; Love, J. C.; Whitesides, G. M. *Journal of the American Chemical Society* **2002**, *124*, 12112–12113.

(20) Qin, D.; Xia, Y.; Whitesides, G. M. *Nature protocols* **2010**, *5*, 491–502.

Chapter 7

Direct Writing 3D Nanostructures via Multiphoton Lithography

Portions adapted with permission from Mandsberg, N. K.; Weitekamp, R. A.; Atwater, H. A. "Direct-Write of Chemically Functional Nanostructures". *SURF Final Report* **2014**.

Chapter Abstract

Multiphoton absorption provides a means of directly writing solid nanostructures with feature dimensions below the diffraction limit. While the hardware and software required to perform multiphoton lithography is commercially available, there are a limited number of photocurable resins that have been employed. This chapter details our efforts towards multiphoton lithography of PLOMP resists. Our goal is to develop a toolbox for the direct-write lithography of a variety of functional nanostructures, with applications in nanophotonics, bioengineering, nanomechanics, and microelectronics.

7.1 2-photon Absorption

Multiphoton absorption was predicted by Maria Göppert-Mayer in 1931 [1], but it was not until after the invention of the laser that applications of this phenomenon were developed. This is because multiphoton excitations are very rare events, and intense artificial light sources needed to be developed in order to observe them. To put the probability in perspective, at the optical intensity of sunlight, two photon-absorption will occur once every 10 million years for a strong two-photon absorber such as Rhodamine B.[2] In this example, the single photon excitation would occur every second.

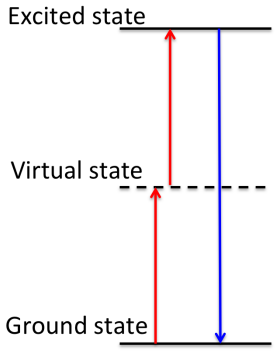

Figure 7.1: Two photons are absorbed to a high energy excited state, which can emit a photon with double the energy.

Today, two-photon excitations are typically induced using pulsed lasers, which are preferable to continuous sources because they can achieve very high peak optical intensities at drastically lower power. Additionally, the light is is typically focused to a diffraction-limited beam spot using a high numerical aperture lens. The rate of two-photon excitation is proportional to the intensity squared, and the intensity of a focused beam falls by the square of the distance from the focal plane. Putting these together, the two-photon excitation falls off as the fourth power of the distance from the focal plane, enabling precision exitation and sub-diffration limited resolution.[3]

The same principles apply to other multiphoton processes —for patterning applications we will simply refer to multiphoton lithography, as higher-order absorption events can also contribute to chemical activation. In lithographic applications, it can

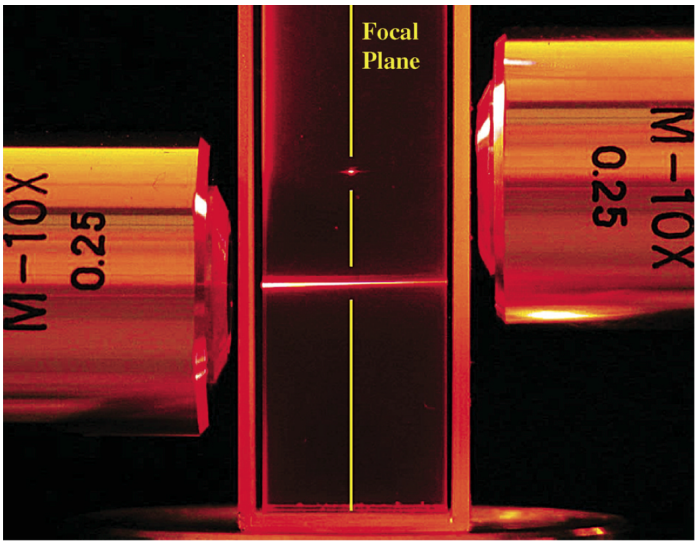

Figure 7.2: Visualization of localized two-photon excitation. The top spot is the result of emission from 2-photon absorption, whereas the bottom reveals the entire excitation path in the case of single photon excitation. Image from Reference [3]

be difficult to decouple the contributions of 2- vs. 3-photon absorption. While the probability of higher-order absorption events is significantly lower, the absorption cross-section and kinetics of the resulting chemistry is often dramatically different than the 2-photon pathway.

7.2 Direct Laser Writing

While there are a number of examples of diffractive and holographic approaches to multiphoton lithography of periodic structures, we will focus here on direct laser writing (DLW) using multiphoton absorption. There are various manifestations of direct writing, using both linear and non-linear absorption, which actuate via ablation, localized heating, chemical crosslinking, or bond cleavage.[3] In each of these applications, the focal point of a laser beam is rastered in a "spot-by-spot" fashion within the photosensitive medium. A key advantage of multiphoton DLW is the ability to localize the chemical activation to a sub-diffraction limited spot size. In practice, this enables two useful features. First is the ability to pattern materials at a resolution of approximately 100 nm. Secondly, because only the focal point of the

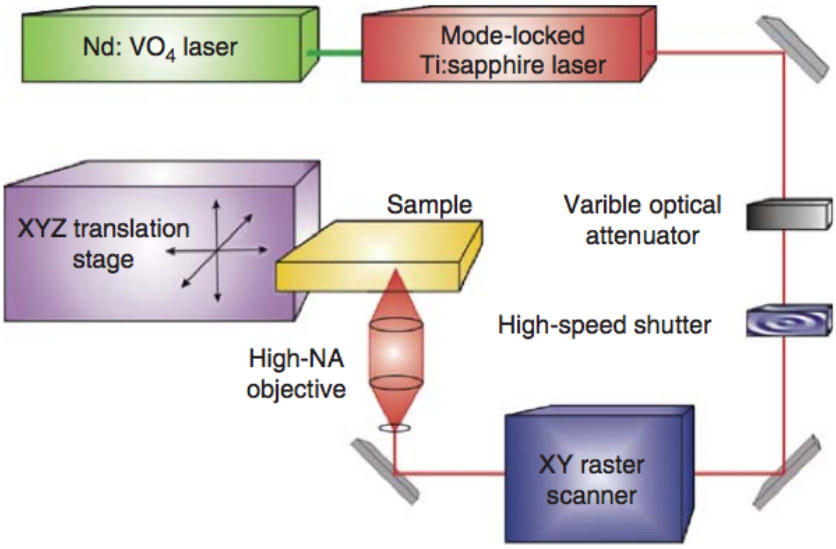

Figure 7.3: Schematic of a DLW apparatus. A pulsed infrared laser is focused onto the sample surface. Rastering can be achieved through a combination of beam and sample movement. Image from Reference [4]

laser has an intensity high enough to achieve multiphoton excitation, highly complex geometries can be written into the entire volume of resist. By contrast, SLA writing is necessarily divided into thin planes using various engineering approaches to re-flow active resin into that plane, as the laser would otherwise "write" everything along its beam path.

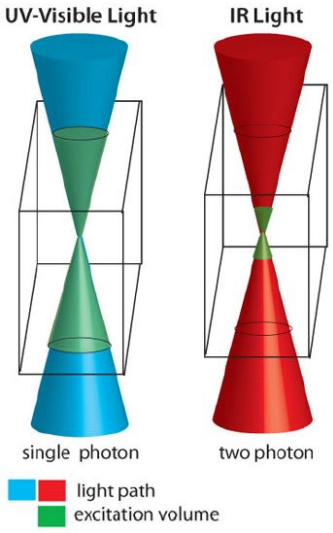

Figure 7.4: 1- vs. 2-photon excitation volumes. Image from Nanoscribe.

In our work, we have employed the Photonic Professional multiphoton lithography

system, manufactured by Nanoscribe (hereafter referred to as a Nanoscribe). The Nanoscribe utilizes a pulsed femtosecond Ti:sapphire laser with a wavelength of 780 nm, concentrated through a 100x, nA = 1.4 objective lens. The practical resolution of the Nanoscribe system is approximately 150 x 150 x 800 nm (x,y,z). The resists sold by Nanoscribe for this instrument utilize photoradical crosslinking of multifunctional acrylates. As a result, these crosslinked acrylates are typically limited to serving the role of a structural placeholder for the desired material functionality.

7.3 Early Attempts

Our initial experimental setup was to simply use the PLOMP 1.0 resist (described in Chapter 5) in the Nanoscribe. The results of these experiments were highly inconsistent; the response of the resist to exposure varied from exothermic explosions to boiling to completely unreactive. Figure 7.5 exemplifies some of these inconsistencies, one can clearly see bubble formation around the written line as well as regions of variable linewidth.

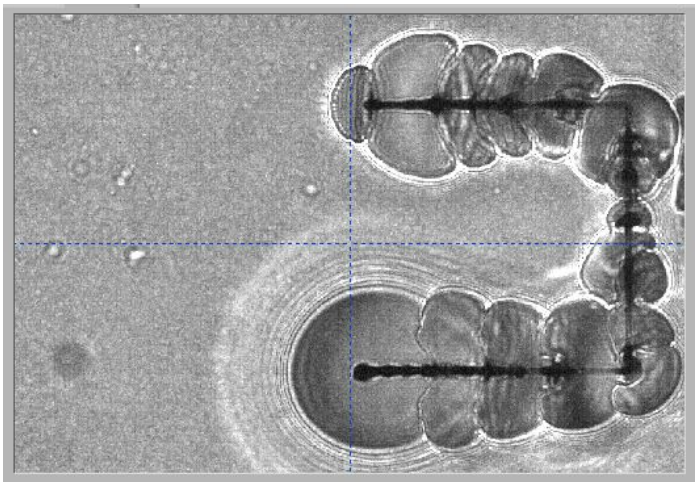

Figure 7.5: An early attempt at 2-photon PLOMP, depicting the issues of boiling and non-linear writing kinetics.

As mentioned in Chapter 5, while the parent resist was stable under ambient conditions for many months as a viscous solution, cast films were not stable to air indefinitely. Practically, it was necessary to begin irradiation of the films a few minutes

after casting to achieve consistent results. Because of the time required to prepare, load and align samples into the Nanoscribe, we observed dramatically varied outcomes depending on the delay between initial air exposure of the resist during sample preparation and writing. Within the first hour, writing was generally consistent, but rapidly declined afterwards. Much of the inspiration to find a more stable photocatalyst came from these initial attempts on the Nanoscribe.

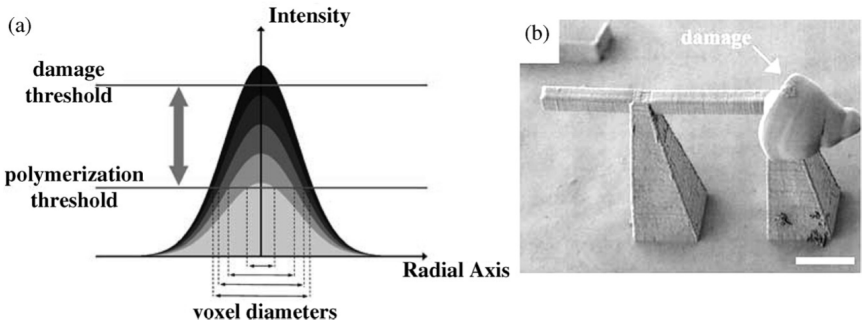

Figure 7.6: (a) The intensity-dependent behavior of DLW resists typically exhibits two thresholds: polymerization and damage. (b) Damage due to overirradiation appears as a solidified explosion as reagents vaporize, expand, and crosslink. Image from Reference [3].

Baldacinni describes the writing resolution and kinetics as a function of intensity, with two key thresholds: polymerization and damage. Figure 7.6 depicts the chemical response as a function of optical intensity, and shows an example of a structure where the damage threshold was clearly exceeded. Most of these heuristics have been developed in the context of radical polymerization. One contributing factor to the polymerization threshold phenomenon is the inhibition of the radical polymerization by oxygen from the environment. In principle, the polymerization threshold for PLOMP could be much lower, as ROMP is exothermic and the resin could be designed to rapidly initiate after activation. The downside of this scenario is that the resolution and feature shape will be impacted by diffusion. For the purposes of writing high-fidelity structures, it is therefore more desirable to control the kinetics of ROMP, either through ligand coordination or re-quenching via excess vinyl ether addition.

7.4 Control Experiments

There are a number of key differences between the physical and chemical environments of the resist in the Nanoscribe, compared to a UV-cured thin-film. First, the optical intensity is dramatically higher and focused only at the writing point. The optical flux in the Nanoscribe is approximately 5×10^8 times higher than the UV lamp employed in our thin-film studies in the previous chapters. Second, the extremely short lengthscales of the written structures demand very high mechanical contrast between the written and unwritten domains, in order to successfully isolate the free-standing nanostructures. Thus, it is desirable to achieve a system with a low viscosity before curing, that will rapidly crosslink to a high-modulus solid. At the same time, the high optical power of the laser combined with the exothermic nature of ROMP can cause the low molecular weight components to vaporize during the writing process, which results in bubbling and changes the local composition of the resist. For these reasons, we typically avoided including excess solvent in developing resist compositions for 2-photon lithography. Finally, the Nanoscribe features the ability to monitor the writing process in real time through the same 100x objective lens that the laser is focused through. The sample is illuminated by an infrared LED (835 nm), enabling the structures to be imaged due to refractive index contrast after crosslinking. While this has the advantage of providing a rapid means for prototyping the write conditions in real-time, it provides limited information about the chemical activity within the resist.

We identified 5-norbornene-2-methanol as a relatively high-boiling ROMP monomer, which is also a liquid at room temperature. During our attempts to incorporate this monomer into the PLOMP resist, we discovered that this monomer was photoactive, even in the absence of any ruthenium catalyst. Alcohols are well-known to undergo photo-dissociation into radical fragments.[5] The addition of the common radical inhibitor BHT (2,6-Di-tert-butyl-4-methylphenol) to the monomer dramatically changed the writing behavior. While BHT prevented the writing of 3D structures, it is interesting to note that the base of the structure is still visible. It is unclear

whether this is the result of chemical interaction with the silica substrate, or simply due to the fact that the local concentration of BHT is too low at the interface to effectively mitigate the radical crosslinking. Nevertheless, this unique behavior at the interface provides some potential challenges to utilizing a single, well-defined writing mechanism.

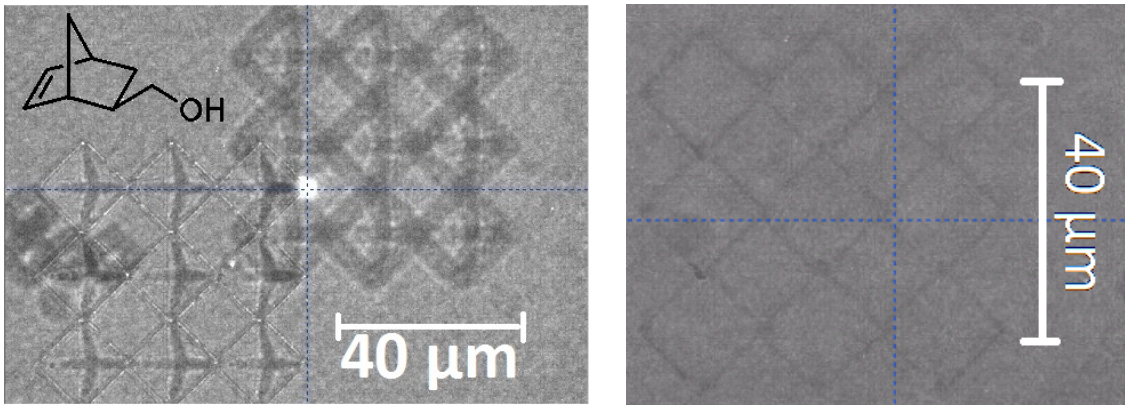

Figure 7.7: (Left) 5-norbornene-2-methanol is able to undergo visible writing on its own, without any added catalyst. (Right) The addition of the radical inhibitor BHT to this molecule shuts down writing in the bulk, while some surface activity remains.

These control experiments clearly indicate the presence of competing radical processes in this highly intense optical environment. Radical formation within the resist presents a number of challenges to PLOMP. First, the radical polymerization of olefins will consume the necessary reactants, reducing the concentration of ROMPable monomers. Secondly, the radical species could alter the structure of the ruthenium catalysts, there is precedent for these complexes to also catalyze radical polymerizations.[6–8] After these experiments were conducted, we began to add BHT to all of our resists to mitigate competing radical processes.

As mentioned above, another challenge to developing a robust multiphoton PLOMP process was the evaporation of volatile components during the writing process. Depending on the resist composition, ∼10-50 fold reductions in the volume of resist were observed after the writing process. For PLOMP 1.0 resists, the ethylidene norbornene is the most volatile component, with a boiling point of 146 °C. This is significantly lower than the commercially-available (photoradically cured) pentaery-

thritol triacrylate, with a boiling point of 205 °C. The total resist droplet size is typically only ∼100-300 μL. The combination of the high surface area and heating from the laser and illumination sources likely accelerate the evaporation rate. To our surprise, the PLOMP 2.0 resists also exhibited significant shrinkage after the writing process. These resists are prepared by the partial polymerization of DCPD, which is quenched when the reaction mixture reaches the desired viscosity. We assumed that these highly viscous resists consisted largely of oligomeric poly(DCPD), which is inconsistent with the observed evaporation. After concentrating a typical PLOMP 2.0 resist at 50 millitorr overnight, the remaining solids only accounted for ∼15% of the mass of the resist. This suggests that there is a significant amount of unreacted DCPD remaining in the PLOMP 2.0 resists. We attempted to engineer a number of solutions to mitigate the effects of evaporation during writing.

7.5 Multiphoton PLOMP Results

Using the "DeScribe" software package, a variety of 3D microstructures were designed to explore multiphoton PLOMP. We are greatly indebted to the Greer group, specifically Lucas Meza and Lauren Montemayor, for helping us with our initial structure designs. Two types of programmed structures that shall be used as continuous references are the octahedron-based lattice structure as well as the Archimedean spire (Figure 7.8).

A number of methods for mitigating the effects of monomer evaporation were tested. One of the simplest attempts is shown in Figure 7.9, a coverslip was placed over the top of the sample holder to limited evaporation. Unfortunately, in many cases this simply let to condensation of the volatile components on the top coverslip, further complicating the writing process.

We also attempted to pre-bake some of the PLOMP films, in an attempt to remove the most volatile components before the writing process began. While this was an effective strategy for the thin-film patterning of PLOMP 2.0 resists in Chapter 6, it led to many processing complications in the DLW process. As mentioned above,

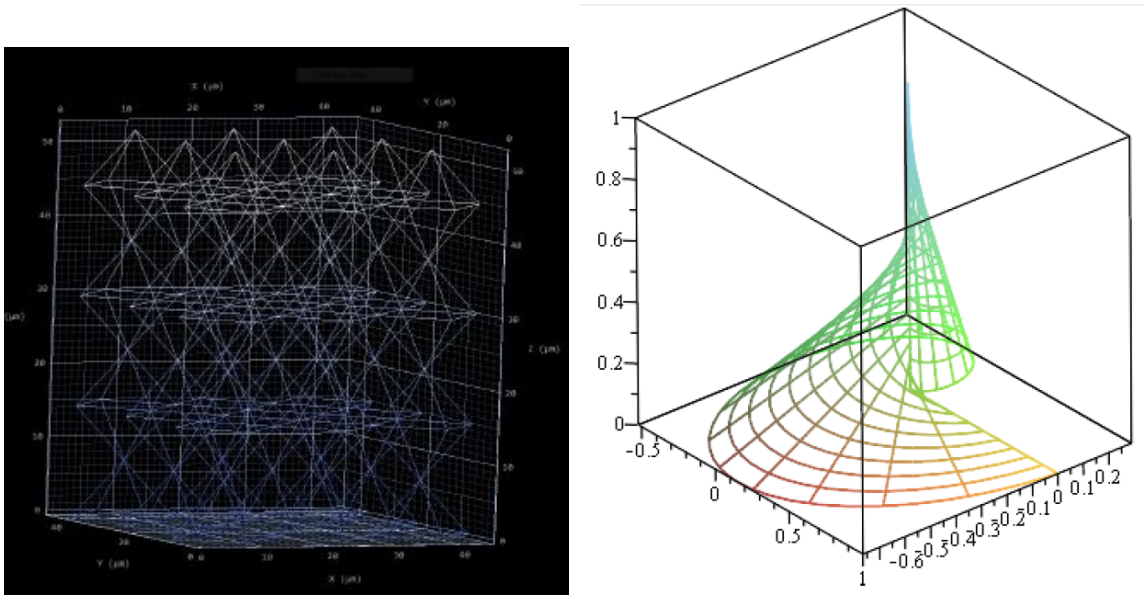

Figure 7.8: Computer generated 3D models for DLW. (Left) Octahedron lattice, and (Right) an Archimedean spire.

Figure 7.9: An attempt to saturate the local atmosphere with volatile resist components.

Figure 7.10: While many of the PLOMP resists were stable to heating, this picture clearly shows the entire volume of resist has crosslinked into a continuous gel by the time the writing process is finished.

one of the biggest challenges to effectively developing these resists into free-standing nanostructures is the high viscosity of the starting photoresist. The potential for partial crosslinking during the resist synthesis renders the possibility of network entanglement, which could be contributing to these observations. Figure 7.10 depicts an attempt to develop a pre-heated resist after the writing process.

Another approach to removing volatile components was to slowly dry the films under a stream of argon. To maintain a thick film, an HPLC vial cap was inverted and used as a corrall, as depicted in Figure 8.3. While this process was somewhat time-consuming, it did enable relatively thick semi-solid films to be isolated, in which we were able to write 3D nanostructures.

Figure 7.11 depicts a 3D octahedral microlattice structure, imaged through confocal microscope of the instrument at various focal planes. This specific sample utlized a variant of the PLOMP resist in which the DCPD was copolymerized with an equal volume of COD. The details of the synthetic preparation can be found in Section 8.4, and we have termed this variant PLOMP 2.1. In terms of the fidelity of the writing throughout the 3D volume, this is perhaps the best result that we have obtained thus

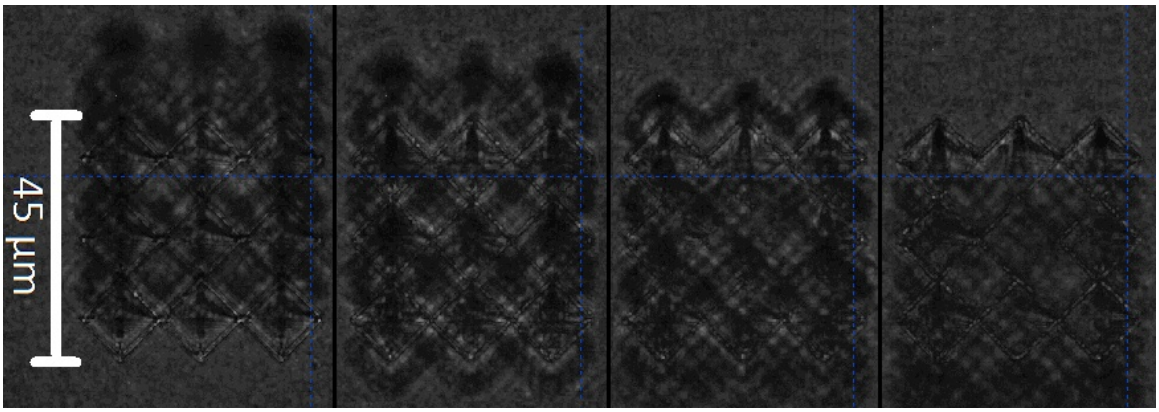

Figure 7.11: 3D microlattices from a gradually evaporated PLOMP 2.1 resist, as imaged on the Nanoscribe at various focal planes.

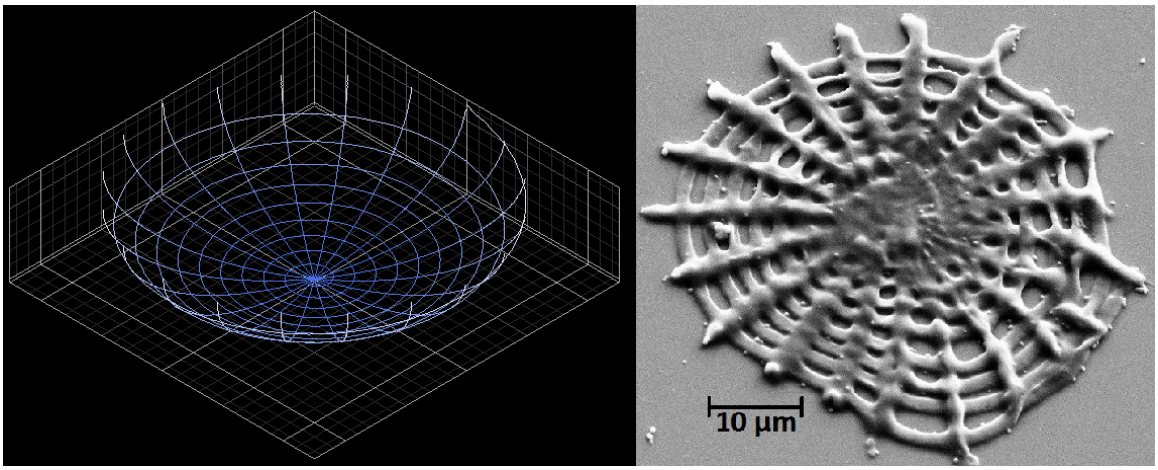

Figure 7.12: A collapsed basket structure, after development of the written PLOMP 2.1 resist.

far. Despite this success, it has been difficult to reliably reproduce this same level of quality.

With the ability to now write 3D structures into our PLOMP resists, we sought to find the right developing conditions to dissolve away the unirradiated regions without distorting the written structure. As mentioned before, one of the difficulties present in our system is the possibility of network entanglment, effectively linking the unexposed and exposed regions of the material. The possibility of crosslinks in the unirradiated phase, as well as the high viscosity of the material regardless of the network connectivity, can generate significant sheering forces when the material is suddendly solvated, and high surface tension as the material dries.

We had minimal success in our attempts to isolate free-standing nanostructures. Figure 7.12 shows a nanostructure that was successfully developed by submerging the film in toluene, but collapsed at some point during the process. For this sample, it is quite likely that the modulus of the written structure was simply not high enough to support itself. One possible approach to overcome our development issues for these samples is critical-point drying, which we have yet to explore.

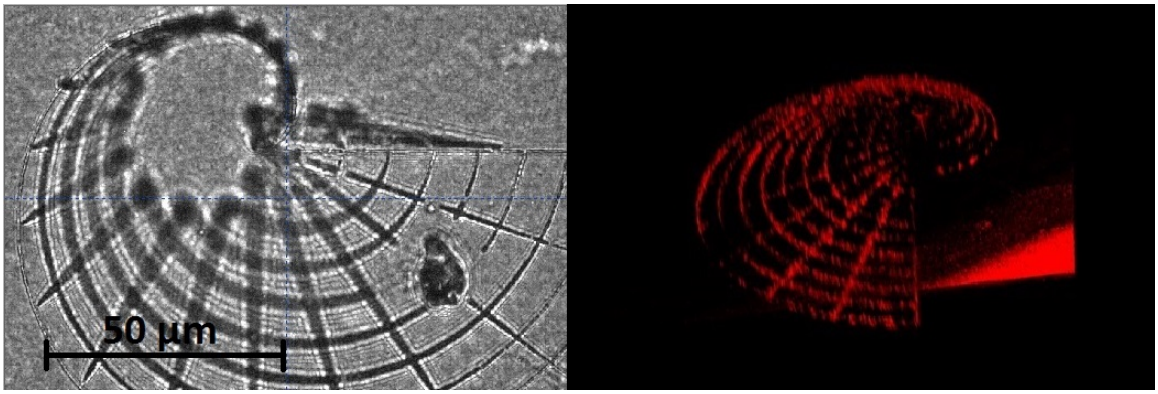

Figure 7.13: Confocal image of after DLW of an undeveloped PLOMP 2.1 resist, with added BHT and β-carotene

As well, we made a few attempts to incorporate functionality into the multiphoton PLOMP DLW. We had hoped that the incorporation of luminescent molecular dyes into our material might facilitate imaging. Figure 7.13 shows a confocal microscopy image of an undeveloped microstructure, with β-carotene embedded into the resist. Once a standard set of conditions can be found to successfully perform multiphoton PLOMP DLW, we hope to extend our efforts to afford chemically functional nanostructures.

7.6 Remaining Challenges

One of the biggest challenges in this project has been the drastically different response of the material at the glass/photoresist interface versus the bulk of the film. In the vast majority of our attempts, high-fidelity structures can be written in 2D at the interface, but 3D writing did not occur reliably. Figure 7.14 shows the inconsistency between writing at various heights above the glass/resist interface. Closer to the interface, the material is apparently much more reactive, as the higher intensities resulted in "explosions" within the material. Further away, the visible feature are much more linear, and less dependent on the optical power.

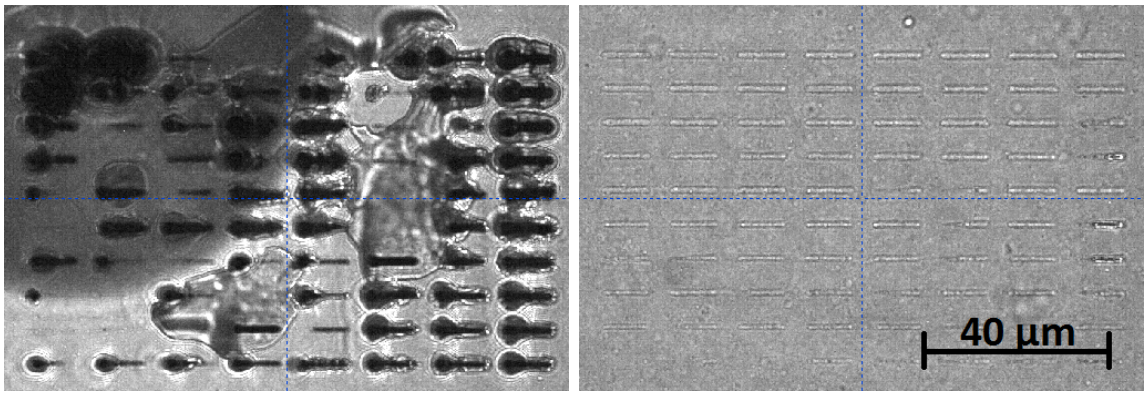

Figure 7.14: Each of these images depicts an array of lines written at iteratively increased powers. On the left, the sweep was performed 2 microns above the detected glass/resist interface, while on the right it was written 5 microns above. The height-dependence of the material response is drastic.

Figure 7.15 depicts how drastic the surface reactivity can be, where the original line "written" is effectively hollow, surrounded by crosslinked material, apparently after a significant expansion. It is possible that photoradical chemistry could be contributing to theses observations. As shown in Figure 7.7, even the addition of radical inhibitors did not fully mitigate activity at the glass/resist interface. While norbornene is not typically considered to be a very reactive monomer for radical polymerization, the vinyl ethers present in the material are known as rapid radical crosslinkers, and may be contributing to this highly non-linear writing behavior.

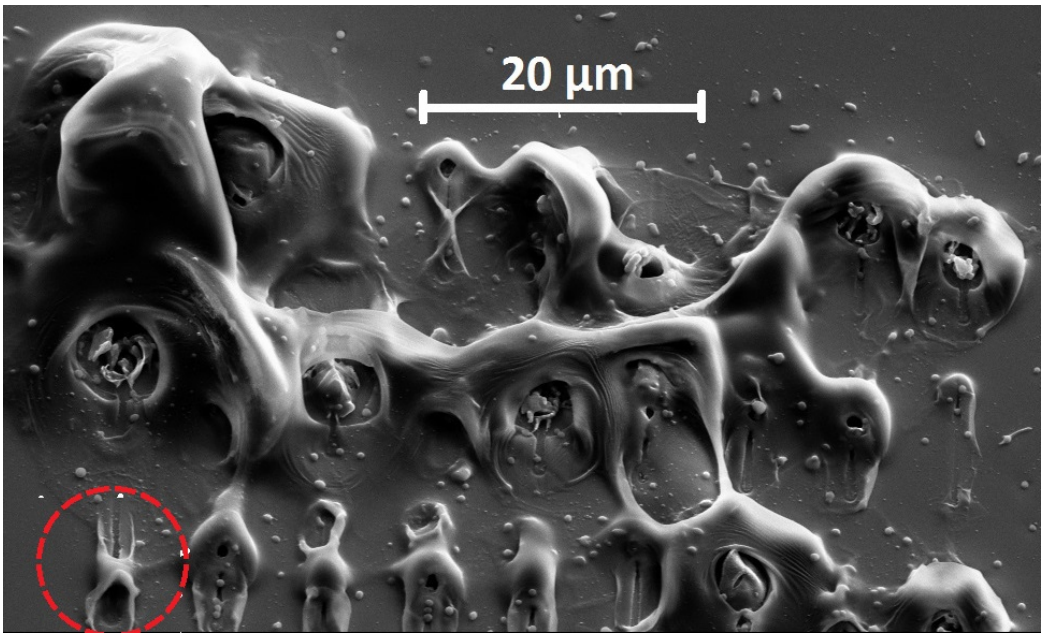

Figure 7.15: SEM micrograph of PLOMP DLW, revealing highly non-linear writing behavior.

7.7 Conclusions

We have demonstrated the ability to write 3D nanostructures using our PLOMP resists, via multiphoton direct laser writing. The development of reliable conditions required the improved precatalyst stability mentioned in the previous chapter, methods for mitigating the kinetics of this highly exothermic reaction and careful preparation of the material composition. A robust process to yield free-standing PLOMP nanostructures remains elusive, and we are working towards new approaches which may be able to surmount these challenges. We believe that the synthesis of a multifunctional ROMP monomer that is both high-boiling yet also a liquid at room temperature will greatly facilitate this endeavor. The mechanical contrast between the starting and written materials likely needs to be improved, as most of the commercially-available resists for DLW involve a transition from a liquid to a high modulus solid.

References

(1) Göppert-Mayer, M. *Annalen der Physik* **1931**, *401*, 273–294.

(2) Denk, W.; Svoboda, K. *Neuron* **1997**, *18*, 351–357.

(3) Baldacchini, T. *Generating Micro-and Nanopatterns on Polymeric Materials* **2011**, 107–140.

(4) Marder, S. R.; Brédas, J.-L.; Perry, J. W. *MRS Bulletin* **2007**, *32*, 561–565.

(5) Turro, N. J., *Modern molecular photochemistry*; University Science Books: 1991.

(6) Bielawski, C. W.; Morita, T.; Grubbs, R. H. *Macromolecules* **2000**, *33*, 678–680.

(7) Simal, F.; Demonceau, A.; Noels, A. F. *Tetrahedron letters* **1999**, *40*, 5689–5693.

(8) Simal, F.; Demonceau, A.; Noels, A. F. *Angewandte Chemie International Edition* **1999**, *38*, 538–540.

Part III

Appendices

Chapter 8

Additional Experimental Detail

8.1 Detailed Procedures for Chapter 2

Detailed synthetic procedures can be found in References [1–5].

Reflection Measurements

Reflection measurements were performed on a Cary 5000 UV/Vis/NIR spectrophotometer, equipped with an integrating sphere diffuse reflectance accessory (Internal DRA 1800). All measurements were referenced to a LabSphere Spectralon 99% certified reflectance standard. The samples were illuminated through a Spectralon-coated aperature with a diameter of 1 cm, with a beam area of approximately 0.5 cm^2. The samples were scanned at a rate of 600 nm/min, with a 1 nm data interval, from 1800 to 200 nm, with a detector crossover (InGaAs to PMT) at either 800 or 875 nm.

Transfer Matrix Method Optical Modeling

Transfer matrix simulations were built upon the EWA MATLAB package by Orfanidis (`http://www.ece.rutgers.edu/~orfanidi/ewa`), specifically the multidiel1() function. The refractive indices were measured by first synthesizing homopolymers of L-MM (M) and S-MM (N), spin casting thin films ($\sim$ 50 nm) onto a Si wafer, and solving for the thicknesses and indices by fitting a Cauchy model to spectroscopic ellipsometric measurements at 70°. The thicknesses were verified with an AFM scratch test. The refractive indices are very close to reported published values of bulk polylactide (PLA) and polystyrene (PS) (`http://refractiveindex.info`). The refractive indices as a function of wavelength, averaged over five different ellipsometric measurements, were employed in the simulations (Cauchy parameters provide below). The extinction coefficients were not consistently fit by ellipsometry. Instead, the extinction coefficients were calculated from the measured absorption of spin cast thin films on quartz, using a Cary 50 UV/Vis spectrophotometer. Exponential fits of the extinction coefficients were used in the simulations (equations provided below). The numbers of alternating layers in the simulations were guessed from the SEM cross section of the corresponding films. The volume fractions of each polymer were guessed by assuming an equal density for each block, and using the weight ratios calculated by NMR (described elsewhere). The actual density of each block in the film is not

easily measured, and we justify the assumption of equal density by the argument that the processing conditions and brush architecture of the polymers (which are identical for every case) will largely dictate the density, rendering literature values of bulk PLA and PS irrelevant.

Cauchy Parameters	PLA	PS
n_0	1.4509	1.5642
n_1	37.0849	42.8081
n_2	-3.4587	-1.7057

$$n = n_0 + \frac{n_1 \times 10^2}{\lambda^2} + \frac{n_2 \times 10^7}{\lambda^4}$$

$$k_{PS} = 6040.3\, exp(-0.05\lambda) \qquad k_{PLA} = 1000000\, exp(-0.088\lambda)$$

$$200 \text{ nm} < \lambda < 1800 \text{ nm}$$

The inputs to our script are: the frequency dependent complex refractive indices, measured first order peak of maximum reflectance, approximate number of layers by SEM, and the weight fractions of each block by NMR. An initial guess of the size of each block domain was made using the first order peak of reflection, using the equation $\lambda_{max} = 2(n_1x_1 + n_2x_2)$, assuming equal polymer densities. This initial domain size is perturbed by a normally distributed variance, with the coefficient of variation as a free parameter. To account for the loss of coherence due to layer roughness, the calculated phase change in the transfer matrix simulation was perturbed by a normally distributed variance, with the standard deviation as a second free parameter. For each sample, a total of 1000 simulations were run and averaged to remove noise. The plots in the figures were additionally smoothed using FFT smoothing with a factor of 3.

8.2 Detailed Procedures for Chapter 3

Fabrication

Silica spheres of 700 nm diameter were obtained from Polysciences Inc. as a 10% (by weight) suspension in water. This suspension was filtered on a fine filtration frit, rinsed with tetrahydrofuran and acetone. The solids were washed with 10 mL of 1:1 methanol/HCl, and rinsed again with acetone. The mostly dried powder was then heated in an oven for 5 minutes at 110 °C and dried under vacuum overnight. To 25 mL toluene in a 50 mL round-bottomed flask, 786 mg of dry silica spheres were suspended and stirred. To this suspension was added 1 mL 3-aminopropyl(diethoxy)methyl silane. The suspension was stirred 72 hours, filtered on a fine fritted filter, rinsed with toluene, and dried *in vacuo* to yield 756 mg dry, amine-functionalized silica spheres.

A 1% (by weight) suspension for Langmuir-Blodgett deposition was prepared by suspending 235 mg of functionalized silica spheres in a solution of 4 mL ethanol and 17 mL methylene chloride. We first perform an isotherm measurement where we record the surface pressure of the water as a function of the surface area, which is reduced using the compression barriers of the LB trough. When the area of the trough is large, the surface pressure of the water is around 4 mN/m. The spheres are freely spread on the surface of the water. This is the so-called "gaseous" state. While the LB troughs barriers compress the spheres and reduce the area that the spheres stand on, the surface pressure slowly increases until 5 mN/m. The slope abruptly increases until 10 mN/m. This is the "liquid" state, corresponding to a dense and condensed monolayer of hexagonally close packed spheres at the surface of the water. Upon further compression, the slope of the curve decreases and the monolayer collapses into multilayer structures. For our purpose, the optimal point is at the middle of the "liquid" condensed state where the spheres are well close packed and still form a monolayer. This point is reached when the surface pressure is around 7.5 mN/m. In a second step, knowing the optimal surface pressure for the deposition, we perform a dipping experiment. While the spheres are on the surface of the water

in the "gaseous" state, we immerse the substrate into the LB trough. We then close the LBs barriers until the surface pressure reaches 7.5 mN/m. From that point, we slowly pull up the substrate at a rate of 1 mm/min while simultaneously keeping the surface pressure constant with a computer controlled feedback system between the electrobalance measuring of the surface pressure and the barrier moving mechanism. Consequently, the floating hexagonally close packed monolayer is adsorbed on the ITO surface. When the structure is totally removed from the water, the part that was initially immersed in the water is coated by a large area of nanoscale dielectric nanospheres on its entire surface.

Poly(vinyl alcohol) (avg. MW = 10,000 g/mol, 88% hydrolyzed, Sigma Aldrich) was spin cast from an aqueous solution containing 1 wt % PVA and 5 wt % gluteraldehyde onto the top glass surface of the cells with a thickness of 15-20 nm, as measured by ellipsometry. Poly(dimethylsiloxane) stamps were prepared from Sylgard 184 (1:10 curing agent : elastomer base, Dow Corning), poured into petri dishes to a thickness of ~ 5 mm, and baked for 85 minutes at 80 °C. A 2D colloidal crystal of 700 nm diameter, aminated silica spheres was deposited on a glass slide, as described above. Spheres were transferred to the PDMS by firmly pressing the stamp into the colloidal array and carefully peeling it away. The stamp, now "inked" with spheres, was pressed against the PVA-coated surface by hand. The cells were placed in a large glass jar, which was purged with argon, covered with a large crystallization dish, and baked for 2 hours at 100 °C. The atmosphere was again purged with argon after the first hour. The jar containing the cells was removed and allowed to cool to room temperature. The PDMS stamps were carefully peeled away to render high fidelity colloidal crystals adhered to the PVA-coated glass surface, with good transfer yield.

Optical Modeling

To support our proposed light-trapping mechanism via PC modes, we performed 1D transfer matrix simulations [6] to account for the graded index effects of the colloidal geometry. Because these 1D simulations cannot account for 3D modes, it provides a useful complement to our 3D FDTD simulations. For the transfer matrix simulations, the spheres were divided into 100 layers, each with an effective index

corresponding to the volume fraction of glass in air. Two simulations (Figure 8.1) demonstrate the calculated effects of these dielectric structures in the near- and far-field cases.

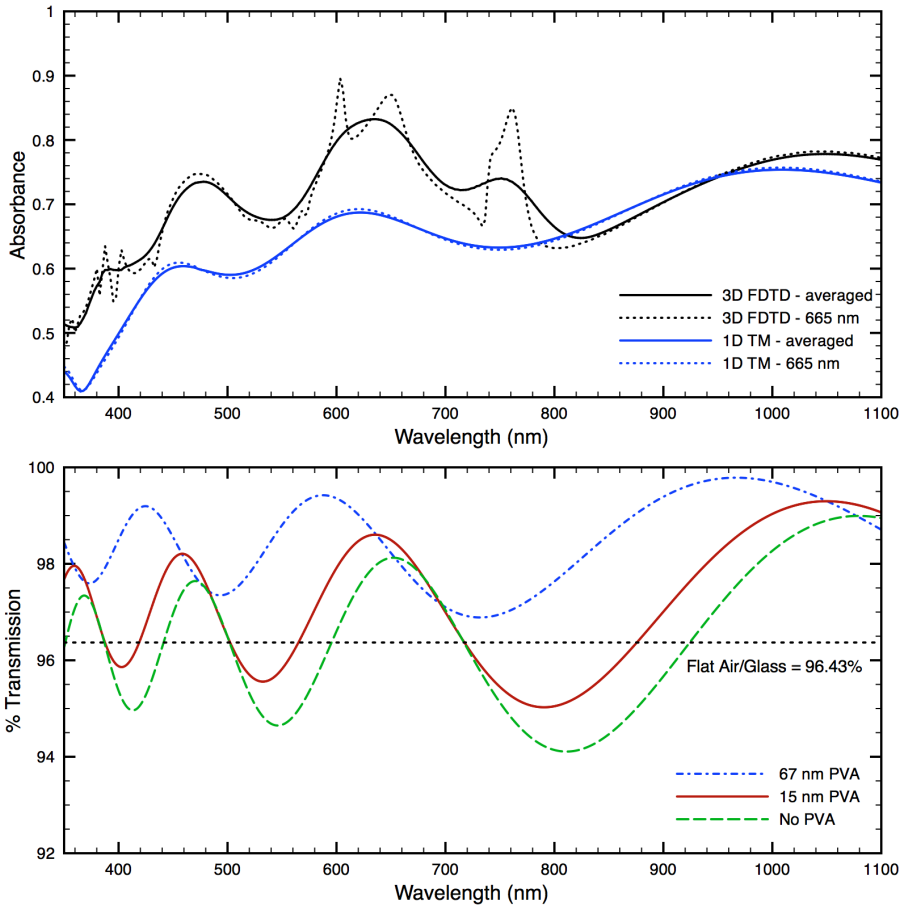

Figure 8.1: (a) 3D FDTD simulations are compared to 1D transfer matrix simulations for a graded index array approximating a silica sphere with 665 nm diameter. The main resonance is not observed in the transfer matrix simulations, as expected. (b) A graded index array approximating a 700 nm diameter sphere is simulated, with various thicknesses of PVA surrounding the base of the sphere.

Figure 8.1(a) shows the simulated absorption of an array of silica spheres on a c-Si wafer using each method, both averaged over 21 simulations as previously described, and for the mean sphere diameter. While the averaged simulations qualitatively share features, the absorption peak near 750 nm cannot be accounted for using the transfer matrix method. This peak corresponds to the strongest PC mode resonance, which has been aligned with the amorphous silicon absorption profile by design. This

provides further evidence that the observed absorption enhancement is due to the proposed PC mode coupling, and not simply a graded index effect due to the sphere geometry.

8.3 Detailed Procedures for Chapter 6

Isolation & Characterization of Complex ***6***

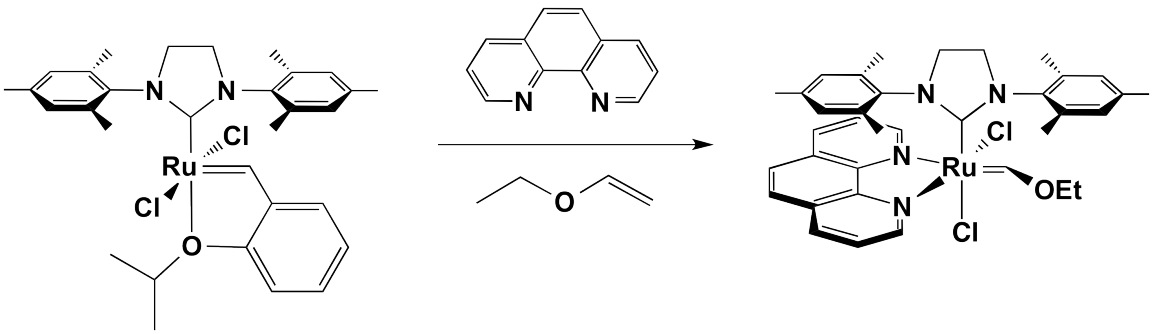

Figure 8.2: Complex **6** was isolated from the Grubbs-Hoveyda catalyst through the simple addition of phenanthroline and ethyl vinyl ether

In a nitrogen-filled glovebox, 100 mg of the Grubbs-Hoveyda catalyst and 30 mg 1,10-phenanthroline were suspended in 2 mL ethyl vinyl ether. The suspension instantly turned dark red, and was gently swirled for 3 minutes, before removing the volatiles *en vacuo*. The red solid was rinsed with 5 mL of pentane and dried *en vacuo*. Crystals were growth by dissolving this red solid in benzene, and slowly diffusing in hexanes. Mass was confirmed by high resolution mass spectroscopy (Measured 716.1628 , Calculated 716.1623)

Representative Conditions for Patterning the PLOMP 2.0 Resists

0. All silicon chips were cleaned with piranha before use, as described in Chapter 5.

1. Preheat wafer at 150 °C, then cool under a stream of argon.

2. Spin-coat $\sim$ 0.1 mL resist at 5000 RPM with a 5 second ramp time and 60 second dwell.

3. Prebake the wafer for 1 minute at $\sim$100 °C.

4. Cool wafer under a stream of argon, then expose to 250 nm blacklight for 2 minutes.

5. Postbake wafer for 4 minutes at 100 °C.

6. Cool under a stream of argon.

7. Develop by soaking in toluene for a bit, then swirling more and more aggressively

until the pattern has been visible developed (in 1 - 1.5 minutes, usually).

8. If necessary, rinse the wafer directly with toluene from a wash bottle to remove any remaining junk on the wafer.

Fabrication of Stamps for Substrate Conformal Nanoimprint Lithography

To prepare the master stamp, electron beam lithography and Inductively Couple Plasma Reactive Ion Etching (ICP-RIE) techniques were used. First, a silicon wafer was cleaned via sonication in acetone and then isopropanol, each for 5 minutes. Next a bufferd-HF acid etch was performed for between 15-30 second to remove any native oxide on the surface. The resist was spun onto the wafer within 20 minutes of this cleaning. For negative tone patterns, MA-N2803 was spun coat onto the wafer at 4,000 RPM with a minimal ramp time for 45 seconds. The wafer with resist was then baked on a hot plate at 90 °C for 60 seconds. For positive tone patterns, ZEP-520a was spun coat at 500 RPM for 5 second and then at 4,000 RPM for 45 seconds and then baked on a hot-plate at 180 °C for 2 minutes. The pattern was prepared with the Layout Editor CAD program and processed with the Genisys Layout BEAMER software. An important processing step was the addition of the Proximity Effect Correction in order to have a uniform pattern across the written pattern. A second crucial portion of the file processing was fracturing the pattern using the sequencing fracturing method with 10 nm resolution. This fracturing method bestowed both speed and pattern accuracy at resolutions and beam currents surprisingly high for the features being created. The pattern was exposed using the Leica Vistec EPBG 5000+ at a dose of around 415 μC/cm^2 (negative) or $\sim$280 μC/cm2 (positive) with a beam current of between 2nA and 10nA depending on the pattern, desired speed, and desired accuracy. Typically a 5nA beam current provided the best balance between accuracy and speed. The pattern was either developed in MF-319 for 45 seconds and immediately rinsed in Deionized water for 60s for MA-N2803, or developed in ZED-N50 for 60 seconds followed by a 20 seconds rinse in isopropanol for ZEP-520a and dried with nitrogen. After development, the wafer was etched using the Oxford Plasmalab 100 ICP-RIE system. A pseudo-bosch recipe was used with the parameters

of the etch recipe as follows: stage temperature of 20 °C, C_4F_8 flow of about 35 sccm and SF6 flow of about 26 sccm, RF forward power of 40 W and ICP forward power of 1200 W, a chamber pressure of 7.5 mTorr. The etch rate was about 120 nm/minute for silicon. The remaining resist was removed with an oxygen plasma etch recipe. Finally, the master stamps were surface treated with trimethylchlorosilane (TMCS) in the gaseous phase to prevent bonding of the XPDMS with the silicon master. This was performed by adding a few drops of (TMCS) to a closed chamber with the master stamp also inside. This was allowed to react for 30 min or more. The humidity in the chamber should be high for the best surface treatment. The master stamp was then used as a mold for the X-PDMS stamps, according to the procedure published by [7].

8.4 Detailed Procedures for Chapter 7

Preparation of a poly(DCPD-co-COD) Resist - PLOMP 2.1

A solution of 6 mL 1,5-cyclooctadiene and 6 mL dicyclopentadiene was degassed with bubbling argon for 15 minutes. Under argon, 2.0 mg catalyst **2** in 100 μL chloroform was added to the reaction, stirring at approximately 1500 RPM. After 33 minutes, the solution was still stirring, but viscous enough that the meniscus did not slosh when shaken, and was quenched with 10 mg 1,10-phenanthroline in 1 mL degassed ethyl vinyl ether. The solution was stirred for approximately 10 minutes and stored in the dark overnight before use. Overnight, the color of the solution changed from pink to dark, reddish orange.

Sample Preparation via Slow Evaporation

An inverted cap of an HPLC vial without a rubber septum was placed upside-down in the center of a 30 mm diameter coverslip, and held in place with a dab of vacuum grease. The cap was filled with photoresist, and placed under a cone of argon. Argon was flowed lightly over the sample for up to a few hours until the film had dried to a semi-solid.

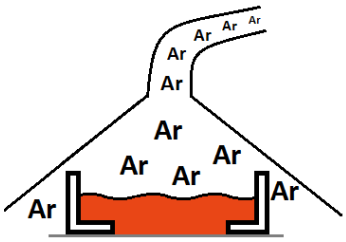

Figure 8.3: Slow evaporation under a stream of argon.

Chapter 9

MATLAB Code for Transfer Matrix Method Simulations

```
% Title:  1D Photonic Crystal Simulator
% Author: Raymond A. Weitekamp - May 2012 - raw@caltech.edu
%
% Description:  Transfer matrix based simulation which incorporates size
% distribution and partial decoherence, to mimic self-assembled lamellar
% structures or other imperfect multilayer stacks.
%
% Free parameters: sigma = coefficient of variation of layer thickness
%                  decoeff = coefficient of variation of decoherence
%
% Dependencies: multidiel_coherenceMod.m, guess_bragg_x0s.m
% must load polymer n,k as array with same array length as lambdas.
% i.e. - n_ps, k_ps, n_pla, k_pla
addpath /path/to/ewa; %load orfanidis

%--INPUT PARAMETERS
% index it's coming from
na=1;
% index it's going to
nb=1;

lambdaMax = 1000;
%number of periods
numLayers = 400;
%refractive indices
nPMMA = 1.50;
nPLA = 1.57;
%volume fractions
vf_pla = .5;
vf_pmma = .5;
%------------------

%--SETUP---

%setup layer arrays
lambda0 = 500; %center wavelength (arbitrary) (nm)
lambdaStart = 300;
lambdaEnd = 2000;
lambdas = [lambdaStart:1:lambdaEnd];%wavelength range (nm) (must match n_pla)

%guess the domain sizes
x0 = guess_bragg_x0s(nPMMA,nPLA,vf_pmma,vf_pla,lambdaMax);

%set polymer domain thicknesses 1 = PS , 2 = PLA
t1 = x0(:,1)
t2 = x0(:,2)

%angle averaging
angles = 0; %55; %latitude 35 degrees

%number of averages
numAvg = 200;

%coefficient of variation (of layer thickness)
sigma = 0.15;%.15;%.05;%.15;

%decoherence coefficient ( beta = decoeff * pi )
decoeff = 0;
%------------------

%--SOLVER LOOPS---
```

```
%setup avergaged reflectance array over all numbers of layers
R_layAvg = zeros(1,length(lambdas));
%step through numLayers
for num=1:length(numLayers)
    %setup avergaged reflectance array over all angles
    R_angAvg = zeros(1,length(lambdas));
    %step through angles
    for ii=1:length(angles)
        %setup avergaged reflectance array with variance
        R_avg = zeros(1,length(lambdas));
        %step through dispersity
        for i=1:numAvg
            %setup reflectance array for each wavelength
            R_now = zeros(1,length(lambdas));
            %step through wavelengths
            for j=1:length(lambdas)
                %nominal optical thickness of layers in terms of lambda0
                ot1 = nPMMA*t1/lambda0;
                ot2 = nPLA*t2/lambda0;

                %variation of layer thicknesses
                variation1 = (sigma*ot1).*randn(1,numLayers(num));
                variation2 = (sigma*ot2).*randn(1,numLayers(num));

                %layer thicknesses without dispersity (wavelengths in the material)
                L=repmat([ot1,ot2],1,numLayers(num));

                %add variance
                for x=1:length(L)
                    if(mod(x,2)>0)
                        L(x) = ot1 + variation1(x/2 + .5);
                    else
                        L(x) = ot2 + variation2(x/2);
                    end
                end

                %indices corresponding to layers
                n=[na,repmat([nPMMA,nPLA],1,numLayers(num)),nb];

                %write to reflectance array
                R_now(:,j)=abs(multidiel_coherenceMod(n,L,(lambdas(j)./lambda0),angles(ii),'te',decoeff)).^2;
            end
            R_avg = R_avg + (R_now./numAvg);
            i
        end
        R_angAvg = R_angAvg + (R_avg./length(angles));
    end
    R_layAvg = R_layAvg + (R_angAvg./length(numLayers));
end

%------------------

%--PLOT---
figure; plot(lambdas,R_layAvg,'-b');
%------------------
```

```
%--FUNCTIONS-------
% Title: multidiel_coherenceMod.m
% Description: modified version of Orfanidis' multidiel1() to account for partial decoherence
% Author: Raymond A. Weitekamp - 2012 - raw@caltech.edu
% Comments: modification based on Troparevsky et al, Optics Express, Vol. 18, Issue 24, pp. 24715-24721 (2010)
%           http://dx.doi.org/10.1364/OE.18.024715
%-----------------------------------------------
%
%          na | n1 | n2 | ... | nM | nb
% left medium | L1 | L2 | ... | LM | right medium
%   interface 1    2    3     M   M+1
%
% Usage: [Gamma1,Z1] = multidiel1(n,L,lambda,theta,pol,deco)
% n      = vector of refractive indices [na,n1,n2,...,nM,nb]
% L      = vector of optical lengths of layers [n1*l1,...,nM*lM], in units of lambda_0
% lambda = vector of free-space wavelengths at which to evaluate input impedance
% theta  = incidence angle from left medium (in degrees)
% pol    = 'tm' or 'te', for parallel/perpendicular polarizations
% deco   = coefficient of variation for decoherence, deco*pi = beta = standard
%          deviation of the randn distribution
%
% Gamma1 = reflection response at interface-1 into left medium evaluated at lambda
% Z1     = transverse wave impedance at interface-1 in units of eta_a (left medium)
%
% notes: simplified version of MULTIDIEL for isotropic layers
%
%        M is the number of layers (must be >=0)
%
%        optical lengths are L1 = n1*l1, etc., in units of a reference
%        free-space wavelength lambda_0. If M=0, use L=[].
%
%        lambda is in units of lambda_0, that is, lambda/lambda_0 = f_0/f
%
%        reflectance = |Gamma1|^2, input impedance = Z1 = (1+Gamma1)./(1-Gamma1)
%
%        delta(i) = 2*pi*[n(i)*l(i)*cos(th(i))]/lambda
%
%        it uses SQRTE, which is a modified version of SQRT approriate for evanescent waves
%
%        see also MULTIDIEL, MULTIDIEL2

% Sophocles J. Orfanidis - 1999-2008 - www.ece.rutgers.edu/~orfanidi/ewa

function [Gamma1,Z1] = multidiel_coherenceMod(n,L,lambda,theta,pol,deco)


M = length(n)-2;                                % number of slabs

if M==0, L = []; end                            % single interface, no slabs

theta = theta * pi/180;

% costh = conj(sqrt(conj(1 - (n(1) * sin(theta) ./ n).^2)));    % old version

costh = sqrte(1 - (n(1) * sin(theta) ./ n).^2);                 % new version - 9/14/07

if pol=='te' | pol=='TE',
    nT = n .* costh;                            % transverse refractive indices
else
    nT = n ./ costh;                            % TM case, fails at 90 deg for left medium
end
```

```
if M>0,
    L = L .* cosh(2:M+1);                       % n(i)*l(i)*cos(th(i))
end

r = -diff(nT) ./ (diff(nT) + 2*nT(1:M+1));      % r(i) = (n(i-1)-n(i)) / (n(i-1)+n(i))

beta = deco*pi;                                 % beta = decoherence factor * pi

Gamma1 = r(M+1) * ones(1,length(lambda));       % initialize Gamma at right-most interface

for i = M:-1:1,
    delta = (2*pi*L(i)./lambda)+(beta.*randn);  % phase thickness in i-th layer, perturbed by distribution with STD = beta
    z = exp(-2*j*delta);
    Gamma1 = (r(i) + Gamma1.*z) ./ (1 + r(i)*Gamma1.*z);
end

Z1 = (1 + Gamma1) ./ (1 - Gamma1);



%guess bragg x0s
function [x0_guess] = guess_bragg_x0s(nA, nB, vfA, vfB, lambdaMax)
xA_guess = lambdaMax/(2*(real(nA)+(real(nB)*vfB/vfA)));
xB_guess = vfB/vfA*xA_guess;
x0_guess = [xA_guess,xB_guess];
end

%------------------
```